National Technical University of Athens

School of Naval Architecture & Marine Engineering

Division of Marine Engineering

COMPUTATIONAL STUDY OF METHANOL COMBUSTION CHEMISTRY FOR SUPERCITICAL CARBON DIOXIDE CONSITIONS

Diploma Thesis

by

Theodora Syrrou

Examination Committee:

Supervisor: L. Kaiktsis, Professor (NTUA)

Members: G. Papalambrou, Associate Professor (NTUA)

G. Papadakis, Assistant Professor (NTUA)

Athens, June 2024

Acknowledgements

This thesis signifies the end of my undergraduate studies at the School of Naval Architecture and Marine Engineering of the National Technical University of Athens, which have been a significant milestone in my life and career. At this point, I would like to express my gratitude to the people who supported me during the past five years.

First, I would like to express my heartfelt gratitude to my supervisors, Lambros Kaiktsis, Professor at the National Technical University of Athens, and D. Kazangas, PhD Student at the National Technical University of Athens, for the excellent collaboration, great assistance and guidance over the difficulties that occurred in the course of my Diploma Thesis.

Finally, I would like to thank my family, my friends, and my colleagues for their unwavering support and encouragement throughout my five-year educational journey. The trust and confidence that they have placed in me have served as a constant source of inspiration throughout my studies.

Abstract

The present diploma thesis investigates methanol (CH_3OH) ignition and combustion under CO_2 supercritical conditions (sCO_2). The topic is currently of interest for gas turbine applications in the context of greenhouse gas (GHG) emissions reduction and is of interest for marine applications. The present study is computational and assesses a reduced-order chemical kinetic mechanism for methanol combustion applications across a wide range of pressure, temperature, and fuel-air equivalence ratios, typical of dual-fuel marine engines and gas turbines. Detailed combustion mechanisms include hundreds or even thousands of reactions and species, making them computationally expensive for simulations. Reduced-order combustion mechanisms, including skeletal and simplified combustion mechanisms, provide simplified representations of the detailed combustion mechanisms. Their main advantage over detailed mechanisms is their computational efficiency, enabling faster simulations, suitable for large-scale Computational Fluid Dynamics (CFD) simulations. Thus, reduced-order mechanisms provide a computationally efficient tool for simulating complex combustion phenomena, while maintaining the key features of combustion chemistry.

Chemical kinetic mechanisms are commonly validated against experimental data, to ensure they can reproduce essential combustion characteristics. In the present study, the reduced-order mechanism *ACR55* of Pichler & Nilsson (2018) was evaluated through comparison with experimental data, as well as against the computational results of the detailed mechanism *Updated HP-Mech* of Wang et al. (2022). The reduced-order mechanism consists of 18 species and 55 irreversible elementary reactions, while the detailed mechanism includes 131 species and 899 reversible elementary reactions. The following problems have been considered: (a) premixed laminar flame, (b) ignition of homogeneous mixtures, and (c) combustion at Perfectly Stirred Reactor (PSR) conditions. In all cases, standard mixtures considered in the experiments (methanol in air/O_2 and O_2/Ar as diluent) were used – no experimental data for methanol ignition and combustion with supercritical CO_2 as diluent are yet reported in the open literature. The CHEMKIN code was used as the simulation tool.

The computational results obtained from the two mechanisms were evaluated by comparison with experimental data in the context of the above three standard problems. The computational results have proven a very good performance of the reduced *ACR55* mechanism, which is demonstrated by the good comparison against the experimental data and the detailed mechanism *Updated HP-Mech*, for all three problems investigated.

To study the effect of CO_2 as diluent (supercritical conditions), calculations were performed for the three reference problems, for: (a) N_2 as diluent, and (b) s-CO_2 as diluent, at the same conditions, which include representative gas turbine and marine dual-fuel engine conditions. In particular, the following range was considered: pressures of 175 – 250 atm, initial temperatures (mainly) of 1300 – 1800 K, equivalence ratios of 0.5 – 2.0. The main findings of the present computations can be summarized as follows.

i. Ignition of homogeneous mixtures: The two mechanisms bear similar results, in the entire range of conditions considered. For equivalence ratios in the range φ=0.8-1.5, and for all pressures, in the high temperature range (T=1500-1800 K), ignition delay times are higher in the case of using N_2 as diluent. The discrepancies between the two diluent cases diminish at high values of φ.
ii. Combustion at PSR conditions: The two mechanisms produce comparable results in the entire range of conditions investigated. For lean and stoichiometric mixtures, the produced CO_2 is higher for N_2 as diluent. For rich mixtures, a decrease of CO_2, with

reference to the initial concentration of 85% CO_2, is observed for the case of sCO_2 as diluent.

iii. Premixed laminar flames: For unburned mixture temperatures of 600 K and 700 K, the laminar flame speed is significantly higher for N_2 dilution, for all stoichiometries considered. For unburned mixture temperatures of 600 K and 700 K, the laminar flame speed is significantly higher for N_2 dilution, for all stoichiometries considered. For unburned mixture temperature of 1800 K and lean mixtures, the laminar flame speed remains higher for N_2 dilution, however the differences are less pronounced; for rich mixtures, the laminar flame speed is substantially higher for N_2 dilution.

For the three problems studied, representative cases were characterized by performing Rate Of Production (ROP) analysis, for identifying the principal chemical pathways. ROP analysis thus enables an understanding of the differences between N_2- and s-CO_2 dilution, as identified in the simulations performed. Here, the following cases were analyzed: (i) Ignition of homogeneous mixture: $\varphi=0.5$, $T=1500$ K, $p=220$ bar. (ii) Combustion at PSR conditions: $T=1500$ K, $p=220$ bar, $\varphi=0.8$ and $\varphi=2.0$. (iii) Premixed laminar flame: unburned mixtures with $T=700$ K and $T=1800$ K, $\varphi=0.5$, $p=200$ atm and $p=220$ atm. The results of ROP analysis identify the chemical paths of important species and explain the observed differences regarding the effects of N_2- and s-CO_2 dilution.

CONTENTS

List of Abbreviations

BC:	Black carbon
BSFC:	Brake specific fuel consumption
CCR:	Carbon capture and recovery
CCS:	Carbon capture and storage
CH_2O:	Formaldehyde
CH_4:	Methane
CO_2:	Carbon dioxide
E_a:	Activation energy
ECAs:	Emission control areas
EGR:	Exhaust Gas Recirculation
GC:	Gas chromatographs
HC:	Hydrocarbons
ICEs:	Internal combustion engines
IMO:	International Maritime Organization
JSR:	Jet Stirred Reactor
NECAs:	Nitrogen oxide emission control areas
NO_x:	Nitrogen oxides
NTC:	Negative temperature coefficient
OC:	Octane number
PM:	Particulates matter
PSR:	Perfectly stirred reactor
ROP:	Rate-of-production
sCO_2:	Supercritical CO_2
SCR:	Selective catalytic reduction
SECAs:	Sulphur Emission Control Areas
SI:	Spark-ignition
ST:	Shock tube
SO_x:	Sulfur oxides
VOCs:	Volatile organic compounds

GHG:	Greenhouse Gas

CHAPTER 1: Introduction

1.1 Ship Emissions

Maritime transport is the core of global commerce, accounting for 80% of goods transported by volume. However, the shipping industry is a major source of air pollution, accounting for 3% of anthropogenic global greenhouse gases (IMO, 2020). The primary sources of concern are greenhouse gases, which cause global warming, as well as toxic, noxious, and sulfuric gases, which threaten human health and the environment.

The International Maritime Organization (IMO) is a specialized division of the United Nations (UN) that publishes global regulations regarding the safety, security, and environmental performance of international shipping. International regulations, such as those established by the IMO, seek to tackle and reduce these emissions by implementing measures such as fuel sulfur content limits, engine efficiency requirements, and the introduction of alternative fuels and technologies. The IMO established a comprehensive roadmap with the Initial GHG Strategy, which was published in 2018, and revised it with the 2023 GHG Strategy.

The Initial GHG Strategy targeted a 40% reduction in CO_2 emissions by 2030 and 70% by 2050, compared to the levels recorded in 2008, as well as a decrease of total annual GHG emissions by at least 50% or more by 2050 relative to 2008 levels from the international shipping industry. On the other hand, the 2023 GHG Strategy established a net zero GHG target by or around 2050, with intermediate targets of 30% in GHG and 40% CO_2 reduction per transport work by 2030, relative to 2008. The IMO 2023 Greenhouse Gas Strategy (GHG) was approved at the 80th Marine Environment Protection Committee (MEPC) meeting on July 7, 2023, leading to a new era in climate change mitigation efforts.

Generally, the decarbonization process involves two main approaches: improving energy efficiency and using alternative fuels. This thesis investigates methanol as a potential alternative fuel for marine engines, exploring its capacity to reduce global maritime emissions.

1.1.1 Types of emissions

Vessels generate a wide range of emissions, which can be broadly categorized as air pollutants and greenhouse gases. The most common emissions from vessels are sulfur oxides (SO_x), nitrogen oxides (NO_x), particulates matter (PM), carbon dioxide (CO_2), volatile organic compounds (VOCs), and methane (CH_4). Various factors may affect the generation of each emission.

Sulfur Oxides (SO_x)

Sulfur oxides are produced when vessels burn fuels containing sulfur. The International Maritime Organization (IMO) has implemented regulations to limit the sulfur content in marine fuels to reduce SO_x emissions, particularly in designated emission control areas (ECAs). Switching to alternative fuels with low or zero sulfur content, such as liquefied natural gas, methanol, propane, biodiesel and hydrogen can help reduce or eliminate SO_x emissions. Additionally, technical measures for SO_x reduction include the installation of exhaust gas cleaning systems, known as scrubbers, and catalytic recirculation systems.

Nitrogen Oxides (NO_x)

NO_x emissions are primarily produced by the reaction of atmospheric nitrogen with oxygen via the Zeldovich mechanism, which is significantly influenced by combustion temperature (Mwangi et al.,2015). NO_x emissions are affected by a wide range of engine parameters, including combustion temperature, residence time of the combustion process, oxygen availability, and ignition delay (Patel et al. 2014). Recirculation (EGR) arrangements and selective catalytic reduction (SCR) systems appear to be promising NO_x reduction technologies. EGR reduces the quantity of oxygen in the engine combustion chamber by recirculating a portion of the exhaust gas to the scavenging air intake, resulting in a decrease in peak combustion temperature. Nevertheless, as a consequence of oxygen shortage during the engine combustion process, this system might raise engine emissions such as black carbon (BC) (Nielsen et al., 2018). On the other hand, SCR system decreases NO_x in engine exhaust by transforming NO_x into N_2 and water via a metal catalyst and ammonia as a reduction component. Exhaust temperatures must be held as high as possible to maintain the necessary NO_x decrease. Additionally, appropriate engine setting, layout, and maintenance may enhance combustion and decrease NO_x emissions. Lastly, several alternative fuels lead to lower NO_x emissions compared to conventional marine fuels.

Particulate Matter (PM)

Particulate matter consists of tiny particles released into the air during fuel combustion. PM emissions can have an adverse effect on health, so efforts are underway to regulate and decrease them via engine design and fuel quality regulations. Particulate matter formation is affected by fuel quality, particularly its sulfur content. Using cleaner fuels with lower sulfur concentrations and installing particulate filters in exhaust systems may contribute to the reduction of PM emissions.

Carbon Dioxide (CO_2)

Vessels generate CO_2 as a byproduct of burning fossil fuels. The attempts to decrease CO_2 emissions that derive from the shipping industry involve enhancing fuel efficiency, investigating alternative fuels, and introducing more environmentally friendly technologies. Energy-efficient technologies, optimized ship design, advanced propulsion systems, and more efficient engines can all help to improve fuel efficiency and reduce CO_2 emissions per unit of cargo transported. Transitioning to alternative fuels such as LNG, hydrogen, or biofuels may assist with minimizing shipping's carbon footprint.

Volatile Organic Compounds (VOCs)

Volatile Organic Compounds are released during the handling and transportation of certain kinds of cargo. These cargos include mostly chemicals and petrochemicals. They contribute to air pollution and have environmental and health consequences. Vapor recovery systems can capture and recover VOC emissions during cargo handling. Additionally, implementing enclosed systems during cargo transfer can control and reduce VOC emissions.

Methane (CH_4)

Methane is another greenhouse gas emitted by vessels. While its contribution is generally lower compared to CO_2, it is more potent in terms of its warming potential. Methane emissions are related to the type of fuel used. Choosing fuels with lower methane content, such as liquefied natural gas LNG, results in lower methane emissions compared to traditional marine fuels. Lastly, methane emissions can also occur through leaks in the fuel system. Regular maintenance and leak detection measures can minimize these emissions.

1.1.2 Regulations for CO_2 emissions – EEDI-EEXI-CII

EEDI, which has been in effect since January 1, 2013, requires the evaluation and regulation of energy efficiency during the ship design stage. The Energy Efficiency Design Index (EEDI) was established initially as a metric for estimating the energy efficiency of newly built ships. The IMO established EEDI as an equitable basis for benchmarking and to foster energy efficiency innovations on maritime vessels. It established the baseline efficiency level for new ships based on their size and type. The average efficiency data of newly built vessels between 1999 and 2009 was used to calculate reference lines for each ship type. A reference line is a curve representing the average index value calculated from a collection of individual index values (IMO, 2013). The lower the EEDI, the more efficient and cost-effective the ship's design. Ships that meet energy efficiency standards can enter into more lucrative chartering agreements. EEDI has been a required application since 2013, and it has been tightened over three phases. Initially, Phase zero was defined, which included ships built between 2013 and 2015. It required a design efficiency that was at least equal to the reference line. Phase one, which implies an EEDI that is at least 10% lower than the reference point, addressed ships built between 2015 and 2020 and went into effect in January 2015. Phase two aims to achieve an EEDI at least 20% lower than the reference point for vessels built between 2021 and 2025. It has been required since January 2020. Phase three is set to start in January 2025 and will include ships built after 2025. This phase requires an EEDI that is at least 30% lower than the reference point (Lu et al., 2021, as cited in Bayraktar & Yuksel, 2023). EEDI applies to all globally operating ships of 400 gross tonnages or more involved in international voyages that require International Energy Efficiency (IEE) certificates. Particularly, EEDI regulations apply to:

1.Ships with a construction contract issued on or after January 1, 2013.

2.Ships without a building contract but with the keel laid or in a similar stage of construction on or after July 1, 2013.

3.Ships delivered on or after July 1, 2015.

The "Attained EEDI" indicates each ship's calculated value, as opposed to the "Required EEDI," which is a regulatory standard that varies depending on ship type and size. It is crucial that the Attained EEDI is equal to or lower than the Required EEDI. The Attained EEDI is calculated using several factors, including a reduction factor (y) defined in MARPOL Annex VI. This process also takes into account a reference line based on ship-specific parameters. The CO_2 conversion factor (Cf), certified fuel consumption (SFC), and rated installed power of main engines (PME) are all factored into the Attained EEDI calculation formula. These parameters are adjusted for specific conditions such as water temperature, load draught, and weather (Class NK, 2023; IMO, 2014, 2018b, 2022a, as cited in Bayraktar & Yuksel, 2023).

The formula for computing the Attained EEDI is as follows:

Attained EEDI ≤ Required EEDI =$(1 - \frac{y}{100})$ x EEDI Reference line (1)

In this equation, 'y' represents the reduction factor from Table 1 of MARPOL Annex VI Chapter 4 Reg.24. Equation (2) defines the Reference Line as follows:

Reference line = $a \times b - c$ (2)

In this formula, 'a', 'b', and 'c' are key parameters used in the EEDI estimation, as described in Table 2 of MARPOL Annex VI Chapter 4 Reg. 24. This table contains the calculation formulas for the Reference Line for each ship type.

EEXI, which went into effect on January 1, 2023, assesses the energy efficiency of currently operational ships. EEXI represents the CO_2 emissions (in grams) from a marine vessel per ton of transported cargo for one nautical mile. It is a revised version of EEDI, and the underlying concept is similar. EEXI measures a ship's energy efficiency success in comparison to a baseline, and its primary goal is to reduce CO_2 emissions per unit of transportation sourced by existing vessels. It represents the technical approach to accomplishing emission decrease goals, with the required EEXI being similar to the required EEDI for newly built vessels in 2023. To guarantee that a ship meets a minimum energy efficiency standard, the computed EEXI value for every vessel must be lower than the required EEXI. The IMO adopted the EEXI as an amendment to MARPOL Annex VI in June 2021 with the goal of reducing CO_2 emissions from existing ships. This regulation applies to all ships with a gross tonnage of 400 or more that are involved in international voyages. To ensure legal compliance, these vessels must maintain an EEXI technical file for calculating the Attained EEXI and have an updated International Energy Efficiency Certificate (IEEC). The EEXI calculation is required for all ships on international voyages, with the exception of those already in compliance with EEDI regulations. The EEXI calculation is similar to that of the EEDI, with the "Attained EEXI" being equal to or less than the "Required EEXI." The calculation for EEXI employs a specific reduction factor (y) and a reference line equation similar to that utilized for EEDI calculations. In short, it determines the amount of CO_2 emissions produced by a vessel transporting 1 ton of cargo across a distance of 1 nautical mile, i.e., $g \cdot CO_2/ton \cdot mile$, which is similar to the approach adopted in EEDI (Lee, 2024).

The carbon intensity indicator (CII) calculation and reporting became mandatory on January 1, 2023 (IMO, 2022). The CII is used to calculate carbon emissions and rating boundaries for ships. It is an index that assesses GHG emissions in terms of freight volume and miles traveled. The CII determines the annual reduction factor needed to keep a ship's operational carbon intensity within a specified rating level. The required annual operational CII needs to be compared to the actual annual operational CII (Bayraktar & Yuksel, 2023) . This allows for the calculation of the operational carbon intensity rating. The ship's efficiency category (A, B, C, D, or E) is determined by its CII. The "Statement of Compliance," outlining the performance level, will be encompassed in the ship's Ship Energy Efficiency Management Plan (SEEMP). A ship must provide an improvement strategy describing how it will achieve the required index of C or higher if it has been rated D for three years in a row or E for one year. Ships of 5000 gt or more, as well as EEDI-applied vessels, must submit an annual CII application and ratings (IMO, 2022; Ivanova, 2021, as cited in Bayraktar & Yuksel, 2023).

1.1.3 Regulations for SO_x emissions

SECAs are geographic areas where strict regulations are established to regulate and lower sulfur oxide (SO_x) emissions from ships, as stated in Annex VI of the 1997 MARPOL Protocol. Ships operating in SECAs have to utilize fuels with lower sulfur content compared to global standards. Ships equipped with exhaust gas cleaning systems, also known as scrubbers, can use high-sulfur fuels while reducing sulfur emissions onboard. SECAs are divided into two categories: those that are created by the International Maritime Organization (IMO) and those published by governments. The IMO established four SECAs on January 1, 2015: the Baltic Sea, North Sea, North America, and Caribbean Sea (IMO, 2022). Other countries, such as China and Korea, have established SECAs in their coastal areas. In 2015, the Chinese Ministry of Transportation established SECAs with a sulfur limit of 0.5% across three water regions: the Pearl River Delta, the Yangtze River Delta, and Bohai (Beijing, Tianjin, and Hebei) (MOT, 2015, as cited in Shao et al., 2023). Furthermore, the government examined the possibility of reducing fuel sulfur content to 0.1% by 2025 (MOT, 2018). The Korean Ministry of Maritime Affairs and Fisheries also implemented SECAs in 2020 (Korea, 2021).

Regulation 14 determines sulfur emission factors and imposes limits on sulfur content in fuel (IMO, 2020 Sulphur Cap), both globally and in Sulfur Emission Control Areas (SECAs). Since January 2020, the global limit for sulfur in fuel oil has been reduced from 3.5% to 0.5% by mass. However, in SECAs which have stricter requirements for SO_x emissions and sulfur in fuel content, the limit has been adjusted to 0.1% by mass (McCaffery et al., 2021; Chen et al., 2018, as cited in Topic et al., 2023). The "IMO 2020 sulfur cap" standard, a requirement for an 85% reduction in sulfur oxides, aims to reduce emissions and improve public health. The primary source of sulfur oxide emissions from oceangoing ships is fuel combustion in the ship's main engines, which generate exhaust gases (Gusti and Semin, 2016, as cited in Elmi et al.,2023). Sulfur emissions from ships do not directly affect the environment, but they have adverse impacts on air quality and human health (Tzannatos, 2010; Tichavska and Tovar, 2015; Spengler and Tovar, 2021, 2022, as cited in Shao et al., 2023). Furthermore, shipping-related sulfur emissions represent 13% of total anthropogenic pollutant emissions (Zhen et al., 2022, as cited in Shao et al., 2023). With no action, emissions could rise to 130% of their 2008 levels by 2050.

1.1.4 Regulations for NO_x emissions - IMO TIERS

ECAs with nitrogen oxide restrictions are referred to as nitrogen oxide emission control areas (NECA). The International Maritime Organization (IMO) uses the designation "NECAs" to identify areas where strict regulations are established to regulate and decrease nitrogen oxide (NO_x) emissions from vessels. The International Maritime Organization (IMO) implemented the Regulations for the Prevention of Air Pollution from Ships and applied Tier III standards to NO_x emission control areas after 2016. Policy measures for nitrogen oxides (NO_x) reduction are defined by the IMO Tier III standard, Regulation 13, which requires all marine engines built after 2016 with installed main engine power greater than 130 kW to reduce NO_x emissions by 80% compared to Tier I (IMO, 2020). However, the strictest decrease measure, Tier III, is mandatory only for ships operating in NO_x Emission Control Areas (NECA) or ports with individually established Tier III regulations.

The International Maritime Organization established a set of standards referred to as the "Marine Engine Tier Standards" to regulate and minimize emissions from ship engines. The IMO Tier Standards are part of Annex VI of the International Convention for the Prevention of Pollution from Ships (MARPOL). These standards limit the emissions of nitrogen oxides (NO_x) from marine diesel engines. The regulations aim to improve air quality by limiting the amount of NO_x emitted into the atmosphere.

The different levers or tiers depend on the ship's construction date and engine speed, as shown in Figure 1 (Van et al.,2019). Tier III requirements are only applicable to new vessels that sail within Nitrogen Oxide Emission Control Areas (NECAs). The main tiers are as follows:

IMO Tier I applies to engines installed on ships build on or after January 1, 2000. This tier established the initial NO_x emissions limits.

IMO Tier II applies to engines installed on ships build on or after January 1, 2011, in designated NOx Emission Control Areas (NECAs). It introduced stricter NO_x limits compared to Tier I.

IMO Tier III applies to engines installed on ships built on or after January 1, 2016, which operate in NECAs. Tier III encounters the strictest NO_x limits, requiring a major decrease in NO_x emissions in comparison with Tiers I and II. It aims to tackle localized air quality issues in specific emission control zones. Since 2016, the NO_x limit for low-speed marine engines (n < 130 r/min) in the Emission Control Area (ECA) is 3.4 g/kWh, which is approximately 80% lower than Tier I standards (Zhang et al., 2023).

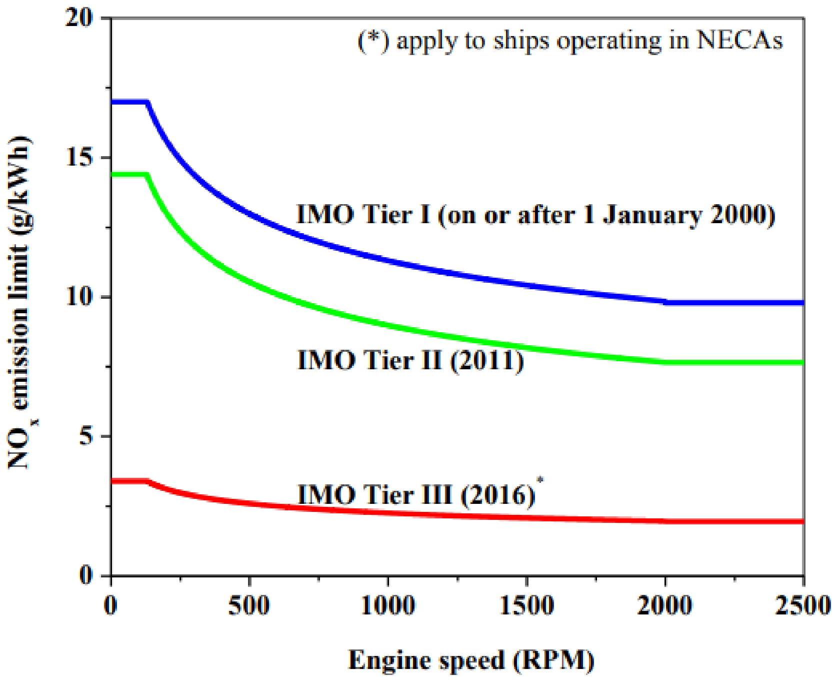

Figure 1. IMO Tiers for reduction of NOx emissions

1.1.5 Regulations for Methane slip

Methane slip refers to the escape of unburned methane from an engine's combustion chamber and other areas of the ship where it is stored and transferred. Methane slip is the leading environmental problem associated with the operation of gas-fueled MDEs, and it needs to be addressed due to its significant impact on global warming. Methane has an 86-fold higher 20-year global warming potential (GWP) than carbon dioxide, while on a 100-year time scale, it is still considered relatively high but reduced to 25 (Ushakov, Stenersen, & Einang, 2019). If methane slip is not properly controlled, the environmental advantages of LNG use are significantly reduced or even eliminated (when compared to diesel or HFO fuels) due to methane's high greenhouse impact. In addition, LNG has a higher leakage rate in the supply chain than fossil fuels. LNG escapes at all stages, including storage, transportation, and usage. It is estimated that leakage from the combustion chamber exceeds that from the supply chain. The rate of leakage is affected by several factors, including engine type, load, fuel, duty cycle, and speed. The factors listed above can cause increased methane slip via the engine exhaust system or crankcase ventilation.

It is worth noting that all ships of 5,000 gross tonnage or more that enter EU ports are subject to the EU Emission Trading System (ETS) since January 2024. This implies that ship owners are required to pay for the GHG emissions when transporting to, from, or between EU ports. The EU ETS is based on TtW emissions and will originally only include CO_2 emissions. However, beginning in 2026, methane emissions will be included as well. Consequently, eliminating or reducing methane emissions to a safe level is a critical milestone before approving LNG engines for all types of vessels. Multiple approaches have been suggested for minimizing methane slip.

Firstly, operation at a high air excess ratio causes increased methane slip (particularly at low loads) because of incomplete combustion in the form of quenching at the coldest part of the combustion chamber. To address this, it is feasible to enrich the mixture in the main chamber, which will most probably minimize unburned methane emissions while ensuring a stable ignition and combustion process even at low loads. Moreover, the crevice volume represents the sum of all the small volumes in the combustion chamber where the flame cannot propagate and unburnt methane remains. The reduction of "dead space" in the form of crevices between cylinder unit components within the combustion chamber may result in methane emission decreases down to 3.0-4.0 g/kWh. Overall, the utilization of an advanced fuel-air ratio control system for enrichment at low loads, combined with an appropriate combustion chamber design focused on reducing the volume of crevices, can significantly reduce methane emissions to 2.5-3.0 g/kWh. Furthermore, LNG engines run on a mix of air and LNG provided via the air inlet valve. The required ignition for the LNG fuel is provided by a small quantity of diesel fuel that serves as pilot fuel. Engine manufacturers are now looking into the adoption of direct gas injection, which allows LNG to be introduced directly into the combustion chamber rather than mixed with air first. The LNG enters the combustion chamber directly late in the compression stroke via a separate injector. One more diesel injector provides a small amount of fuel for ignition. High-pressure (1500+ bar) LNG injection results in a higher flow rate per unit area. It additionally allows for a favorable heat release rate curve, which improves fuel efficiency even more. Improving direct gas injection technology leads to a reduction in methane slip of up to 90%. This process allows a very small amount of methane to escape, between 0.2 and 0.3 g/kWh. Lastly, aftertreatment solutions, particularly oxidation catalysts, are especially appealing because they enable a 70% reduction in methane slip. Oxidation catalysts have already been employed in a wide range of industrial procedures to eliminate hydrocarbons from exhaust. Engine manufacturers are currently looking into after-treatment solutions as a more viable method of controlling methane slip than direct gas injection.

1.1.6 Regulations for Nitrous Oxide

According to the Intergovernmental Panel on Climate Change's fifth assessment report (2014), N_2O has a 265 times greater global warming potential (GWP) than CO_2 over a 100-year time horizon. Despite the fact that N_2O's GWP has been reduced from 310 to 265 over the last two decades, it is still approximately ten times that of methane (CH_4) (Jung et al.,2022). In terms of anthropogenic radiative forcing, N_2O is the third most important well-mixed GHG after CO_2 and CH_4. N_2O also contributes significantly to stratospheric ozone depletion (Ravishankara et al., 2009, as cited in Jung et al.,2022). Every year, the concentration of N_2O in the atmosphere increases by around 0.2 to 0.3%. Nitrous oxide (N_2O) is the third most potent long-lived greenhouse gas in the atmosphere, with a radiative forcing of 0.17 W/m^2. N_2O is generated as a byproduct of NO_x reduction reactions in exhaust gas after-treatment systems, such as selective catalytic reduction (SCR) systems based on aqueous urea solution. Following the implementation of catalytic controls to meet more stringent NO_x regulations, N_2O emissions from diesel engines have become a greater source of concern. The primary concern in diesel

NO_x abatement systems today is to avoid a trade-off relationship in which NOx is reduced but N2O increases, while maintaining excellent NOx conversion efficiencies.

Companies must monitor and report CO_2 emissions, as well as methane (CH4) and nitrous oxide (N2O) emissions, beginning January 1, 2024.

1.1.7 Regulations for Particulate Matter (PM)

The shipping industry generates 1 million tons of particulate matter (PM) per year. The use of fuel with a high fuel sulfur content (FSC) is a major contributor to ship-generated PM emissions. Extensive research has been conducted to determine the impact of FSC on PM emissions. Adding 1 ppm FSC increases PM concentration by 36 × 106 parts per cubic centimeter on average (Zhao et al.,2022). High FSC has been shown to promote soot formation due to the oxygen sink from sulfur, resulting in higher PM emissions. Combustion-generated PM emissions include soot or black carbon (BC), which is the second leading climate forcing agent after CO_2 (Bond et al., 2013, as cited in Trivanovic et al.,2019). Compared to GHGs, the impact of BC on the environment is far more complex and regional. The Arctic is especially vulnerable to BC emissions because particles deposit on the surface of snow and ice, transforming surface albedo and boosting melting rates (Law & Stohl, 2007, as cited in Trivanovic et al.,2019). Furthermore, the negative health effects of BC are a source of concern in port cities (Corbett et al., 2007), as it is linked to cardiovascular disease (Luben et al., 2017, as cited in Trivanovic et al.,2019), lung diseases with premature death, impaired cognition (Power et al., 2011, as cited in Trivanovic et al.,2019), increased morbidity, and smog formation.

There is currently no regulation in place for marine vessel PM emissions. Countermeasures against ship emissions, such as installing sulfur scrubbers, using low-sulfur fuel or alternative fuels, and implementing catalyzed filter processes, have significantly reduced PM emissions in some parts of the world. A variety of filter types have been developed and tested over the years to remove diesel particulate matter (PM), but the ceramic wall flow filter is currently the preferred PM trapping technology (Johansen, 2015). Cordierite, silicon carbide, aluminum titanate, and mullite are among the most popular ceramic filter materials. Figure 2 depicts the principle of PM trapping and the main reactions of a catalyst-coated wall flow filter.

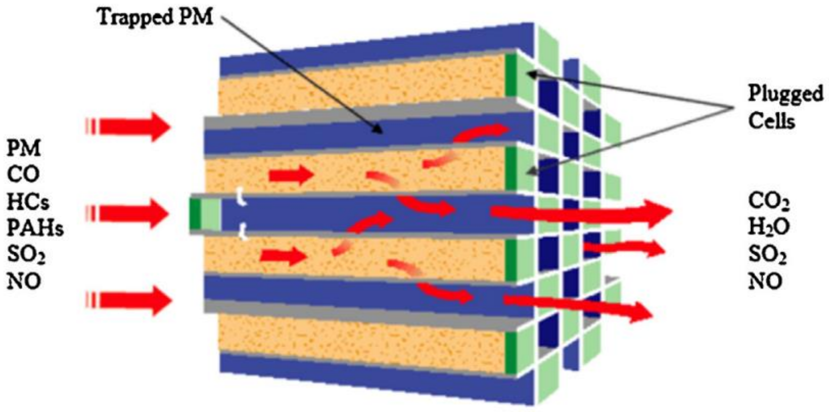

Figure 2. Function of a catalyzed wall flow filter

1.1.8 MRV – ETS

The entry into force of Regulation (EU) No 2015/757 on the Monitoring, Reporting, and Verification of CO_2 emissions (the MRV Regulation) in 2015 marked a significant step forward in the decarburization of the EU's maritime transport sector. The MRV Regulation established rules requiring shipping companies to report annually the amount of carbon dioxide (CO_2) emissions and other relevant information from ships of 5,000 gross tonnage (GT) or above calling at European Economic Area (EEA) ports, and accredited independent verifiers to verify those amounts.

CO_2 emissions are the largest contributor to greenhouse gas emissions from maritime transportation, but methane (CH4) and nitrous oxide (N_2O) emissions are also significant. Starting January 1, 2024, shipping companies must monitor and report methane (CH4) and nitrous oxide (N_2O) emissions in addition to CO_2.Furthermore, beginning January 1, 2025, the MRV Regulation will apply to general cargo ships with a gross tonnage of 400 to 5000, as well as offshore ships with a gross tonnage of 400 or above.

Beginning in 2025, companies must submit an emissions report for each ship under their control for the whole reporting period of the previous year, which has been verified as satisfactory by a verifier in accordance with Article 13 of the MRV Regulation. The emissions report must be submitted via THETIS-MRV to:

- The relevant administering authority
- The authorities of the ship’s flag State (if it is flying the flag of an EEA country)
- The European Commission

Furthermore, beginning in 2025, by the 31st of March of each year, shipping companies must submit an emissions report at the company level (aggregating the data to be reported for ETS purposes at the company level), which has been verified as satisfactory by a verifier in accordance with Chapter III of Regulation (EU) 2015/757.

Under EU's Emissions Trading System, shipping companies will be required to monitor and report their emissions on an annual basis, as well as purchase and surrender ETS emission allowances for each ton of CO_2 emissions reported within the scope of the system. The EU ETS will initially cover CO_2 emissions, but from January 1, 2026, it will also include methane (CH_4) and nitrous oxide (N_2O), using the CO_2 equivalent principle.CO_2 emissions from ships with 5,000 or more gross tonnage that call at or depart from ports in the European Economic Area (EEA), regardless of flag (EEA/non-EEA), are included in the EU's Emissions Trading System (ETS) from January 1, 2024.The expansion of the ETS to maritime transportation includes:

- 100% of emissions from ships calling at an EEA port for voyages within the EEA
- 50% of the emissions from voyages starting or ending outside of the EEA
- 100% of emissions produced when ships are within EEA ports.

The new system will be implemented gradually, and shipping companies will be required to surrender allowances as follows:

- In 2025, for 40% of the emissions reported in 2024
- In 2026, for 70% of their emissions reported in 2025
- From 2027 onwards, shipping companies will have to surrender allowances for 100% of their reported emissions.

The system is based on the MRV maritime regulation and data reported through the THETIS MRV, which is operated and maintained by EMSA. To ensure system compliance, each shipping company will be assigned an administering authority from a Member State. The EU legislation also includes a reporting and review clause to monitor the implementation of maritime sector rules and to consider relevant developments at the International Maritime Organization (IMO) level.

1.2 Methanol

Methanol has been used in industrial applications for over a century, and is now demonstrating great promise as a clean and sustainable future fuel for maritime applications. Methanol (methyl alcohol, CH_3OH, or MeOH) is a biodegradable wood alcohol used to make a variety of products, including plastics, paint, and pharmaceuticals. Methanol is a liquid under atmospheric pressure. Although it is toxic and highly flammable, it dissolves in water and degrades quickly, making it a lesser risk to the environment than many alternatives. Methanol is regarded as a renewable, dependable, and usable energy that exhibits superior physicochemical properties when compared to traditional fossil fuel sources. However, there are still some challenges, such as cold starts, low fuel economy, and elevated unregulated emissions, that need to be addressed before methanol can be widely adopted in engines. The primary advantage of green methanol is that it emits less CO_2 than diesel combustion, as well as lower SO_x and NO_x emissions. The reduction in emissions relates to the engine's load. Switching from diesel to methanol reduces CO_2 (tank-to-wake) emissions by up to 7%, SO_x emissions by up to 99%, and NO_x emissions by up to 60% compared to heavy fuel oil (HFO) operation. When burned as a fuel in a methanol engine, methanol emits 50% less NO_x than fuel oil, allowing the engine to comply with IMO Tier II limits. Methanol is one of the most promising biofuels and has numerous benefits as an alternative fuel for ICEs given its superior chemical and physical properties when compared to traditional fuels. Methanol (CH_3OH) is the simplest alcohol, consisting of a single carbon atom per molecule. Furthermore, it is a colorless, toxic liquid with a faint odor, also known as "methyl alcohol" or "wood alcohol." It is also miscible with the majority of organic solvents, other alcohols, water, and esters, while slightly soluble in oils and fats (Zhen and Wang, 2015, as cited in Zhou et al., 2024). It is also an effective hydrogen carrier. Methanol's lower molecular weight and simple chemical structure lead to lower carbon emissions because lighter fuels exhibit a slower diffusion rate (Yadav et al., 2021, as cited in Zhou et al., 2024). On the other hand, using methanol or mixing methanol with fossil fuel can significantly decrease engine exhaust emissions including NO_x, PM, CO, and CO_2 emissions (Chao et al., 2001; Yusop et al., 2014; Balki et al., 2014, as cited in Zhou et al., 2024). Methanol has a low carbon/hydrogen ratio and more oxygen, which contributes to the improvement of combustion and reduction of exhaust emissions (Liu et al., 2007, as cited in Zhou et al., 2024). Furthermore, methanol is a sulfur-free fuel, unlike diesel fuel, which completely eliminates SO_2 and sulfate (Valera et al., 2020, as cited in Zhou et al., 2024). Additionally, methanol lacks carbon-carbon bonds and the thermal cracking process, minimizing the possibility of smoke creation, which is triggered mainly by thermal cracking of long-chain molecules in air-deprived environments (Lapuerta et al., 2005; Pickett and Siebers, 2004, as cited in Zhou et al., 2024).

Furthermore, methanol displays a higher laminar flame speed and a wider lean-burn limit (Sharudin et al., 2016, as cited in Zhou et al., 2024). Thus, using methanol in engines can decrease NO_x, CO, and HC emissions while improving combustion efficiency and lean-burn limitation (Kowalewicz, 1993, as cited in Zhou et al., 2024). Higher laminar flame speed promotes flame propagation and accelerates the combustion process, improving engine thermal and combustion efficiency. Methanol has the lowest adiabatic combustion temperature. Lower adiabatic flame temperature reduces heat transfer rate and cylinder wall heat loss, which enhances thermal efficiency and reduces NO_x emissions. Methanol's lower heating value decreases both peak combustion temperature and exhaust gas temperature, lowering NO_x emissions (Eyidogan et al., 2010, as cited in Zhou et al., 2024). Additionally, methanol has a higher octane number (OC) compared to conventional fossil fuels, allowing for a higher compression ratio and improved thermal efficiency.

Moreover, methanol lacks a negative temperature coefficient (NTC) region (Haas et al., 2009, as cited in Zhou et al., 2024). As a result, methanol-fueled engines have better knock tolerance and can slightly raise compression ratio, leading to greater efficiency (Kowalewicz, 1993, as cited in Zhou et al., 2024) and fuel economy (Celik et al., 2011, as cited in Zhou et al., 2024). The knock can cause various types of internal combustion engine damage, including cylinder head erosion, cylinder head gasket leakage, piston ring land rupture, cylinder bore scuffing, piston ring sticking, and piston crown melting (Z. Wang et al., 2017). Despite its relatively high knock resistance, methanol is still susceptible to detonation when the compression ratio is too high. It should be mentioned that methanol has a greater latent heat of vaporization, about 3.7 times that of gasoline. This property leads to a lower intake temperature, allowing for increased power output and volumetric efficiency (Arapatsakos et al. 2003, as cited in Zhou et al., 2024). In addition, the higher latent heat of vaporization of methanol can successfully reduce in-cylinder combustion temperature, improving knock resistance and decreasing NO_x emissions (Sharudin et al., 2016; Tian et al., 2022, as cited in Zhou et al., 2024). However, the greater latent heat vaporization of the methanol will result in a cold start problem in the SI engine, especially in low-temperature conditions. Furthermore, it should be noted that methanol is a toxic liquid that is poisonous to people. However, methanol is completely miscible with water and poses a smaller risk in comparison to gasoline in case of a leak (Bozzano and Manenti, 2016 as cited in Zhou et al., 2024). Lastly, methanol is liquid at standard pressure and temperature because of the hydrogen bonding phenomenon induced by the OH characteristic group. Consequently, methanol is easily transportable and storable, with low losses to vehicles and fuel infrastructure.

NO_x emissions

NO_x emissions consist primarily of NO and NO_2 produced during the engine's combustion process. NO formation is primarily affected by increased oxygen levels and temperatures, which are the primary factors that contribute to NO_x emissions (S. Wang et al., 2017, as cited in Zhou et al., 2024). Methanol's high latent heat of vaporization and low heating value lead to lower combustion temperatures in the cylinder, which help prevent NO_x creation in the SI engine.

CO emissions

In general, inadequate oxygen during the combustion process has a significant impact on the engine's CO formation and oxidation (Saxena et al., 2021, as cited in Zhou et al., 2024). This results in incomplete combustion and limits the oxidation of CO into CO_2, thus boosting CO creation. The 50% concentration of oxygen in methanol could optimize engine combustion quality and considerably decrease CO emissions, especially during idle time and low load conditions. Furthermore, higher temperatures can lead to the generation of CO through the dissociation of CO_2 during the combustion process, as a result of chemical reaction equilibrium.

HC emissions

The engine's HC emissions primarily stem from unburned mixtures in crevices, adsorption and desorption of unburned mixture in the lubricant oil, and flame quenching near the combustion chamber wall, among other factors. Methanol, with its significant oxygen levels and elevated laminar flame speed, can decrease the combustion duration of the engine, lowering HC emissions and enhancing combustion efficiency. However, HC formation and oxidation of the engine are also firmly linked to engine type, fuel type, and operating conditions (Yanju et al., 2008, as cited in Zhou et al., 2024).

1.2.1 Methanol demand and retrofitting

Figure 3 depicts the global methanol demand and supply from 2015 to 2023 (Zhen and Wang, 2015; Methanol Institute, n.d.). Evidently, methanol demand and production capacity have increased significantly over the last decade. In 2020, the Methanol Institute confirmed that methanol was available at approximately 100 ports around the world, with this number steadily increasing.

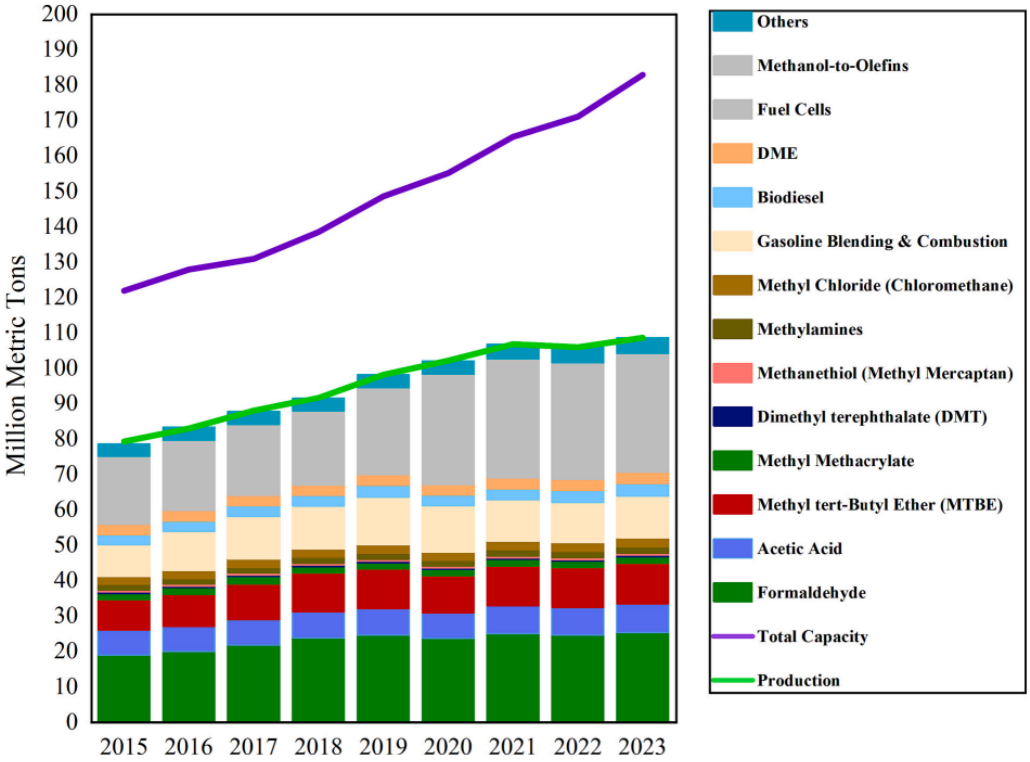

Figure 3. Global methanol demand and supply

Retrofitting methanol technology to an existing engine involves significant changes, particularly in fuel injection technology, engine controls, safety, and automation. In most cases, the starting point is an engine that runs on heavy fuel (HFO) oil or light fuel (LFO). Methanol conversion necessitates modifications to auxiliary devices in the vessel, as well as bunkering arrangements and fuel storage. Each conversion begins with feasibility studies, design, and engineering, followed by engine conversion and the installation of associated equipment such as tanks, piping, and safety systems. In conversion projects, finding space for a methanol fuel tank or container, as well as fuel handling equipment, can be challenging. Whether a vessel can be converted to run on methanol is primarily determined by the amount of space required for tanks and additional equipment. Methanol has a lower energy content than conventional fuels. In practice, this means that additional tanks must be installed onboard to maintain the same level of operational autonomy level. For example, to maintain the same level of fuel endurance as diesel, converting a vessel to run on methanol requires roughly double the fuel tank volume. These tanks can be built using existing fuel tanks or converted ballast tanks. Typical fuel tanks are structurally suitable for methanol. Because of methanol's chemical properties, bunkering requires only minor infrastructure changes, and there is no need for cryogenic storage when converting from conventional marine fuel. Methanol tanks also require extra cofferdams to prevent leaks into machinery spaces. Methanol conversion necessitates additional safety upgrades regarding engine and high-pressure systems. In methanol conversion, a nitrogen generator is required to provide inert gas to the protected areas of pipes and tanks. In terms of onboard safety, the IMO's MSC.1-Circ.1621 - Interim Guidelines For The Safety Of Ships Using Methyl/Ethyl Alcohol As Fuel outlines well-established rules and regulations for using methanol as a marine fuel. Converting an existing vessel to run on methanol is one method for decarbonizing a fleet and improving its EEXI and CII ratings. When building a new vessel, using green methanol can help achieve higher EEDI (Energy Efficiency Design Index) and CII values.

1.2.2 Thermophysical properties of Methanol

Table 1. Thermophysical properties of Methanol (Djermouni & Ouadha, 2023)

Fuel properties	Methanol
Chemical structure	CH_3–OH
Molecular weight (kg/kmol)	32
Density (kg/m3)	798
Boiling Temperature (K)	337.85
Flash Point (K)	284.15
Autoignition temperature (K)	738
Adiabatic flame temperature (K)	2143
Low heat value (MJ/kg)	20
Latent of heat vaporization (kJ/kg)	1160
Octane Number (RON)	109
Stoichiometric air–fuel ratio	6.5
Oxygen content (%) by weight	50%
Kinematic Viscosity (cSt at 20 ◦C)	0.74
Flammability limit (Volume% in air)	6-36

1.2.3 Methanol production technology

Methanol can be produced from both non-renewable and renewable fossil fuels, such as carbon dioxide, biomass, coal, and natural gas.

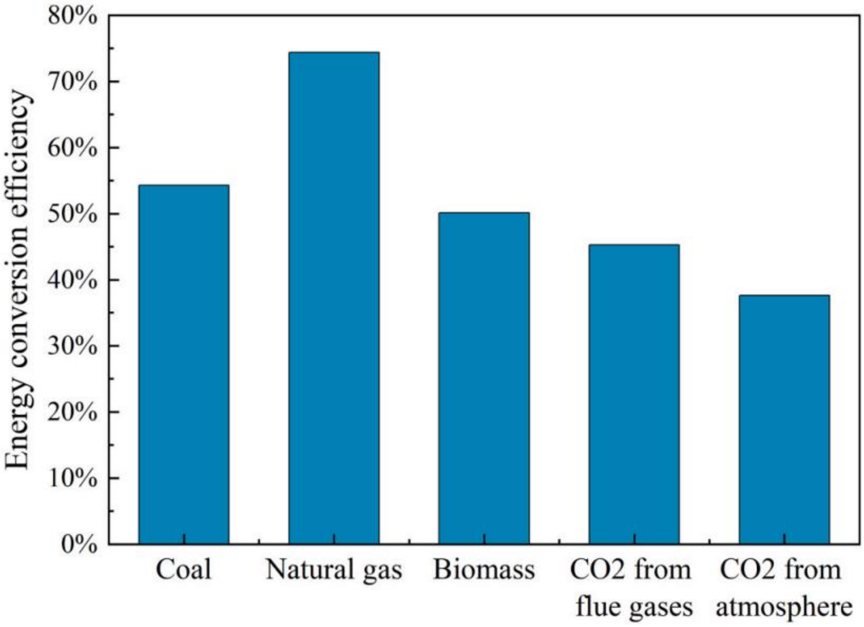

Figure 4. Efficiency of methanol synthesis from different feedstocks (Çelebi and Aydın (2019), as cited in Zhou et al., 2024)

Methanol is a colorless liquid, but color names are used to show what it is made of.

- Green methanol is made from biomass or captured CO_2 and green hydrogen.
- Blue methanol is made by combining blue hydrogen with carbon capture technology.
- Grey methanol is produced by using natural gas.
- Brown methanol is produced from coal.

The CO_2 footprint of methanol varies depending on how it is produced and transported, with fossil-based methanol (grey and brown) emitting more lifetime CO_2 emissions than diesel, whereas green methanol is the most environmentally sustainable and has the potential to be a carbon-free fuel. Blue methanol still significantly lowers well-to-tank CO_2 emissions compared to fossil fuels such as diesel. One of the most significant challenges to maritime decarbonisation is that most methanol today is grey or brown. The methanol molecule, CH_3OH, remains the same whether produced from grey, brown, blue, or green feedstocks. This means that blending methanol is a viable option for facilitating the transition from conventional to renewable marine fuels by gradually increasing the proportion of sustainable green methanol.

Methanol produced from coal and biomass

Coal is China's most abundant energy resource, and coal-based methanol production is vital. To meet future demand, coal production is anticipated to surpass 95 million tons by 2021

(Sonthalia et al., 2021; Harrington and Pilot, 1975, as cited in Zhou et al., 2024). Figure 5 depicts the industrial procedure from coal to methanol (Li et al.,2018, as cited in Zhou et al., 2024). The primary stages of the process are coal gasification for syngas production, crude methanol synthesis, and purification. Nevertheless, using coal-based substances to produce methanol creates significant quantities of carbon dioxide, exhaust gases, and wastewater, all of which contribute to the greenhouse effect and severe pollution of the environment.

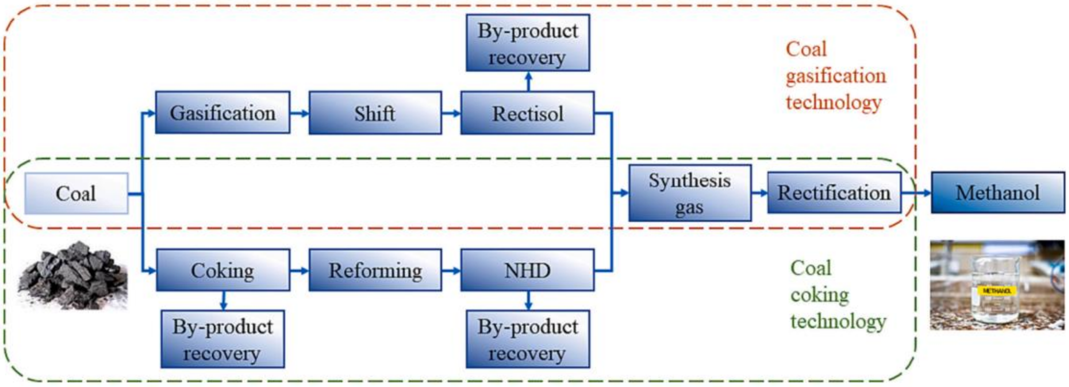

Figure 5. Flow chart of coal to methanol

As a result, many researchers have conducted studies on biomass-based methanol production. Technically speaking, biomass is abundant in carbon atoms. Methanol can be produced from nearly any organic material, like sugarcane, corn, rice straw, biogas, and algae. Therefore, creating methanol from biomass can successfully mitigate the greenhouse effect and environmental pollution. It is essential to note that during the syngas production process, the biomass must be dried and ground. However, large-scale industrial methanol production is currently not feasible because of uneven allocation of biomass resources and high costs.

Methanol produced from natural gas

Nowadays, natural gas is the preferred feedstock for methanol synthesis, accounting for more than 75% of total production (Fletcher et al. 2005, as cited in Zhou et al., 2024). Methanol from natural gas possesses an energy conversion efficiency of more than 70%. Methanol production via natural gas is a more sustainable method. Methanol production from natural gas follows similar steps to methanol production from coal and biomass. Figure 6 depicts a simplified flow chart for the natural gas to methanol procedure (Çelebi and Aydın, 2019, as cited in Zhou et al., 2024).

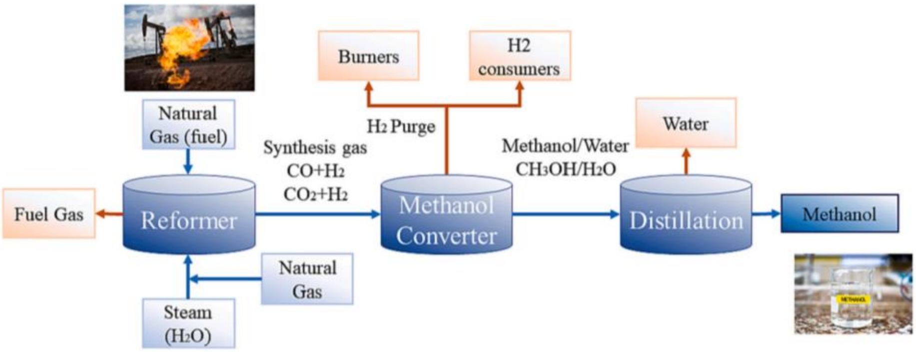

Figure 6. Flow chart of natural gas to methanol

Methanol produced from CO_2

Because of the increasing greenhouse effect and the growing focus on carbon neutrality, the technological path for transforming CO_2 into methanol is receiving increased attention. Furthermore, the utilization of technological paths such as coal-to-methanol, biomass-to-methanol, and natural gas-to-methanol in manufacturing will emit greater amounts of carbon dioxide than the amount of CO_2 required for generating syngas. This will undoubtedly aggravate the greenhouse effect. Olah (2005) and Olah et al. (2011) were among the first to propose combining carbon capture and storage (CCS) with chemical recovery.

Carbon capture and recovery (CCR) is another alternative to CCS. They suggested the notion of a "methanol economy" based on CCR and methanol, which is a renewable, viable, and carbon-neutral cycle, as illustrated in Figure 7 (Kothandaraman et al., 2018, as cited in Zhou et al., 2024). CO_2 is a highly stable compound that has two double bonds between the oxygen and carbon atoms. It that can be stored in liquid form under mild pressure. To produce methanol, CO_2 has to be catalyzed or undergo electrochemical hydrogenation. However, current CO_2 storage technologies are not optimal and are prohibitively expensive.

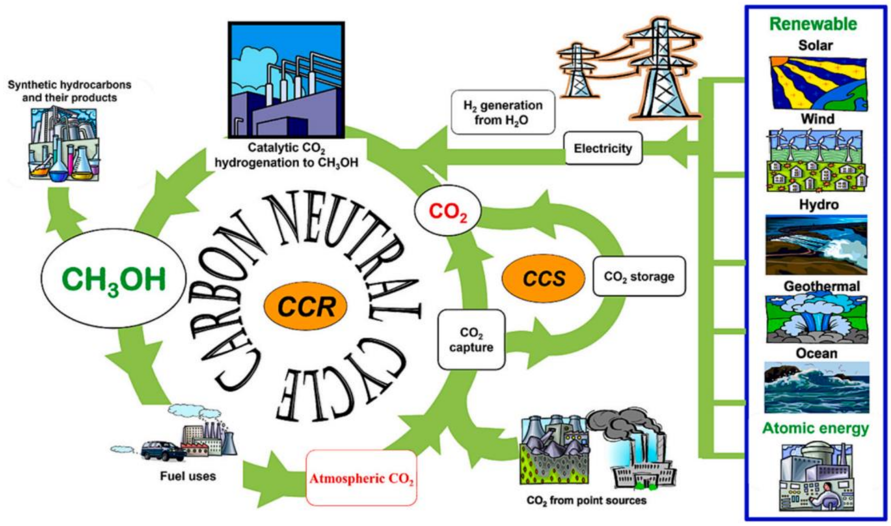

Figure 7. Carbon neutral cycle in the context of the methanol ecomony

A different method to produce methanol from CO_2 is through solar photosynthesis. This not simply eliminates the greenhouse effect, but also allows for highly renewable and viable resources. However, the present technology is insufficient for commercial-scale application. In natural photosynthesis, CO_2 is transformed to carbohydrates, but not to methanol. As a result, many scholars have suggested using artificial photosynthesis to transform CO_2 into methanol. The most important step in artificial photosynthesis is to convert water into protons and electrons using solar energy.

1.2.4 Main challenges for methanol fueled engines

Methanol has the greatest potential as a clean alternative fuel due to its superior physiochemical properties. Nevertheless, methanol's high latent heat of vaporization and low vapor pressure tend to render cold starts challenging for methanol engines. In the twentieth century, scholars discovered that methanol engines equipped with carburetors suffer from serious wear issues during the cold start state, which constitutes a significant part of the total wear. This was triggered by methanol spray striking the cylinder walls during the first brief period of engine startup (Nautiyal et al., 1985, as cited in Zhou et al., 2024). Additionally, methanol is a single-component fuel with a consistent boiling point and lacks volatile components, which may enhance cold-start performance. Moreover, methanol has a high latent heat of vaporization, meaning it requires greater amounts of energy to vaporize. Thus, the engine will be hard to start. Another significant challenge of the methanol engine is the generation of substantial quantities of exhaust emissions during cold start, including CO, HC, formaldehyde (CH_2O), and unburned methanol. Approximately 50-80% of CO and HC emissions occur during the first cycle of engines at cold start (Gong et al., 2008a, as cited in Zhou et al., 2024). Unregulated emissions, particularly formaldehyde, will be significantly produced in the methanol engine and are primarily affected by the in-cylinder temperature during the cold start state. Furthermore, corrosion caused by the material compatibility of methanol is another issue. Methanol can corrode both ferrous and non-ferrous metals to varying degrees (Yuen et al., 2010, as cited in Zhou et al., 2024) and temperature significantly impacts the corrosion process (Turner et al. 2012, as cited in Zhou et al., 2024). Furthermore, methanol, as an alcoholic fuel, causes swelling, shrinkage, hardening, or softening of the fuel system's elastomers.

Methanol displays an extremely low heating value. The heating value of the fuel has a direct impact on brake specific fuel consumption (BSFC) (Awad et al., 2017, as cited in Zhou et al., 2024). This means that more methanol fuel is required to generate the same amount of heat as gasoline. Moreover, methanol displays substantial chemical resistance to auto-ignition because of its single-stage auto-ignition behavior (Yates et al., 2010, as cited in Zhou et al., 2024). Methanol has a greater auto-ignition temperature compared to that of conventional fuels. The temperature at which combustion occurs without an ignition source is referred to as the auto-ignition temperature. On the other hand, the auto-ignition delay time is defined as the period of time it takes for a homogeneous and quiescent mixture to auto-ignite. As a result, methanol is regarded as more appropriate for SI engines (Sayin et al., 2008, as cited in Zhou et al., 2024) which can use a relatively high compression ratio or slightly advance the spark timing. Lastly, methanol costs can be up to 15 times higher than diesel operation, depending on the type of methanol used, its price, and the proportion of energy provided by methanol. Although fuel costs are higher with methanol than with diesel, this should be considered in light of today's regulatory landscape. Vessels that do not meet the CII and EEXI targets will no longer be allowed to operate. So the additional fuel cost should be compared not only to today's fossil fuel prices but also to the cost of a brand new and more efficient ship, as well as the potential losses from a mandatory stop of operations.

1.3 Supercritical CO_2 Applications

Supercritical fluids (SCFs) have properties that differ significantly from those of real fluids. Supercritical fluids are not liquids or gases but rather substances that are in a "supercritical state" above their critical temperature (Tc) and pressure (Pc). Supercritical carbon dioxide (sCO2) is a nonpolar medium with a high quadrupole moment. Its critical point occurs at 7.38 MPa, 304 K (31.1 °C), and 73.8 bar (Budisa & Schulze-Makuch, 2014). Its density varies with temperature and pressure. At critical pressure, its compressibility is maximized and slight changes in thermal parameters can significantly impact its local density.

Carbon dioxide has four distinct phases: solid, liquid, gas, and the supercritical phase. A substance is considered a supercritical fluid if its temperature and pressure exceed the critical temperature (Tc) and pressure (Pc) of the substance, respectively. Carbon dioxide transitions to the supercritical phase at the critical points of 7.38 MPa, 304 K (31.1 °C), and 73.8 bar.

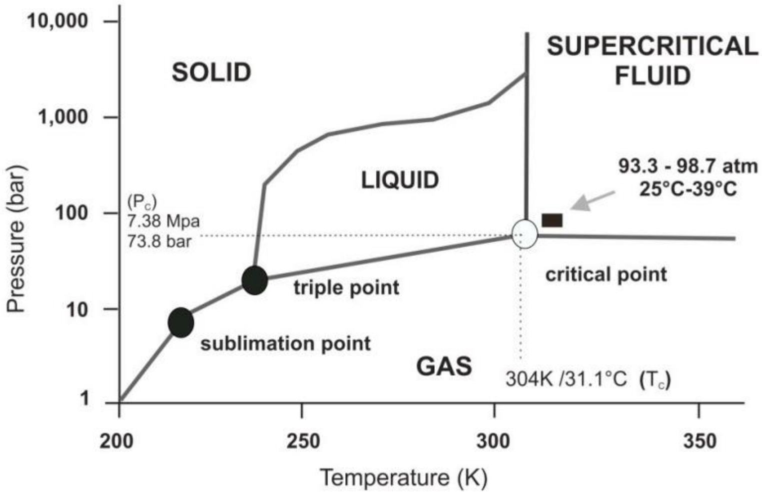

Figure 8. Schematic p-T phase diagram of CO_2 (Budisa & Schulze-Makuch, 2014)

1.4 Modeling and simulation of combustion chemistry

Recent advances in the field of chemical kinetics have resulted in the intricate exploration of reaction mechanisms, particularly in the study of hydrocarbon combustion. These mechanisms unravel the fundamental steps involved in transforming reactants into products in the context of an overall reaction. The primary motivations for developing detailed mechanisms are a more complete representation of chemical processes and the ability to produce satisfactory results over a wider range of pressure, temperature, and fuel-air equivalence ratio conditions. However, the development of skeletal mechanisms, which contain a subset of chemical compounds and reactions compared to detailed mechanisms, is considered necessary for the thorough study of complex aerothermochemical phenomena. This is due to the necessity of coupling chemical kinetics mechanisms with Computational Fluid Dynamics codes, and the inclusion of a detailed mechanism is deemed prohibitive in terms of computational cost.

1.5 Motivation and Objectives of Present Study

The subject of this thesis is the study of methanol combustion in supercritical conditions and the evaluation of a skeletal chemical kinetic mechanism for methanol combustion. The process followed is divided into three stages: (i) Evaluation of the skeletal mechanism, (i) Evaluation of the skeletal mechanism for CO_2 use in supercritical conditions as a diluent, and (C) Chemical Analysis.

The first step in the assessment process involves collecting experimental data for a wide range of pressure, temperature, and fuel-air equivalence ratio conditions. The experimental data is divided into three major categories. The first category concerns concentration profiles of significant chemical compounds as a function of temperature in a perfectly-stirred reactor for CH_3OH combustion. The second category involves ignition delay time in autoignition phenomena, and the third category pertains to the laminar flame speed of premixed preheated mixtures.

Following that, two chemical kinetic mechanisms were collected, one detailed and one skeletal. The detailed mechanism used is the Hp-Mech, developed at Princeton, while the skeletal mechanism is the Pichler-Nilsson, developed at Lund University in Sweden and referred to as ACR55.

The skeletal mechanism is assessed by comparing its results to those of a detailed mechanism and determining its accuracy in approximating experimental data. The skeletal mechanism produced quite satisfactory results under conditions relevant to maritime applications.

The same procedure is followed when using CO_2 as a diluent in supercritical conditions. Simulations for the two mechanisms are performed at high pressures and temperatures over a significant range of fuel-air equivalence ratios.

Finally, the chemical analysis process for the skeletal mechanism and the three standard problems was conducted for a representative set of pressure, temperature, and fuel-air equivalence ratio conditions, covering the overall range of experimental conditions. Significant reactions and important chemical compounds involved in these reactions were identified through chemical analysis.

1.6 Literature

A literature review has been performed to identify experimental and computational studies of relevance to the present study of methanol combustion. The most important works are summarized next.

In the work of Wang et al., a study on methanol combustion at high pressures in a supercritical pressure jet-stirred reactor is presented. Experimental data were collected from this work regarding concentration profiles of the chemical compounds CH_3OH, CO_2, CO, H_2O, CH_2O, and H_2 as functions of temperature. The range of conditions for the specific experimental data mentioned is: P=10atm & 100atm, T=550-950 K, and φ=0.1, 1.0, and 9. Additionally, experimental data are obtained from the work of Burke et al., where methanol combustion in a jet stirred reactor is studied under low and medium pressures. The range of conditions for the specific experimental data mentioned is: P=10atm & 20atm, T=550-950 K, and φ=0.2, 0.5, 1, 2.

Burke et al. also studied ignition delay time during methanol combustion. Experimental data were collected from this work for the following range of conditions: P=1.96-51 atm, T=950-1475 K, and φ=0.5, 1, and 2.

In the works of Zhang et al. and Vancoillie et al., premixed flame speed during methanol combustion is studied. Data were collected from the aforementioned works for the following range of conditions: P=1-10bar, T=298-423 K, and φ=0.7-1.5.

At this point, it needs to be noted that no experimental data were found for methanol combustion under supercritical conditions with the addition of CO_2 in the literature.

1.7 Thesis Structure

The present thesis focuses on the investigation of methanol combustion under supercritical conditions. In this context, a skeletal mechanism is being validated against experimental data and compared to a detailed mechanism. The structure of the thesis is described below.

Chapter 1 outlines the issue of pollution, as well as the methods and global regulations that are being implemented to address it. A brief overview of methanol, its fundamental properties, and the challenges that arise in its applications is also provided.

Chapter 2 serves as an introduction to basic Chemical Kinetics theory. Moreover, the experimental setups for the three standard problems used to evaluate the skeletal chemical kinetic mechanism are described. These problems include (a) laminar premixing flame, (b) ignition delay problems, and (c) perfectly stirred reactor (PSR) problems.

Chapter 3 introduces the results from simulations for the two mechanisms over a wide range of pressure, temperature, and fuel-air equivalence ratios, representative of the operation of dual-fuel marine engines. A comparison with experimental data from the literature is made.

Chapter 4 presents the results from simulations for the two mechanisms, this time using CO_2 as a diluent in supercritical conditions, covering a wide variation of high pressures, high temperatures, and equivalence ratios.

Chapter 5 refers to the chemical analysis conducted for the skeletal mechanism for all three standard problems, covering a wide range of pressure, temperature, and fuel-air equivalence conditions. The goal is to identify key chemical processes and significant chemical pathways through rate-of-production (ROP) analysis for a representative selection of cases.

Chapter 6 concludes the present work by summarizing the observations and results of this study.

CHAPTER 2: Fundamental Concepts - Experimental Setups

2.1 Chemical kinetics

The branch of chemistry that studies the speed (or rate) at which a chemical reaction progresses, the factors influencing the speed of a reaction, and the mechanism of a reaction is called chemical kinetics. The speed of chemical processes depends on the mechanism, stoichiometry, and initial conditions of pressure and temperature. The study of the combustion phenomenon is related to understanding the fundamental reaction steps that a hydrocarbon follows in the presence of oxygen or air. The aforementioned reactions occur at a high speed, are exothermic, and result in the release of heat.

The reaction rate is proportionate to the rate of change of the concentration of reactants or products per unit time. The speed of a reaction depends on the following factors:

1. The nature of the reactants.
2. The concentration of the reactants: Higher concentration of reactants leads to an increase in collisions among reactant molecules, consequently resulting in an increase in effective collisions and, hence, an increase in the reaction rate.
3. Pressure: Increasing the pressure for reactants in gaseous form results in an increase in concentration and ultimately an increase in the reaction rate.
4. Surface area of reactants for solids: Increasing the surface area leads to an increase in the reaction rate. Therefore, reactants are preferred in powdered form if they are solids.
5. Temperature of the reactants: Increasing the temperature results in an increase in the reaction rate. At higher temperatures, the particles of the reactants have higher velocities, leading to more collisions. Typically, a 10°C increase in temperature is required to double the reaction rate.
6. Presence of radiation: Results in an increase in the speed of some reactions.
7. Presence of catalysts: A catalyst is a substance that increases the speed of a reaction without being consumed in the overall reaction.

It is worth noting that, in general, slow elementary reactions have a greater impact on the overall phenomenon.

The law of mass action is the mathematical expression used to calculate the instantaneous rate of a reaction.

For example, for the following reaction:

$$eE + fF \rightarrow gG + hH$$

The reaction rate is calculated using the following relationship:

$U=k(T)[E]^e[F]^f$, where k(T) is the specific rate constant of the reaction, [E] and [F] are the concentrations of the reactants, and e, f are the stoichiometric coefficients of the reactants. The value of the specific rate constant of the reaction, also known as the Arrhenius constant, depends on the nature of the reactants and the temperature. The unit of measurement for the specific rate constant $k(T)$ changes according to the order of the reaction. Specifically, when the reaction order is first order, the units of $k(T)$ are sec^{-1}, while for second order, the units are m^3/mol sec. The reaction order is defined as the sum of the stoichiometric coefficients of the reactants, i.e., for the specific example e+f. The Arrhenius equation, used to calculate the specific rate constant *k*, is as follows:

$k(T)=A\cdot e^{-\frac{E_a}{RT}}$

Where *A* is the pre-exponential factor, E_a is the activation energy, *R* is the gas constant, and *T* is the absolute temperature. The units of the pre-exponential factor *A* are the same as the units of the specific rate constant *k* and depend on the order of the reaction. For a clearer understanding of the above mathematical relationship, *A* is considered to be the total number of collisions, and the factor $e^{-\frac{E_a}{RT}}$ indicates the percentage of collisions that are successful. Thus, the specific rate constant is used to calculate the number of collisions that result in a reaction.

For a reaction to occur, the atoms of the reactants must collide appropriately to cause the breakdown of the initial chemical compounds, leading to the formation of new chemical compounds and the progression of the chemical process. The total collisions that take place are numerous, but only a few of them are effective. The conditions for a collision to be effective and for the reaction to occur are: (a) The colliding particles must have at least the activation energy E_a, and (b) They must have a suitable orientation.

Additionally, with the change in temperature, the total number of collisions that occur changes without altering the percentage of effective collisions. Thus, an alternative form of the Arrhenius equation is as follows:

$k(T)=A'\cdot T^n$, where *n* is an appropriate exponent of temperature.

2.2 Assumptions about chemical kinetics

Regarding the phenomenon of combustion, there are several common characteristics that appear in different systems and different mechanisms. These characteristics include:

1. The presence of free radicals, which are reactive and have a short lifespan.
2. The presence of a subset of reactions that reach equilibrium before the completion of the overall phenomenon.

To simplify the overall chemical mechanism, assumptions are made about the steady state and partial equilibrium.

2.2.1 Steady-state assumption

In the assumption of the steady state, we consider that free radicals, chemical compounds that are reactive and are rapidly consumed upon their creation, maintain a constant concentration throughout the duration of the phenomenon. Specifically, for the combustion phenomenon, the rate of change in the concentration of free radicals is considered zero, as they are rapidly consumed from the moment they are created. This allows for the simplification of a chemical kinetic mechanism. In the example below, the theory of the steady state is applied. Let's consider a chain of two reactions as shown below:

$$S_1 \xrightarrow{k_{12}} S_2 \xrightarrow{k_{23}} S_3$$

The change in concentration is calculated using the following relationships:

$$\frac{d[S_1]}{dt} = -k_{12}[S_1]$$

$$\frac{d[S_2]}{dt} = k_{12}[S_1] - k_{23}[S_2]$$

$$\frac{d[S_3]}{dt} = k_{23}[S_2]$$

Considering that the compound S2 is reactive and rapidly consumed, the rate of change of its concentration is zero. Therefore, we can calculate the change in the concentration of the final product as a function of the concentration of the chemical compound S1.

$$\frac{d[S_2]}{dt} = k_{12}[S_1] - k_{23}[S_2] \approx 0$$

$$\frac{d[S_3]}{dt} = k_{12}[S_1]$$

2.2.2 Partial equilibrium assumption

In the assumption of partial equilibrium, we consider that a subset of reactions reaches equilibrium before the completion of the overall phenomenon. A characteristic example in the combustion of hydrocarbons is the hydrogen-oxygen system. At high temperatures, the value of the specific rate constant (k) is high. This results in a subset of reactions attaining a high speed, causing this subset to reach equilibrium faster. For example, we consider a system of three reactions:

$$H + O_2 \leftrightarrow OH + O \ \ (k_1, k_2)$$

$$O + H_2 \leftrightarrow OH + H \ \ (k_3, k_4)$$

$$OH + H_2 \leftrightarrow H_2O + H \ \ (k_5, k_6)$$

Assuming that the system has reached equilibrium, we have:

$$k_1[H][O_2] = k_2[OH][O]$$

$$k_3[O][H_2] = k_4[OH][H]$$

$$k_5[OH][H_2] = k_6[H_2O][H]$$

And solving for the concentrations of free radicals (O, OH, H), the following relationships are obtained:

$$[H] = \left(\frac{k_1 k_3 k_5^2 [O_2][H_2]^3}{k_2 k_4 k_6^2 [H_2O]^2} \right)^{\frac{1}{2}}$$

$$[O] = \left(\frac{k_1 k_5 [O_2][H_2]}{k_2 k_6 [H_2O]} \right)$$

$$[OH] = \left(\frac{k_1 k_5 [O_2][H_2]}{k_2 k_4} \right)^{\frac{1}{2}}$$

In this way, the concentration of free radicals can be calculated by measuring the concentrations of the remaining elements. The assumption of partial equilibrium is applied for the calculation of concentrations of chemical compounds that are difficult to measure through experimental setups.

2.3 Premixed laminar flame structure-Mallard-Le Chatellier analysis

In premixed flames, fuel and oxidizer are mixed before the flame front propagates. In the case where the heat generated by combustion is used to heat the combustion products, the flame is called adiabatic. The assumption of adiabatic flame is mainly used in the analysis of one-dimensional premixed flames.

The oxidizing agent in combustion is mainly atmospheric air (i.e., 21% O_2, 79% N_2). For combustion to occur, the fuel-air equivalence ratio must be within specific limits known as flammability limits. For given conditions, flammability limits are defined as the two extreme values of stoichiometry within which combustion of the mixture can take place.

The laminar flame speed of premixed flames, denoted as SL, is defined as the relative speed of the flame front to the unburned mixture. The value of laminar flame speed depends not on the flow but on the conditions and stoichiometry. The flame stabilizes when the mixture velocity equals the laminar flame speed.

Figure 9 illustrates the temperature distribution along the premixed flame. The flame is divided into two zones: the reactants' preheating zone (Zone I) and the reaction zone (Zone II).

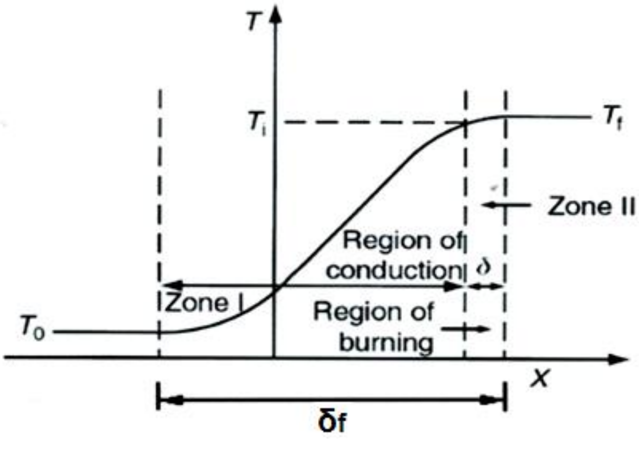

Figure 9. Temperature distribution along the premixed flame

According to the analysis of Mallard and Le Chatellier, a significant factor in the propagation of premixed flames is the heat transfer from the reaction zone to the preheating zone. Part of the released energy is conducted to heat the unburned mixture up to the ignition temperature (T_i). Assuming the temperature change in the reaction zone is linear, the spatial derivative of temperature can be calculated from the expression [($T_f - T_i$)]/δ], where T_f is the final exit temperature, T_i is the ignition temperature, and δ is the reaction zone thickness.

The thermal power balance (energy conservation) in the reaction zone is:

$$\dot{m}c_p(T_i - T_0) = \lambda\left[\frac{(T_f - T_i)}{\delta}\right]A_1$$

Where $\dot{m}$ the mass flow rate of the unburned mixture is [kg/s], c_p is the specific heat capacity of the mixture [J/KgK], T0 is the initial temperature of the mixture [K], λ is the thermal conductivity coefficient [W/mK], and A is the area of the interface between the two zones [m^2].

The mass flow rate equation is:

$$\dot{m} = \rho u A_1 = \rho S_L A_1$$

Where ρ is the density of the mixture [kg/m^3] and $u=S_L$ is the relative velocity of the unburned mixture with respect to the flame front [m/s]. Thus, Equation 8 takes the following form:

$$S_L = \left[\lambda\frac{T_i - T_f}{\rho c_p(T_i - T_0)}\right]\frac{1}{\delta}$$

The total mass flow rate of the unburned mixture per unit surface area is equal to that participating in the reaction zone.

$$\frac{\dot{m}}{A_1} = \rho u = \rho S_L = \dot{\omega}\delta$$

Where $\dot{\omega}$ is the rate of reaction in terms of mass per unit area.

Therefore, equation 10 takes the following form:

$$S_L = \left\{\left[\lambda\frac{T_i - T_f}{\rho\, c_p\,(T_i - T_0)}\right]\frac{\dot{\omega}}{\rho}\right\}^{1/2} \sim \left(\alpha\frac{\dot{\omega}}{\rho}\right)^{1/2}$$

Where $\alpha = \frac{\lambda}{\rho\, c_p}$ is the thermal diffusivity coefficient of the unburned mixture.

From the above analysis, it follows that:

$$\delta \sim \frac{\alpha}{S_L}$$

After the reaction zone, it can be considered that there is a third zone where recombination reactions of free radicals take place. However, the concentrations of free radicals in this zone are small, and although these reactions are exothermic, the temperature practically does not change.

2.4 Influence of parameters on laminar premixing flame velocity

2.4.1 Effect of unburned mixture temperature

The laminar flame speed of pre-mixed flames increases with the temperature of the unburned mixture. This trend is attributed to the fact that an increase in temperature reduces density, increases the overall reaction rate, and, based on equation (12), results in an increase in laminar flame speed. The laminar flame speed is also influenced by the adiabatic flame temperature (TF), as higher values favor dissociation reactions, leading to an increase in laminar flame speed [19].

2.4.2 Effect of pressure

The dependence of the laminar flame speed of premixed flames on pressure is derived from equation (12). For gases, it holds that $\alpha \sim 1/p$ and $\rho \sim p$, resulting in:

$S_L \sim p^{\frac{n-2}{2}}$ (14)

Where n is the reaction order. For n=2, the laminar flame speed of premixed flames is independent of pressure, while for n>2, an increase in pressure leads to an increase in S_L. Similarly, for n<2, an increase in pressure results in a decrease in S_L.

2.4.3 Effect of stoichiometry

The dependence of the laminar flame speed of premixed flames is due to the strong influence of the adiabatic flame temperature on the fuel-air equivalence ratio. For hydrocarbon fuel blends, the maximum adiabatic flame temperature occurs for stoichiometric or slightly fuel-rich mixtures. Therefore, for equivalence ratios near unity, maximum values for laminar flame speed of premixed flames are obtained, as reflected in the results obtained in this study.

2.5 Experimental Devices

In this study, simulations were carried out to estimate the ignition delay time, and laminar premixing flame speed and concentration profile of important chemical compounds during methanol combustion as a function of temperature. The simulation results were compared to the corresponding experimental measurements from the literature. The experimental arrangements for each type of simulation are described below.

2.5.1 Jet Stirred Reactor – JSR

The Jet Stirred Reactor (JSR) is used to determine the concentration profile of chemical compounds that participate in combustion as a function of temperature, pressure, residence time, and stoichiometry. During this study the concentration profile was generated as a function of temperature. The JSR system consists primarily of a system for fuel injection (vaporization tank, syringe pump), a temperature control system (temperature control of reactor and gas path), a gas route and control system, a jet stirred reactor, and a system for detection (Gas Chromatograph Mass Spectrometer, GCMS), as illustrated in Figure 10 (Wang et al., 2023).

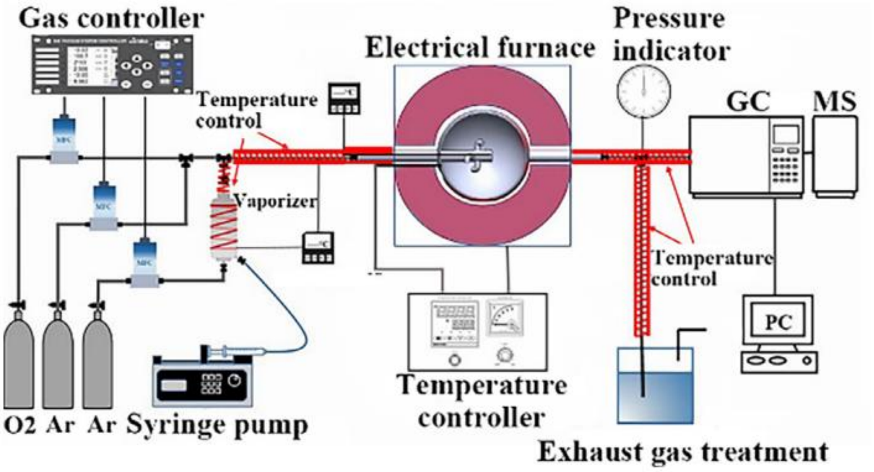

Figure 10. Schematic of JSR system

The JSR is composed of a fused silica sphere and turbulent jets in the center of the sphere, which offer stirring to ensure perfect mixing within the reactor. The Jet Stirred Reactor operates on the basis of efficient mixing of the reactant gas phase, resulting in homogeneous gas synthesis within the reactor. It operates under permanent state conditions, which means that pressure and temperature stay constant throughout the process. This study examines the oxidation characteristics of methanol in a jet-stirred reactor under a wide range of temperatures, pressures, and equivalence ratios with residence times (τ) of 2 s.

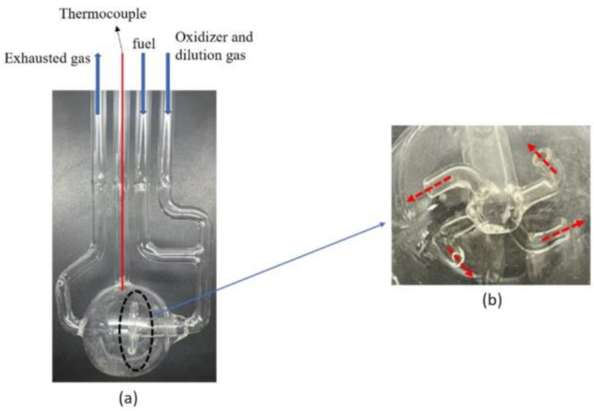

Figure 11. (a) JSR main body, (b) JSR nozzles

According to Burke et al. the JSR used in the experiments is a fused silica sphere with a diameter of 4 cm and an inner volume of 35 cm^3. It is equipped with four l-mm diameter nozzles for admitting the gases that are used to stir. It is located within an oven, which consists of two separate insulated heating cables placed in a stainless-steel pressure-resistant jacket stuffed with insulating ceramic wool. A controlled nitrogen flow in the reactor's outer region regulates the pressure within the JSR. Mass flow controllers deliver all of the gases. A high-pressure liquid chromatography pump delivers the liquid fuel to an in-house vaporizer, which produces a homogeneous nitrogen-methanol blend that flows via a fused silica capillary until it reaches the mixing point before entering the reactor. To prevent reactions prior to the reactor, methanol was diluted with a nitrogen flow of 100 L/h. Preheating all gases prior to the injection reduces temperature gradients within the JSR. The experiments in this study were carried out at varying temperatures and a constant mean residence time. A significant level of dilution was used to decrease temperature gradients and release of heat within the JSR, allowing for steady-state operation. Molecular species were quantified using several gas chromatographs (GC).

According to Wang et al. the main component of JSR is a spherical quartz reactor with an inner volume of 0.4 cm^3. The reactor's unique feature is its four jet fingers, each with two 0.2 mm inner diameter perpendicular nozzles capable of producing powerful turbulence and homogeneous blending. High-pressure mass flow controllers determined the gas flow rates, while a high-pressure syringe pump injected liquid fuel into a vaporization line. Axial temperature profiles were acquired in 1 mm steps across the reactor bulb to confirm the uniform temperature distribution (+/−3 K) under experimental conditions. A quartz sonic nozzle was utilized for sampling the products of oxidation exiting the reactor, and the gas samples were measured using micro gas chromatography. The flow residence time is calculated as the ratio of the reactor's volume to mixture volume flow rate at every temperature and pressure.

2.5.2 Shock tube

The ignition delay time is calculated with the experimental shock tube device. First, a high-pressure inert gas is pumped into the driver section. The fuel is pumped into the driven part position at the desired stoichiometry with steam air. When the fuel and oxidising agent are completely mixed, the ignition delay time measurement procedure begins. An aluminum diaphragm separates the driver's seat from the driver's position. When this diaphragm breaks, a shock wave travels through the combustible mixture, causing an immediate rise in pressure and temperature. The ignition delay time is defined as the time between the spread of the shock wave and the highest rate of change in pressure or the highest concentration of a free radical, which signifies that ignition has occurred. Figure 12 illustrates this kind of arrangement.

According to Burke et al. two ST facilities have been used in this study. The high-pressure ST used is an updated version of that described in detail by Darcy et al. It has an inner diameter of 6.35 cm, a driver section 3.0 m long which is separated from the driven section, 5.70 m in length, by a double diaphragm section (3 cm in length) which houses two pre-scored aluminum diaphragms. It is equipped with six PCB113B24 pressure transducers mounted axially along the side-wall and one Kistler 603B transducer in the end-wall to determine ignition delay measurements from the sharp increase in pressure due to ignition.

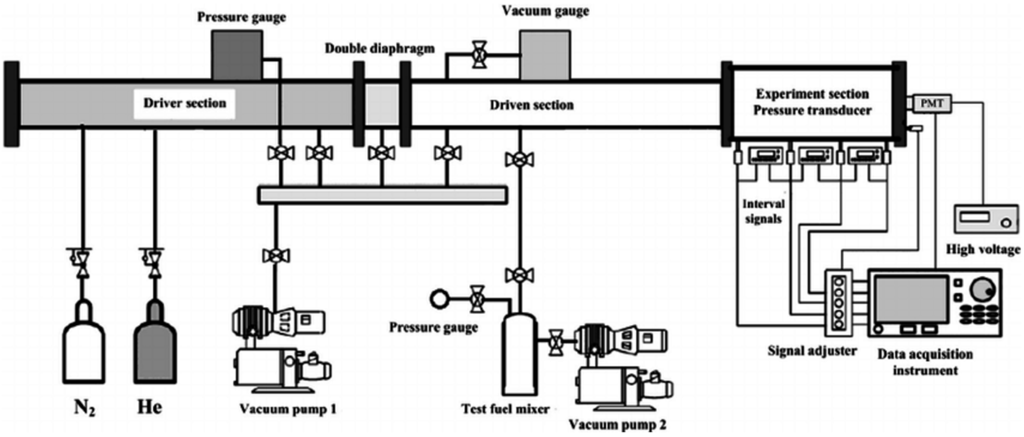

Figure 12. Schematic of Shock tube

2.5.3 Experimental setups for laminar burning velocity measurements

Several experimental setups can be used to measure the laminar burning velocity of fuels, including flat flame burners, combustion chambers, counterflow burners, etc.

In the case of the combustion chamber the experimental setup includes a combustion chamber with a constant volume and systems for heating, ignition, data acquisition, and high-speed schlieren photography. Figure 13 depicts the combustion chamber, which is a cylinder with an inner diameter of 180 mm and a volume of 5.5 liters (Zhang et al., 2008). The combustible mixture is ignited by electrodes located in the center. The chamber body houses the pressure transmitter, thermocouple, pressure transducer, liquid fuel injection valve, as well as the inlet and outlet valves. The vessel has two 80 mm diameter quartz windows placed on each side. As mentioned by Zhang et al. during the combustion, a high-speed digital camera (HG-100K) with a frame rate of 10,000 frames per second captured flame progression. A mercury manometer controls the partial pressures of every component if the initial pressure of the mixtures in the vessel is below or equal to 0.1 MPa. The pressure transmitter controls the partial pressures when the initial pressure exceeds 0.1 MPa. A 2.4 kW heating tape wrapped outside the chamber body heated the entire vessel. The thermocouple has an accuracy of 1 K when measuring the initial temperature of mixtures in the vessel. A thermo-regulator adjusts the initial temperature. As soon as the mixture reaches the desired initial temperature, the power is turned off. The necessary liquid fuel is introduced into the chamber at the specified initial temperature, pressure, equivalence ratio, and dilution ratio.

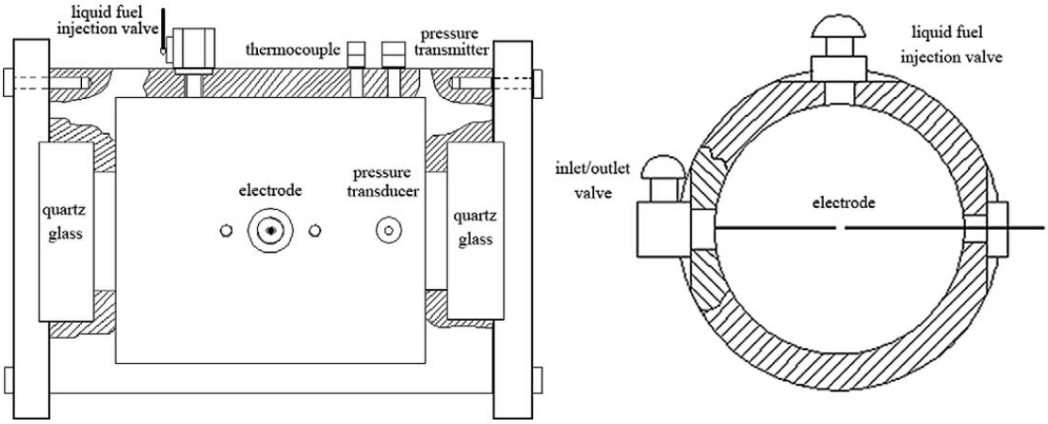

Figure 13. Constant volume combustion chamber

In Beeckmann et al. the closed-vessel method was used to collect experimental data at high pressures and temperatures. The pressure vessel's internal shape is spherical, with an inner diameter of 100 mm, and quartz windows with a diameter of 50 mm are located on opposite sides. A Schlieren cinematography system is used in conjunction with a high-speed CCD camera to image the flame's outward location. The camera covers a 50x50 mm^2 area at an image resolution of 384 x 384 pixels and a frame rate of 5000 frames per second. The Schlieren system includes a HeNe laser with a wavelength of 632.8 nm as a source of light, a microscope objective, a polariser for regulating the intensity, spherical lenses, a 0.6 mm diameter pinhole, and an optical filter to prevent the camera from being overexposed to flame radiation. An external mixing vessel, connected to the combustion chamber through pipes, is used to prepare the air/fuel mixture outside of the combustion chamber. A narrow needle valve connects the fuel storage tank and the mixing vessel. To prevent fuel condensation, the fuel storage tank, the external mixing vessel, and all fuel-contact pipes are heated. The necessary fuel amount can be determined as a function of equivalence ratio, temperature, and pressure. Therefore, the partial pressure method can be utilized in order to precisely determine and regulate the filling process. Technical air, used as an oxidizer, is gradually introduced into the mixing vessel under an isothermal state until the desired pressure is achieved. The quantity of fuel/air mixture prepared in the external mixing vessel is sufficient for multiple successive runs in the combustion vessel. This ensures a clearly defined mixture for every equivalence ratio. The heaters are turned off before sparking, and the mixture has time to settle. The mixture is ignited at the center of the vessel via a two-step ignition system with 1 mm diameter extended spark plug electrodes. The temperature and pressure of the fuel/air mixture inside the combustion vessel before ignition were set to 373 K and 10 bar, respectively. The temperature was regulated via K thermocouples, and the pressure was tracked via Kistler absolute pressure sensors 4045A2, 4075A50, and 4075A100. The experiments were carried out with equivalence ratios ranging from 0.7 to 1.3. Figure 14 depicts the experimental setup schematically.

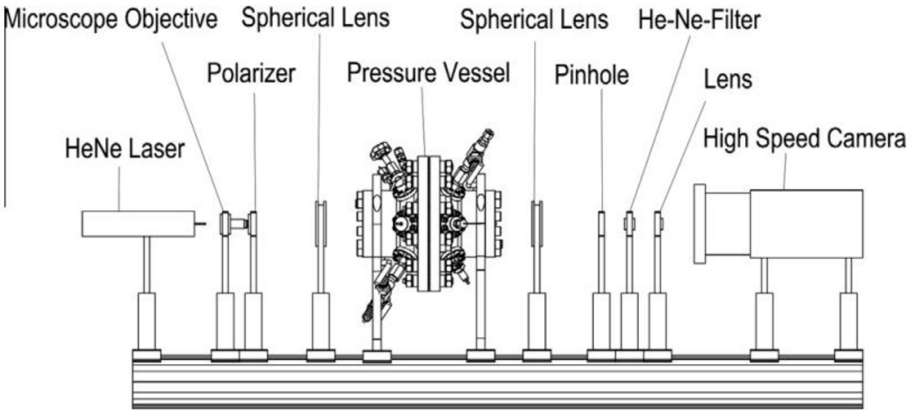

Figure 14. Schematic of the experimental setup

De Goey et al. proposed the heat flux method for stabilizing adiabatic premixed laminar flames on a flat flame burner. As stated in Vancoillie et al. the burner outlet is fitted with a 2 mm thick burner plate perforated with small holes (0.5 mm in diameter). The burner head has a heating jacket that is supplied with thermostatic water to maintain the burner plate temperature constant. Throughout the experiments, this temperature (T1) was set to 368 K. The plenum chamber includes a different temperature control system that is supplied with water at a constant temperature (T0), allowing the fresh gas mixture to be heated between 298 and 358 K. The heating jacket maintains the burner plate edges at a temperature higher than the initial gas temperature, heating the (unburned) flow of gases. The flame's conductive heat transfer to the burner plate cools the gas flow as it turns back. When the flow rate of the gas mixture changes, a proper value of gas velocity can be estimated to cancel out the net heat flux. In this case, the radial temperature distribution in the burner plate is uniform and matches the temperature of the heating jacket. Bosschaart and de Goey provided a theoretical study of the heat flux method, demonstrating that a parabolic function can be used to approximate the temperature profile of the burner plate.

$$T_p^r = T_c - \frac{q}{4\lambda_p h} r^2 = T_c + \mathrm{C}r^2$$

,where Tp(r) is the mean temperature of the perforated plate (averaged over the burner thickness) at radial position r, Tc is the thickness averaged temperature of the perforated plate at the center of the plate (r = 0), h is the thickness of the perforated plate (h = 2 mm), λp is the heat conductivity of the plate, and q is the net heat flux (the difference between the heat flux from the flame to the plate and the heat flux from the plate to the unburned mixture).

A number of thermocouples linked to the burner plate measure temperature distribution at various radial positions. The interpolated flow velocity at which the net heat flux became zero is identified as the adiabatic flame burning velocity of the unburned gas mixture at temperature T0. A mixing panel was utilized to regulate the flow of the vaporized fuel and air at the desired equivalence ratio.

CHAPTER 3: Assessment of reduced chemical kinetic mechanism

A large set of experimental data relevant to CH_3OH combustion was collected and utilized in this study. These data encompass ignition delay times, concentration profiles in jet stirred reactors (JSRs), and laminar flame speeds, and are widely employed for validating methanol combustion kinetics.

Experimental data on ignition delay times were obtained from the work of Burke et al. (2016). Specifically, 10 detailed datasets were acquired from Burke et al. (2016) , covering a wide range of temperatures (900-1450 K), pressures (2.0-50.0 atm), and equivalence ratios (φ=0.5-2.0). Concentration measurements of species in jet stirred reactors (JSRs) were sourced from two literature references. Seven datasets from Burke et al. (2016) covered temperatures ranging from 800-1200 K, pressures from 1-20 atm, and equivalence ratios from φ=0.2-2.0. Additionally, six datasets from Wang et al. (2022) included temperatures of 550-950 K, pressures of 10-100 atm, and equivalence ratios of φ=0.1-9.0. Experimental data on laminar flame speeds were obtained from two literature references. Two datasets from Zhang et al. (2008) covered an inlet temperature of 373 K, pressures from 1-5 bar, and equivalence ratios of φ=0.7-1.4. Furthermore, one dataset from Beeckmann et al. (2014) included an inlet temperature of 373 K, a pressure of 10 bar, and equivalence ratios of φ=0.7-1.3.

As indicated in the previous section, one reduced-order mechanism evaluated in the present study for investigating CH_3OH combustion in sCO_2 conditions is ACR55. Computation with the Updated HP-Mech was also performed to further evaluate the results of the ACR55 mechanism. Table 2 presents the number of species and elementary reactions included in each mechanism.

Table 2. Number of species and elementary reactions included in the two mechanisms used in the present study.

Mechanism	Number of species	Number of reactions
ACR55	18	55 (**irreversible**)
Updated HP-Mech	131	899 (**reversible**)

Mechanism assessment has been carried out by comparing simulation results of the ACR55 mechanism against experiments and the results of the Updated HP-Mech mechanism. Simulations have been performed using the ANSYS CHEMKIN-PRO software. Representative computational results for ignition delay times are presented in Figure 1 (φ = 0.5 and φ = 1.0, for pressure of 50 atm) and in Figure 2 (φ = 1.0, for p = 31 atm). Computed representative speciation profiles in JSRs are shown in Figures 3 and 4 (p = 20.0 atm, φ = 0.2), Figures 5 and 6 (p = 20.0 atm, φ = 0.5), and Figures 7 and 8 (φ=0.1 and φ=1.0 for pressure p = 100.0 atm). Finally, computed laminar flame speeds of methanol-air mixtures at p = 1.0, 5.0, and 10.0 atm and unburned mixture temperature T_{un} = 373 K are shown in Figures 9 and 10.

The mechanism studied during the assessment process is presented in Table 3 (Pichler, & Nilsson 2018).

Table 3. Studied Reduced Order Chemical Kinetic Mechanism

Reduced Order Chemical Kinetic Mechanism	Number of chemical compounds	Number of chemical reactions
Nilsson	18	55

The reduced order mechanism was assessed in relation to a detailed mechanism and using experimental data on concentration profiles of the important combustion compounds of CH_3OH as a function of temperature, ignition delay time and laminar premixing flame velocity.

Additionally, the detailed mechanism that was used for the further assessment of the reduced mechanism is presented in Table 4 (Wang et al. 2022).

Table 4. Detailed Chemical Kinetic Mechanism

Detailed Chemical Kinetic Mechanism	Number of chemical compounds	Number of chemical reactions
Hp-Mech	131	899

The simulations of the two mechanisms were carried out through the CHEMKIN code. The variables of the solvers used are those suggested by the manufacturer's manual. Tables 4,5, and 6 present the solvers used for each simulation category.

The numerical parameters of the solver for calculating the concentration profile are as follows:

Table 5. Values of numerical solver parameters for calculating the concentration profile as a function of temperature

BASIC SOLVER	
ABSOLUTE TOLERANCE	1.0E-20
RELATIVE TOLENRANCE	1.0E-8
SENSITIVITY ABSOLUTE TOLERANCE	0.0001
SENSITIVITY RELATIVE TOLERANCE	0.0001

The numerical parameters of the solver for calculating the ignition delay time are as follows:

Table 6. Numerical solver parameter values for calculating ignition delay time

BASIC SOLVER	
ABSOLUTE TOLERANCE	1.0E-20
RELATIVE TOLENRANCE	1.0E-8
SENSITIVITY ABSOLUTE TOLERANCE	0.0001
SENSITIVITY RELATIVE TOLERANCE	0.0001

The numerical parameters of the solver for calculating the laminar premixing flame speed are as follows:

Table 7. Values of the numerical parameters of the solver for the calculation of laminar premixing flame

BASIC SOLVER	
ABSOLUTE TOLERANCE	1.0E-9
RELATIVE TOLENRANCE	0.0001
ABSOLUTE TOLERANCE FOR PSEDO TIMESTEPPING	1.0E-9
RELATIVE TOLERANCE FOR PSEDO TIMESTEPPING	0.0001
ADVANCED SOLVER	

PSEUDO TIME STEPS (FIXED TEMPRATURE)	
NUMBER OF TIME STEPS	100
INITIAL SIZE OF TIME STEP	1.0E-6 sec
PSEUDO TIME STEPS (ENERGY EQUATION)	
NUMBER OF TIME STEPS	100
INITIAL SIZE OF TIME STEP	1.0E-6 sec
MINIMUN PSEUDO TIME STEP	1.0E-10 sec
MAXIMUM PSEUDO TIME STEP	0.0001 sec
NUMBER TIME STEPS BEFORE INCREASING	25
TIME STEP DECREMENT FACTOR	2.0
TIME STEP INCREMENT FACTOR	2.0
NUMBER OF TRANSIENT ITERATIONS BEFORE UPDATING JACOBIAN	20
NUMBER OF INITIAL PSEUDO TIMESTEPS	0
NUMBER OF ITERATIONS BEFORE UPDATING JACOBIAN	20
MINIMUM BOUNDS ON SPECIES FACTIONS	-0.001
POSITIVE VALUE TO RESET SPECIES FRACTIONS	1.0E-12

The pressure, temperature and air fuel equivalence ratio conditions for which the simulations of each category were carried out are presented in the following tables.

Table 8 shows the conditions used in the study for the PSR simulations.

Table 8. Conditions of PSR simulations

Pressure (atm)	Temperature Range (K)	Fuel-Air Equivalence Ratio φ
1	650-1250	1
10	650-1250	0.2 , 2
10	700-1250	1
20	650-1250	0.2 , 0.5 , 1
10	500-1000	0.1 , 1 , 9
100	500-1000	0.1 , 1 , 9

Table 9 shows the conditions used in the study to calculate the ignition delay time.

Table 9. Conditions of ignition delay simulations

Pressure (atm)	Temperature Range (K)	Fuel-Air Equivalence Ratio φ
20	950-1300	0.5
0.5	950-1300	49.6
20	950-1250	1
31	850-1175	1
51	850-1250	2
10	950-1325	1
49	950-1350	1
10	1050-1475	1
50	950-1250	1

Table 10 shows the conditions used in the study to calculate the laminar premixing flame speed.

Table 10. Conditions of laminar premixing flame speed simulations

Pressure (bar)	**Inlet Temperature (K)**	**Fuel-Air Equivalence Ratio φ**
1	373	0.7 , 0.8 ,0.9 , 1 , 1.1 , 1.2 , 1.3 , 1.4
5	373	0.7 , 0.8 ,0.9 , 1 , 1.1 , 1.2 , 1.3 , 1.4
10	373	0.71 , 0.82 , 0.92 , 1.02 , 1.12 , 1.22 , 1.33
Pressure (atm)	**Inlet Temperature (K)**	**Fuel-Air Equivalence Ratio φ**
1	**298**	0.7 , 0.8 ,0.9 , 1 , 1.1 , 1.5
1	**423**	0.8 ,0.9 , 1 , 1.1 , 1.2 , 1.3

The evaluation process resulted in the following indicative diagrams. The simulation results are presented in the diagrams with consecutive lines, and the experimental data are presented with points. For reasons of briefness, the mechanisms are presented in the legends within the diagrams with the symbolic names shown in Table 10, rather than the names given by their creators.

Table 11. Symbolic names of the two chemical kinetics mechanisms

Original mechanism name	**Mechanism name in diagramms**
Updated Hp-Mech	Hp-Mech
ACR55	Nilsson

3.1 Ignition delay time

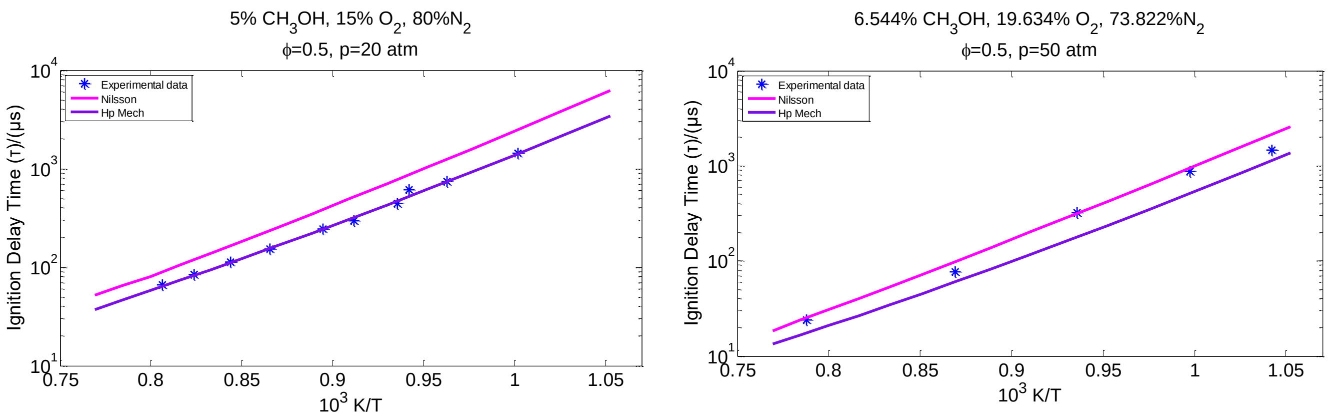

Figure 15. Ignition delay time profiles versus initial temperature for homogeneous CH_3OH-air mixtures of (a) φ = 0.5, P = 20 atm, mixture composition per volume: 20.0% CH_3OH, 15.0% O_2, 80.0% N_2 (Mixture 1); and (b) φ = 0.5, P = 50 atm, mixture composition per volume: 6.544% CH_3OH, 19.634% O_2, 73.822% N_2 (Mixture 2). Experimental data from Burke et al. (2016).

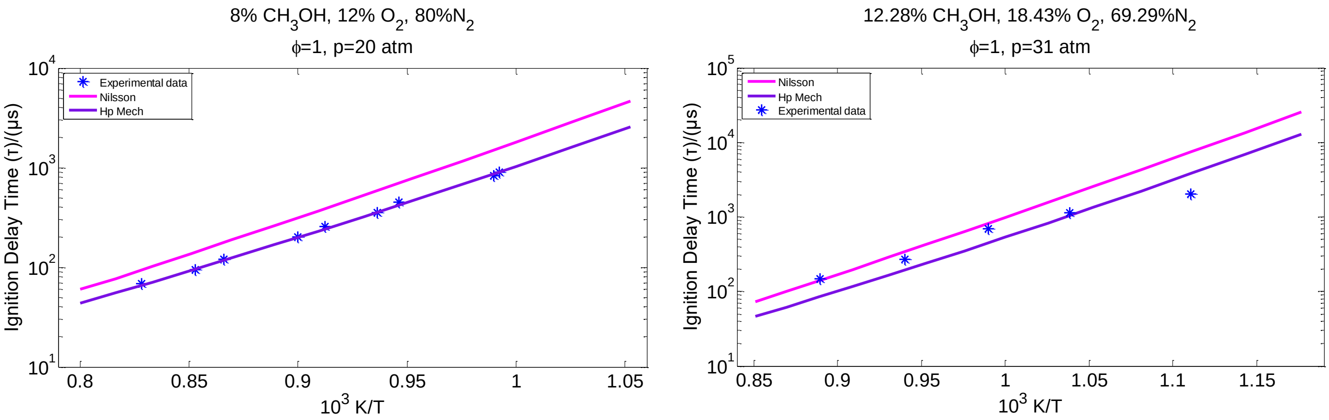

Figure 16. Ignition delay time profiles versus initial temperature for homogeneous CH_3OH-air mixtures of (a) φ = 1, P = 20 atm, mixture composition per volume: 8% CH_3OH, 12% O_2, 80.0% N_2 (Mixture 3); and (b) φ = 1, P = 31 atm, mixture composition per volume: 12.28% CH_3OH, 18.43% O_2, 69.29% N_2 (Mixture 4). Experimental data from Burke et al. (2016).

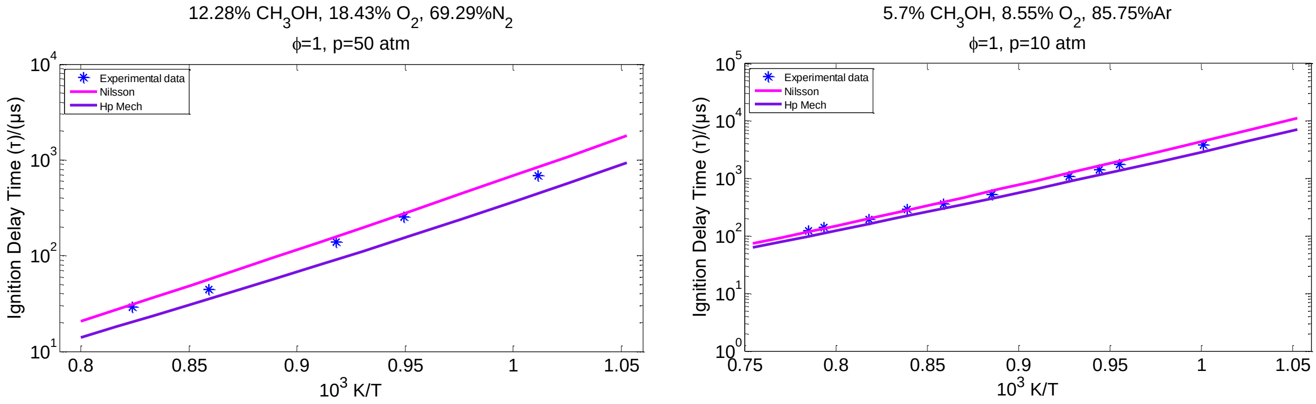

Figure 17. Ignition delay time profiles versus initial temperature for homogeneous CH_3OH-air mixtures of (a) φ = 1, P = 50 atm, mixture composition per volume: 12.28% CH_3OH, 18.43% O_2, 69.29% N_2 (Mixture 5); and (b) φ = 1, P = 10 atm, mixture composition per volume: 5.7% CH_3OH, 8.55% O_2, 85.75% N_2 (Mixture 6). Experimental data from Burke et al. (2016).

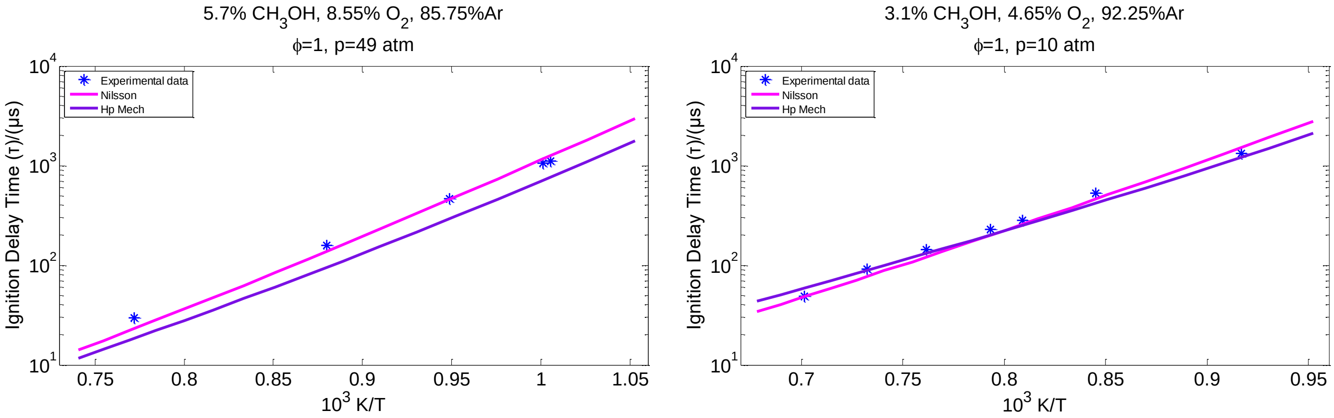

Figure 18. Ignition delay time profiles versus initial temperature for homogeneous CH_3OH-air mixtures of (a) φ = 1, P = 49 atm, mixture composition per volume: 5.7% CH_3OH, 8.55% O_2, 85.75% N_2 (Mixture 7); and (b) φ = 1, P = 10 atm, mixture composition per volume: 3.1% CH_3OH, 4.65% O_2, 92.25% N_2 (Mixture 8). Experimental data from Burke et al. (2016).

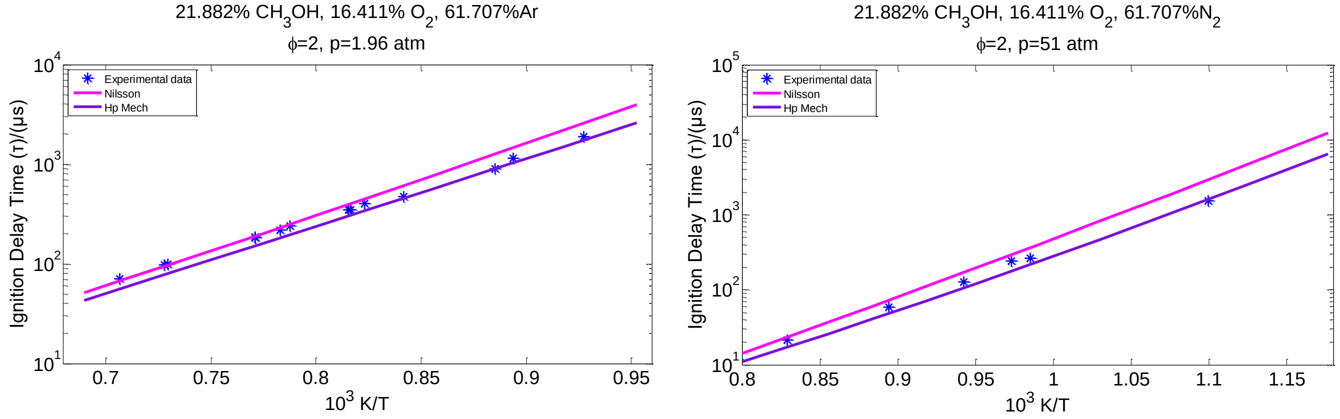

Figure 19. Ignition delay time profiles versus initial temperature for homogeneous CH_3OH-air mixtures of (a) φ = 2, P = 1.96 atm, mixture composition per volume: 21.882% CH_3OH, 16.411% O_2, 61.707% N_2 (Mixture 9); and (b) φ = 2, P = 51 atm, mixture composition per volume: 21.882% CH_3OH, 16.411% O_2, 61.707% (Mixture 10). Experimental data from Burke et al. (2016).

3.2 Concentration profiles as function of temperature

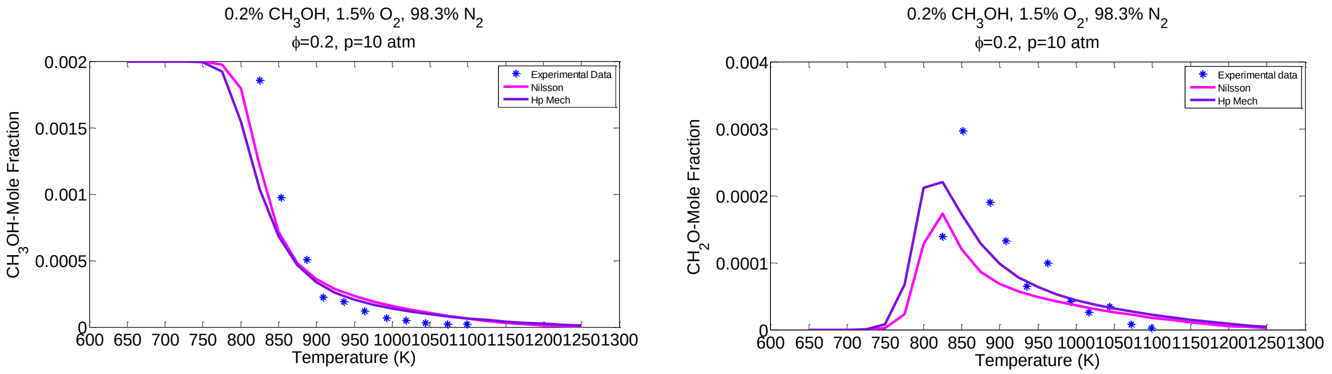

Figure 20. Mole fraction profiles versus temperature for neat CH_3OH combustion under PSR conditions at P = 10 atm, φ = 0.2, and τ_{res}=0.5 s of (a) CH_3OH; and (b) CH_2O. Mixture composition per volume: 0.2% CH_3OH, 1.5% O_2, 98.3% N_2 (Mixture 1). Experimental data from Burke et al. 2016.

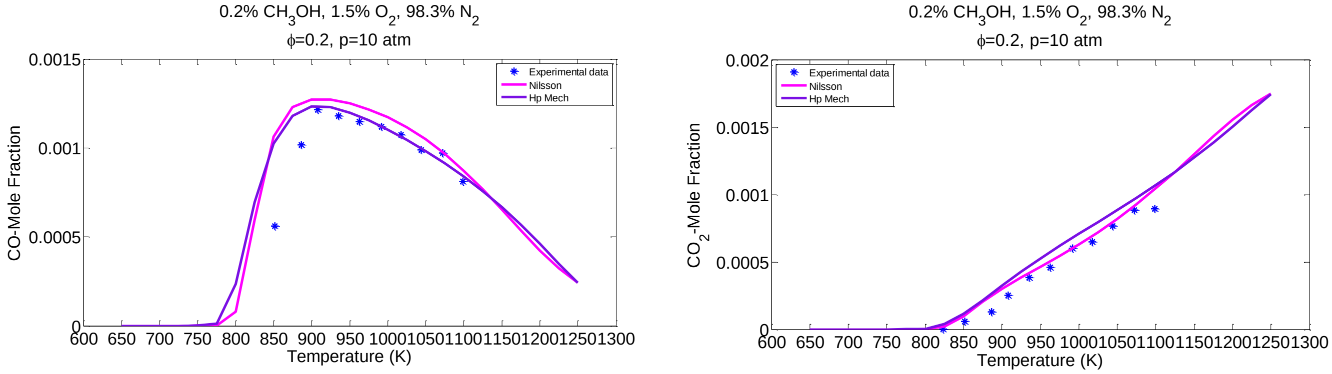

Figure 21. Mole fraction profiles versus temperature for neat CH_3OH combustion under PSR conditions at P = 10 atm, φ = 0.2, and τ_{res}=0.5 s of (a) CO; and (b) CO_2. Mixture composition per volume: 0.2% CH_3OH, 1.5% O_2, 98.3% N_2 (Mixture 1). Experimental data from Burke et al. 2016.

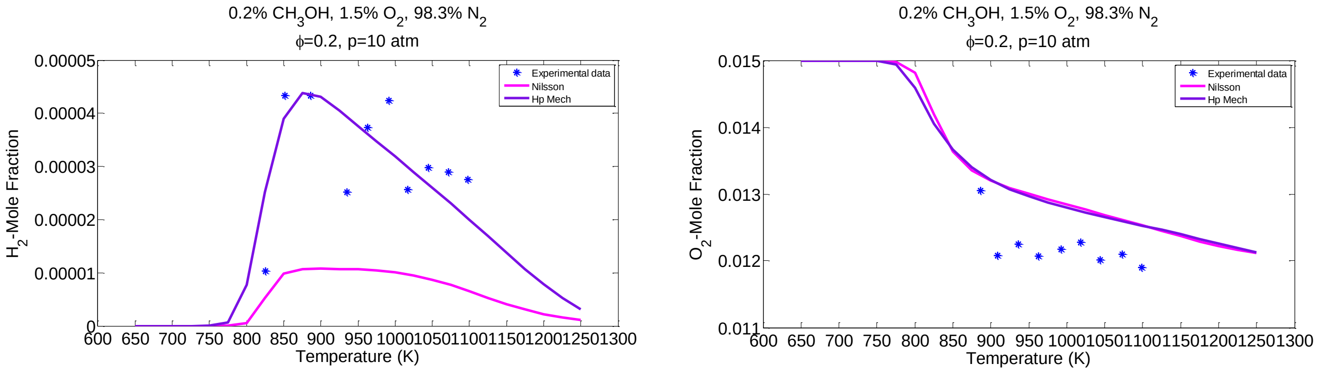

Figure 22. Mole fraction profiles versus temperature for neat CH_3OH combustion under PSR conditions at P = 10 atm, φ = 0.2, and τ_{res}=0.5 s of (a) H_2; and (b) O_2. Mixture composition per volume: 0.2% CH_3OH, 1.5% O_2, 98.3% N_2 (Mixture 1). Experimental data from Burke et al. 2016.

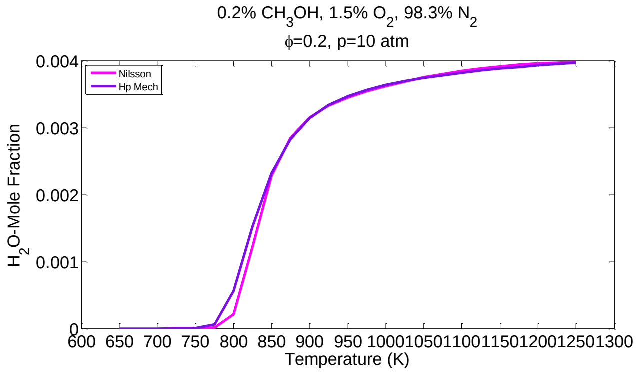

Figure 23. Mole fraction profiles versus temperature for neat CH_3OH combustion under PSR conditions at P = 10 atm, φ = 0.2, and τ_{res}=0.5 s of H_2O. Mixture composition per volume: 0.2% CH_3OH, 1.5% O_2, 98.3% N_2 (Mixture 1). Experimental data from Burke et al. 2016.

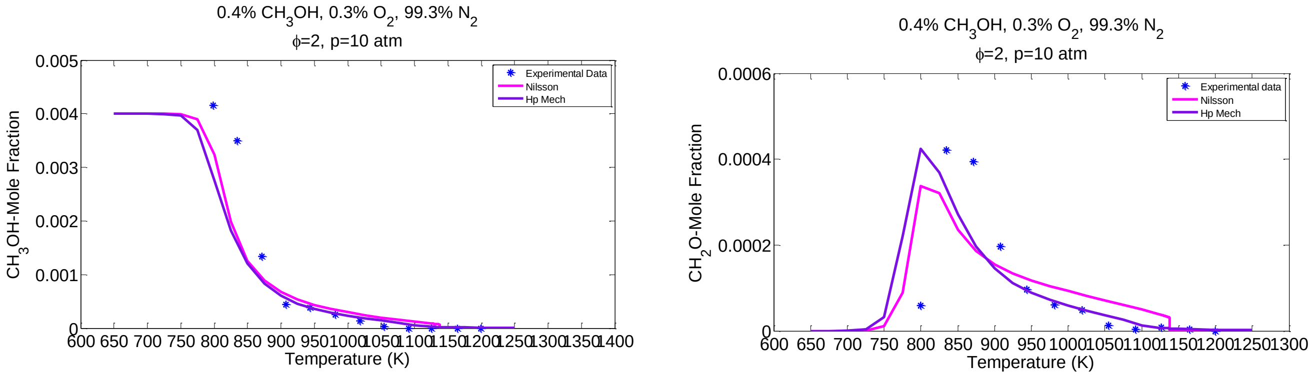

Figure 24. Mole fraction profiles versus temperature for neat CH_3OH combustion under PSR conditions at P = 10 atm, φ = 2, and τ_{res}=0.5 s of (a) CH_3OH; and (b) CH_2O. Mixture composition per volume: 0.4% CH_3OH, 0.3% O_2, 99.3% N_2 (Mixture 2). Experimental data from Burke et al. 2016.

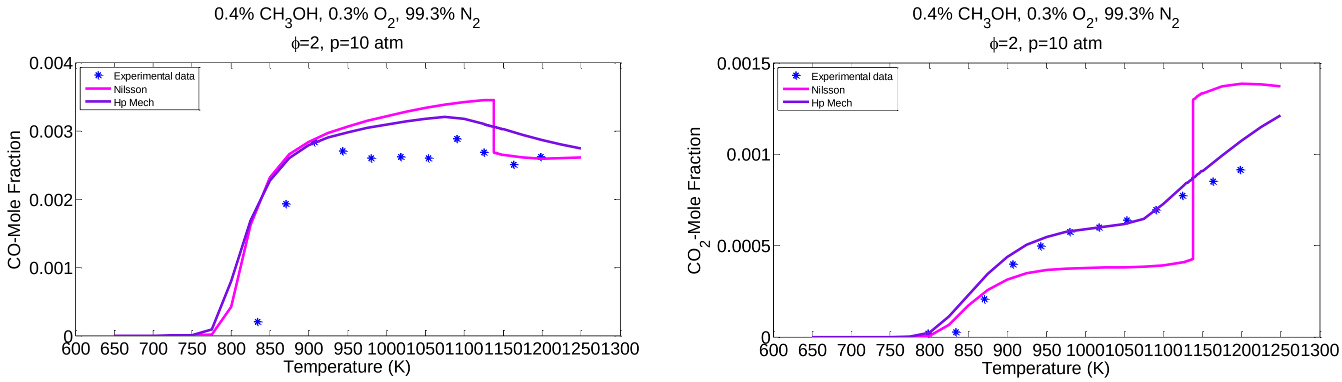

Figure 25. Mole fraction profiles versus temperature for neat CH_3OH combustion under PSR conditions at P = 10 atm, φ = 2, and τ_{res}=0.5 s of (a) CO; and (b) CO_2. Mixture composition per volume: 0.4% CH_3OH, 0.3% O_2, 99.3% N_2 (Mixture 2). Experimental data from Burke et al. 2016.

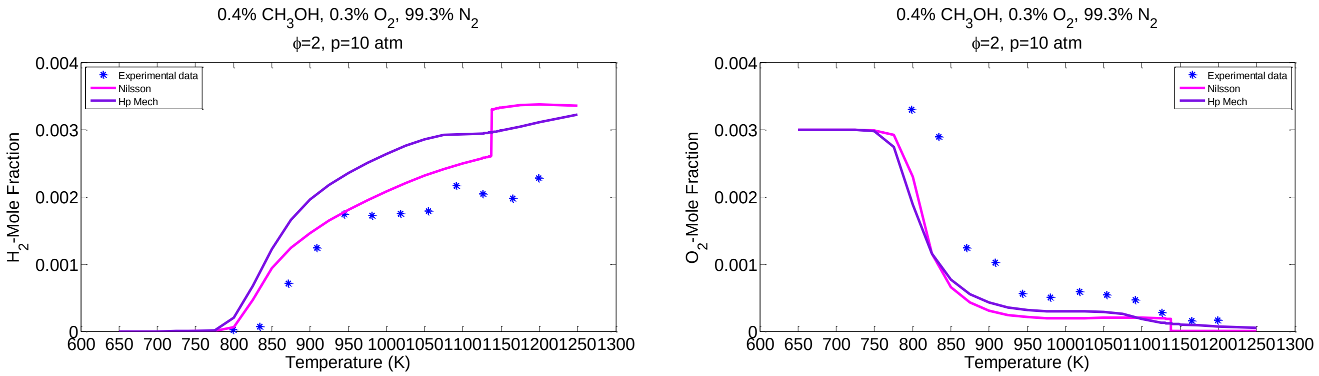

Figure 26. Mole fraction profiles versus temperature for neat CH_3OH combustion under PSR conditions at P = 10 atm, φ = 2, and τ_{res}=0.5 s of (a) H_2; and (b) O_2. Mixture composition per volume: 0.4% CH_3OH, 0.3% O_2, 99.3% N_2 (Mixture 2). Experimental data from Burke et al. 2016.

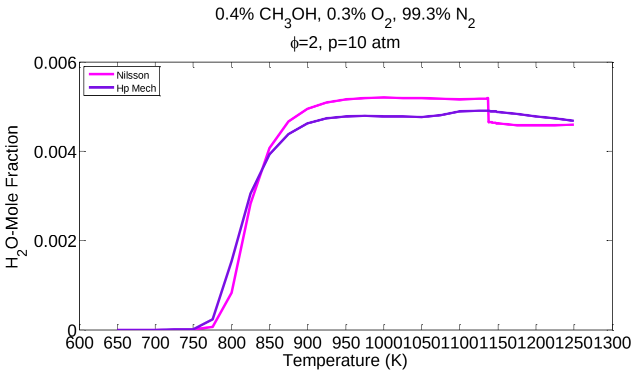

Figure 27. Mole fraction profiles versus temperature for neat CH_3OH combustion under PSR conditions at P = 10 atm, φ = 2, and τ_{res}=0.5 s of H_2O. Mixture composition per volume: 0.4% CH_3OH, 0.3% O_2, 99.3% N_2 (Mixture 2). Experimental data from Burke et al. 2016.

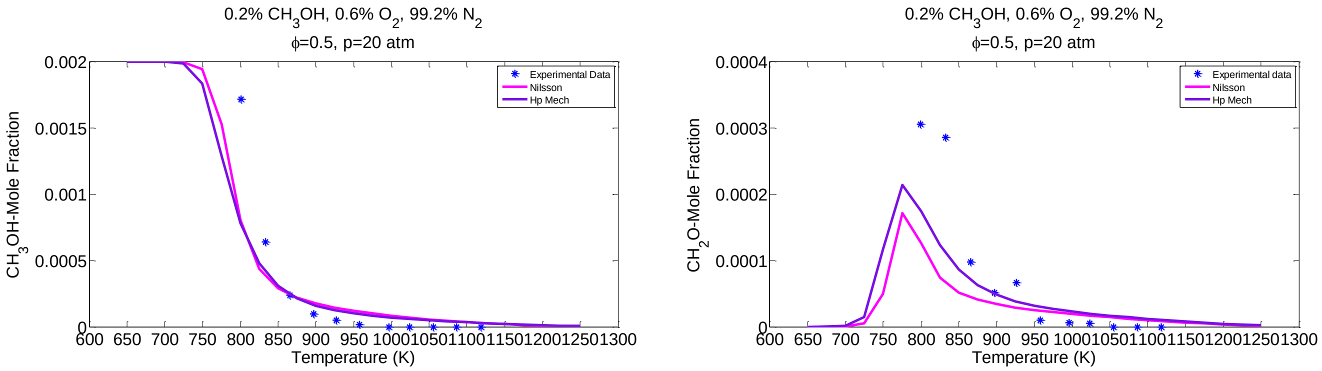

Figure 28. Mole fraction profiles versus temperature for neat CH_3OH combustion under PSR conditions at P = 20 atm, φ = 0.5, and τ_{res}=1.0 s of (a) CH_3OH; and (b) CH_2O. Mixture composition per volume: 0.2% CH_3OH, 0.6% O_2, 99.2% N_2 (Mixture 3). Experimental data from Burke et al. 2016.

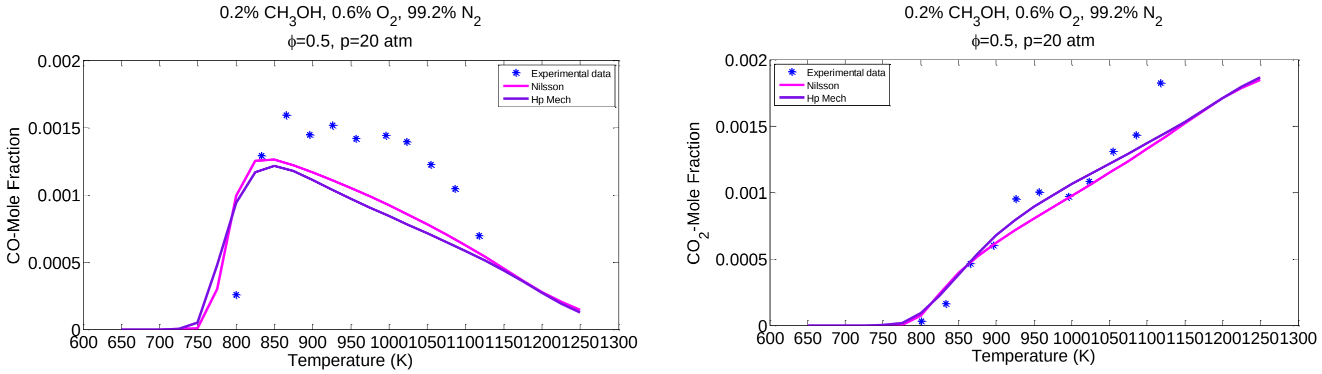

Figure 29. Mole fraction profiles versus temperature for neat CH_3OH combustion under PSR conditions at P = 20 atm, φ = 0.5, and τ_{res}=1 s of (a) CO; and (b) CO_2. Mixture composition per volume: 0.2% CH_3OH, 0.6% O_2, 99.2% N_2 (Mixture 3). Experimental data from Burke et al. 2016.

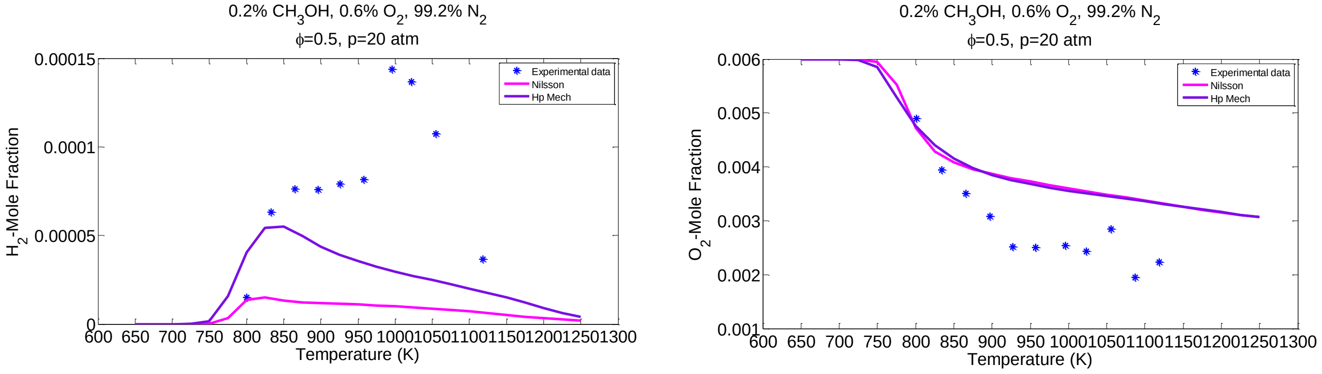

Figure 30. Mole fraction profiles versus temperature for neat CH_3OH combustion under PSR conditions at P = 20 atm, φ = 0.5, and τ_{res}=1 s of (a) H_2; and (b) O_2. Mixture composition per volume: 0.2% CH_3OH, 0.6% O_2, 99.2% N_2 (Mixture 3). Experimental data from Burke et al. 2016.

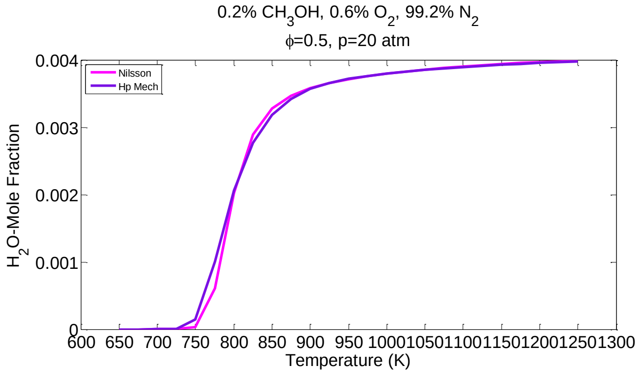

Figure 31. Mole fraction profiles versus temperature for neat CH_3OH combustion under PSR conditions at P = 20 atm, φ = 0.5, and τ_{res}=1 s of H_2O. Mixture composition per volume: 0.2% CH_3OH, 0.6% O_2, 99.2% N_2 (Mixture 3). Experimental data from Burke et al. 2016.

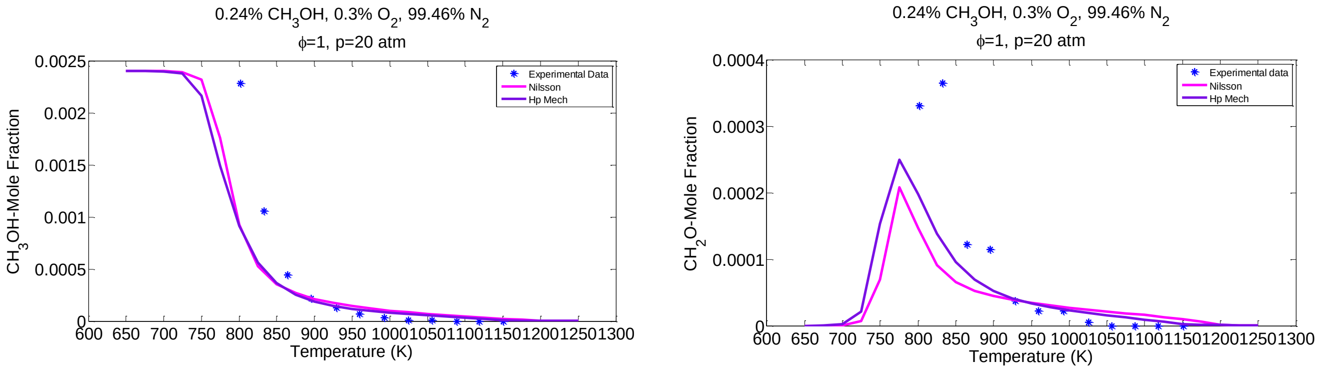

Figure 32. Mole fraction profiles versus temperature for neat CH_3OH combustion under PSR conditions at P = 20 atm, φ = 1, and τ_{res}=1.0 s of (a) CH_3OH; and (b) CH_2O. Mixture composition per volume: 0.24% CH_3OH, 0.3% O_2, 99.46% N_2 (Mixture 4). Experimental data from Burke et al. 2016.

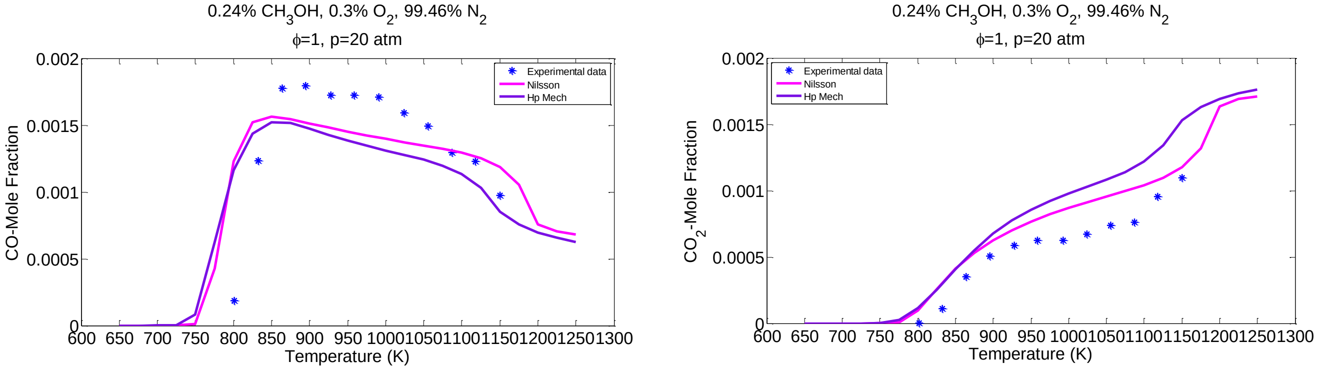

Figure 33. Mole fraction profiles versus temperature for neat CH_3OH combustion under PSR conditions at P = 20 atm, φ = 1, and τ_{res}=1 s of (a) CO; and (b) CO_2. Mixture composition per volume: 0.24% CH_3OH, 0.3% O_2, 99.46% N_2 (Mixture 4). Experimental data from Burke et al. 2016.

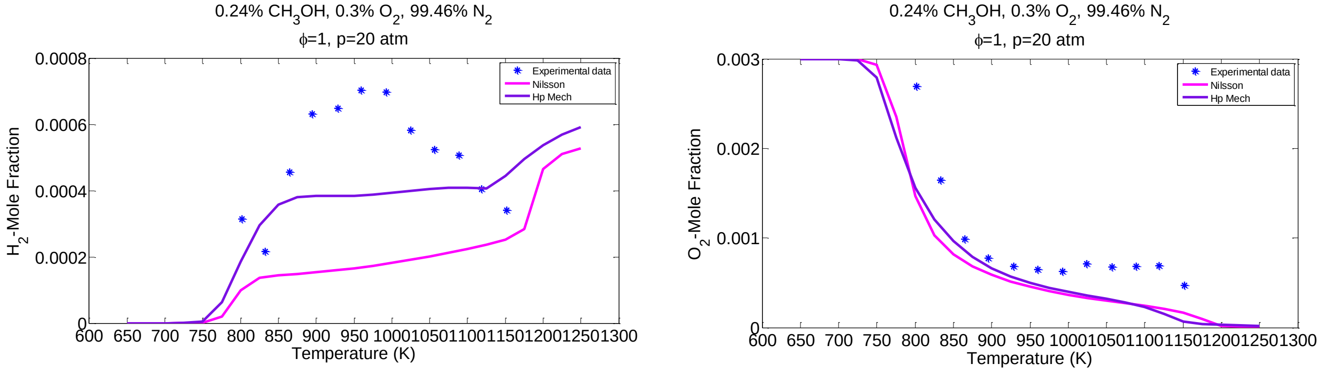

Figure 34. Mole fraction profiles versus temperature for neat CH_3OH combustion under PSR conditions at P = 20 atm, φ = 1, and τ_{res}=1 s of (a) H_2; and (b) O_2. Mixture composition per volume: 0.24% CH_3OH, 0.3% O_2, 99.46% N_2 (Mixture 4). Experimental data from Burke et al. 2016.

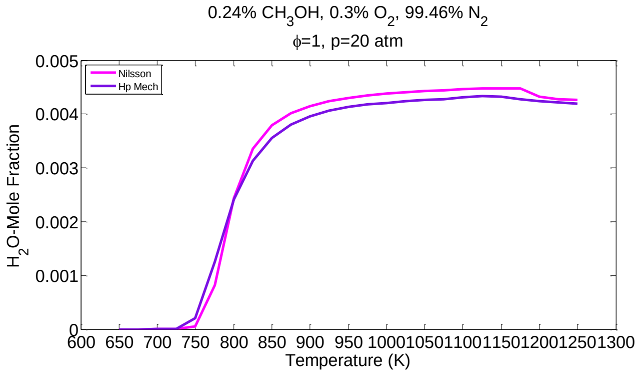

Figure 35. Mole fraction profiles versus temperature for neat CH_3OH combustion under PSR conditions at P = 20 atm, φ = 1, and τ_{res}=1 s of H_2O. Mixture composition per volume: 0.24% CH_3OH, 0.3% O_2, 99.46% N_2 (Mixture 4). Experimental data from Burke et al. 2016.

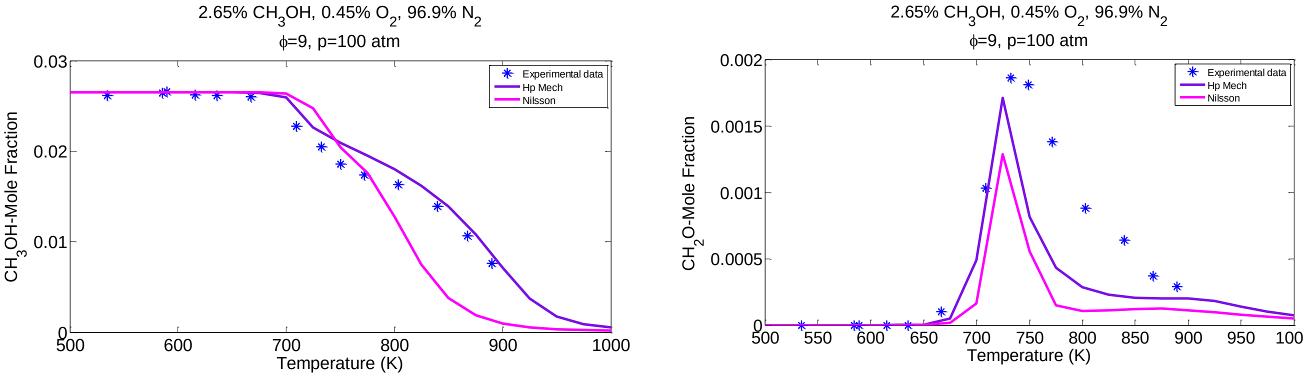

Figure 36. Mole fraction profiles versus temperature for neat CH_3OH combustion under PSR conditions at P = 100 atm, φ = 9, and τ_{res}=0.43 s of (a) CH_3OH; and (b) CH_2O. Mixture composition per volume: 2.65% CH_3OH, 0.45% O_2, 96.9% N_2 (Mixture 5). Experimental data from Wang et al. (2022).

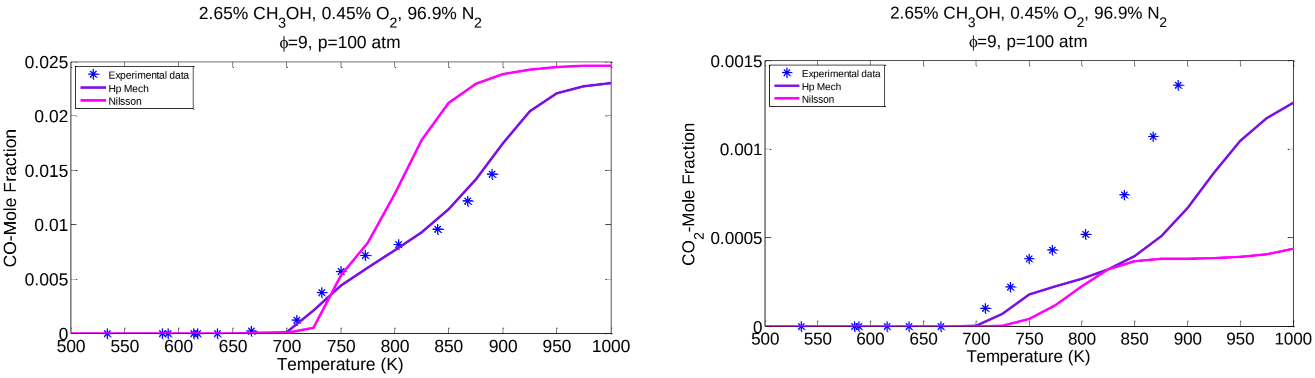

Figure 37. Mole fraction profiles versus temperature for neat CH_3OH combustion under PSR conditions at P = 100 atm, φ = 9, and τ_{res}=0.43 s of (a) CO; and (b) CO_2. Mixture composition per volume: 2.65% CH_3OH, 0.45% O_2, 96.9% N_2 (Mixture 5). Experimental data from Wang et al. (2022).

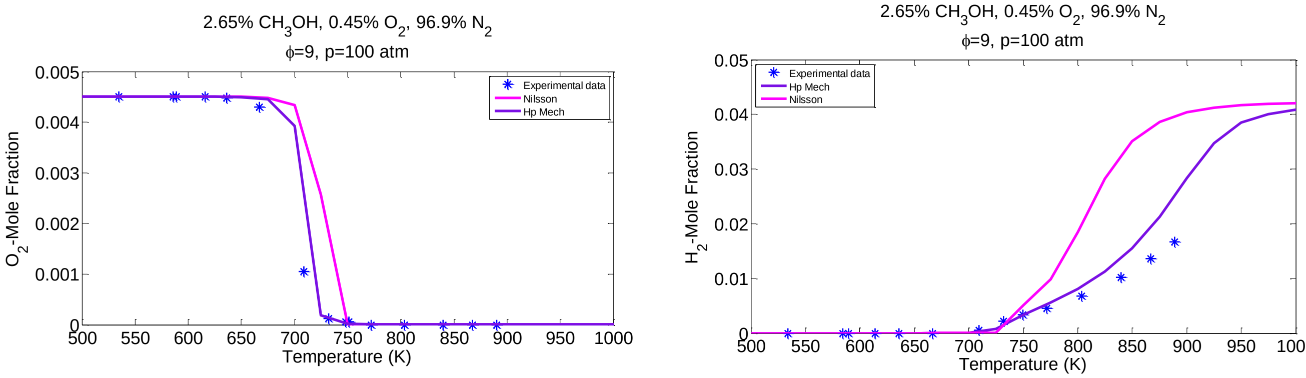

Figure 38. Mole fraction profiles versus temperature for neat CH_3OH combustion under PSR conditions at P = 100 atm, φ = 9, and τ_{res}=0.43 s of (a) H_2; and (b) O_2. Mixture composition per volume: 2.65% CH_3OH, 0.45% O_2, 96.9% N_2 (Mixture 5). Experimental data from Wang et al. (2022).

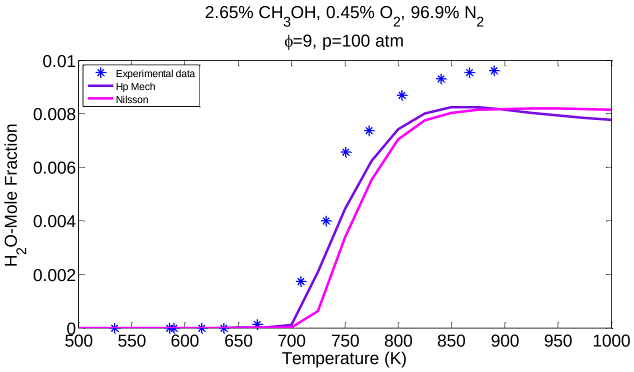

Figure 39. Mole fraction profiles versus temperature for neat CH_3OH combustion under PSR conditions at P = 100 atm, φ = 9, and τ_{res}=0.43 s of H_2O. Mixture composition per volume: 2.65% CH_3OH, 0.45% O_2, 96.9% N_2 (Mixture 5). Experimental data from Wang et al. (2022).

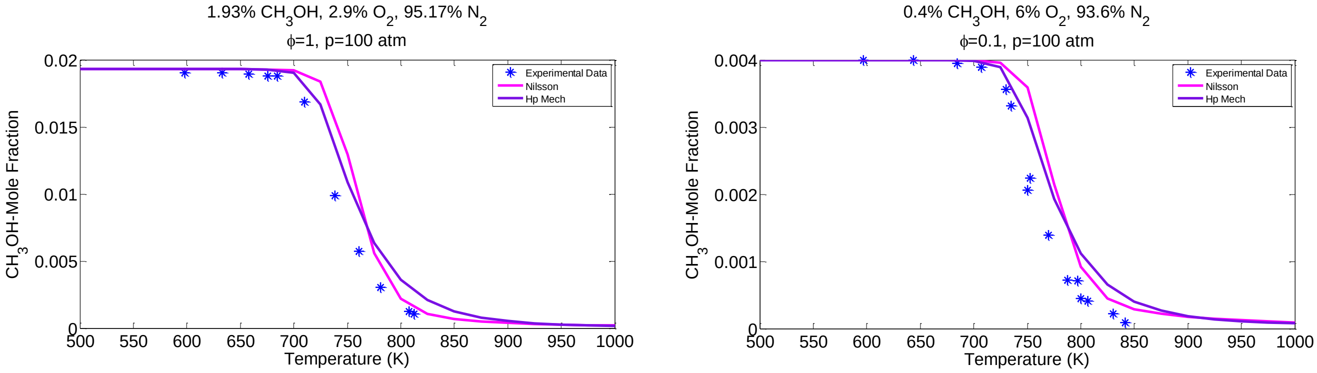

Figure 40. Mole fraction profiles of CH_3OH versus temperature for neat CH_3OH combustion under PSR conditions at (a) P = 100 atm, φ = 1, and τ_{res}=0.43 s, mixture composition per volume: 1.93% CH_3OH, 2.9% O_2, 95.17% N_2 (Mixture 6); and (b) P = 100 atm, φ = 0.1, and τ_{res}=0.43 s, mixture composition per volume: 0.4% CH_3OH, 6% O_2, 93.6% N_2 (Mixture 7). Experimental data from Wang et al. (2022).

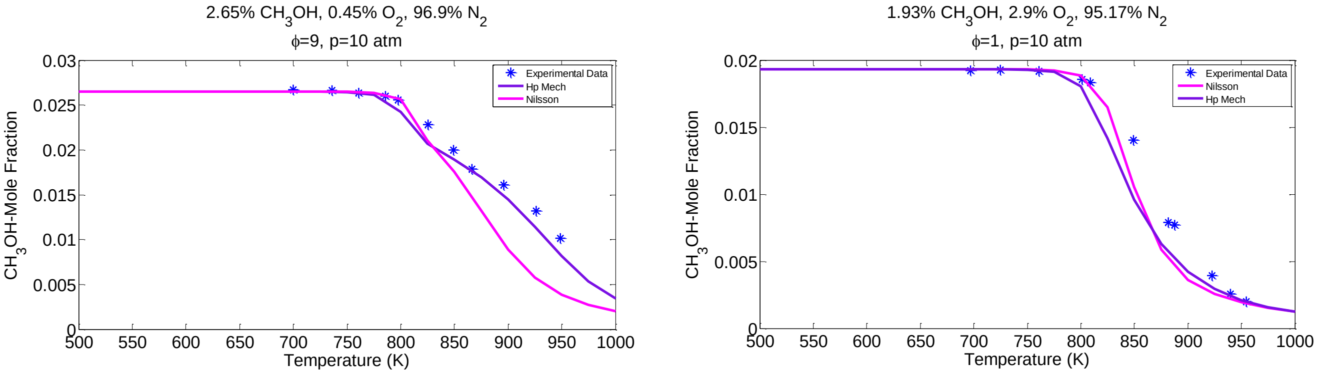

Figure 41. Mole fraction profiles of CH_3OH versus temperature for neat CH_3OH combustion under PSR conditions at (a) P = 10 atm, φ = 9, and τ_{res}=0.43 s, mixture composition per volume: 0.4% CH_3OH, 6% O_2, 93.6% N_2 (Mixture 8); and (b) P = 10 atm, φ = 1, and τ_{res}=0.43 s, mixture composition per volume: 1.93% CH_3OH, 2.9% O_2, 95.17% N_2 (Mixture 9). Experimental data from Wang et al. (2022).

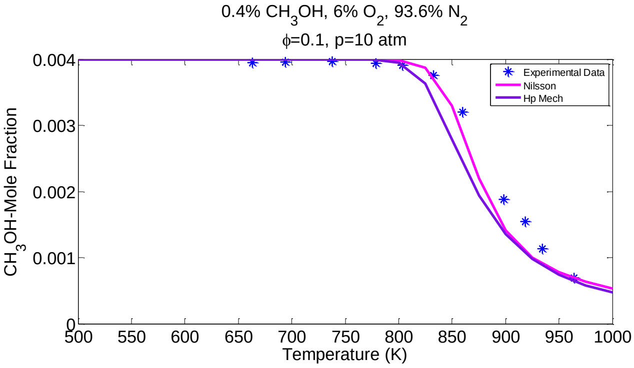

Figure 42. Mole fraction profile of CH_3OH versus temperature for neat CH_3OH combustion under PSR conditions at P = 10 atm, φ = 0.1, and τ_{res}=0.43 s. Mixture composition per volume: 2.65% CH_3OH, 0.45% O_2, 96.9% N_2 (Mixture 10). Experimental data from Wang et al. (2022).

3.3 Laminar premix flame speed

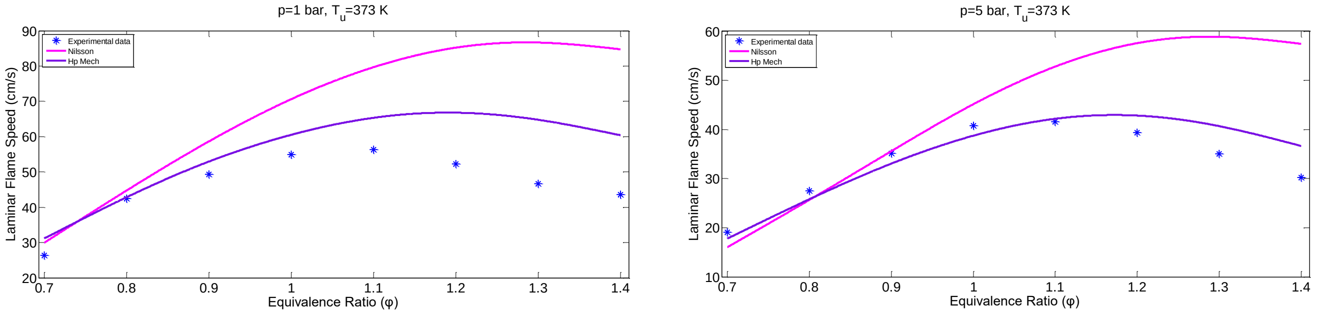

Figure 43. Laminar flame speed versus equivalence ratio for neat CH_3OH combustion, at (a) P = 1.0 bar and T_{un} = 373 K (Mixture 1), (b) P = 5.0 bar and T_{un} = 373 K (Mixture 2). Experimental data from Wang et al. (2022).

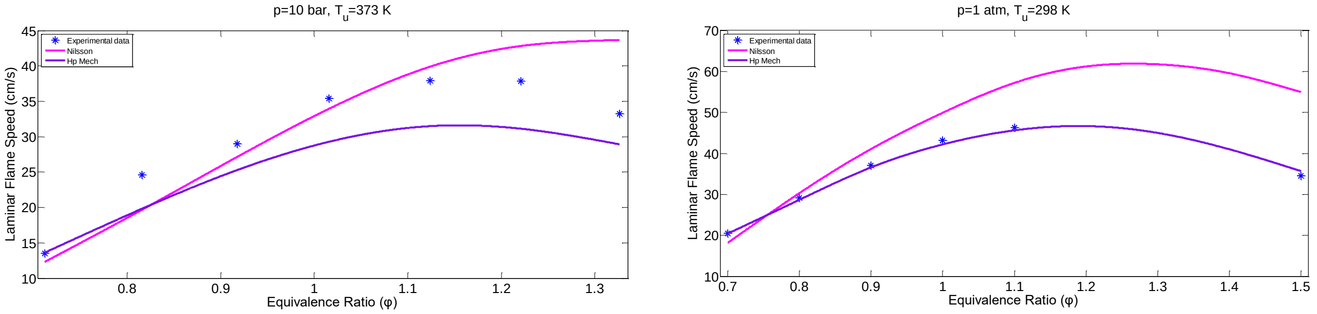

Figure 44. Laminar flame speed versus equivalence ratio for neat CH_3OH combustion, at (a) P = 10 bar and T_{un} = 373 K (Mixture 3), (b) P = 1.0 atm and T_{un} = 298 K (Mixture 4). Experimental data from Wang et al. (2022).

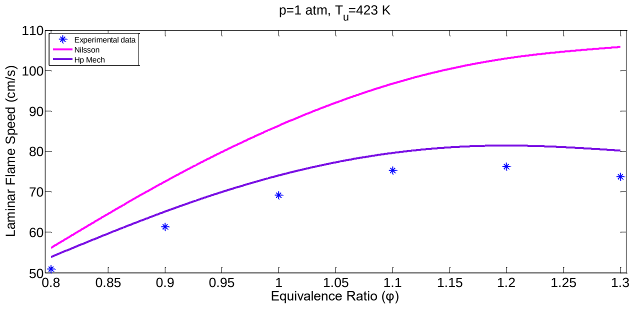

Figure 45. Laminar flame speed versus equivalence ratio for neat CH_3OH combustion, at P = 1.0 atm and T_{un} = 423 K (Mixture 3). Experimental data from Wang et al. (2022).

3.4 Relative Errors

Careful inspection of the results presented in Figures 1-10 indicates that the ACR55 mechanism accurately predicts ignition time delays for all operational conditions and stoichiometry considered. Additionally, the results of the ACR55 mechanism compare very well to JSR experimental data and are consistent with the respective computational results of the Updated HP-Mech mechanism. The only region where the ACR55 performs less satisfactorily is for the rich mixture (φ=9.0) conditions, at pressure p=100 atm, and temperatures between T = 800-900 K (see Figure 8). In addition, small-scale discrepancies are observed between experiments and the computational results of both the ACR55 mechanism and the Updated HP-Mech mechanism for lean mixtures (φ=0.2 and φ=0.5) conditions at p=20 atm and temperatures between T=900 – 1100 K (see Figures 3b, 5b) for carbon monoxide (CO) production. Finally, the ACR55 mechanism accurately reproduces laminar flame speeds for lean mixtures (φ=0.7-1.0) for pressures p=1.0, 5.0 bar, and performs less satisfactorily in the rich region (φ=1.0-1.4 – Figures 9a, 9b). This performance is mitigated for the case of p=10 atm (see Figure 10), in which the results of the ACR55 mechanism in the rich region reproduce the experiments more accurately. It is noted that for this case (p=10 atm), the results of the lean and stoichiometric regions are characterized by very good agreement with experimental measurements.

Furthermore, to quantify the accuracy of the obtained computational results of the ACR55 mechanism in comparison to the experimental data, an average relative error for each dataset is used in the present study. The equation for the average relative error is defined as follows:

$$Relative\ Error = \left|\left(\frac{experiment - numerical}{experiment}\right)\right| \cdot 100,\quad Average\ \ Relative\ Error = \frac{\sum_{i=1}^{n} Relative\ Error}{n_{exper.meas.}}$$

Table 12 shows the values of the average relative error for the ACR55 mechanism, as well as for the Updated HP-Mech mechanism. These values confirm the validity of the ACR55 mechanism's performance. It is noted that in some cases, the ACR55 mechanism's performance is better than that of the Updated HP-Mech mechanism, which is remarkable considering that the ACR55 mechanism includes only 18 species and 55 irreversible reactions.

In conclusion, for all three canonical problems, the ACR55 mechanism consistently reproduces the experimental data across the entire range of parameters considered. Thus, the ACR55 mechanism is adopted for further investigation of ignition and combustion at PSR conditions of CH_3OH in an sCO_2 environment

Table 12. Average Relative Error of Updated HP Mech. and ACR55 mechanisms for all three prototype problems (i.e. (i) Ignition of homogeneous mixture, (ii) Combustion in PSR conditions, and (iii) Premixed laminar burning velocities) considered here.

#	Data Set	Average Relative Error (%) (Updated HP Mech.)	Average Relative Error (%) (ACR55)
1	IDT, p=50 atm, φ=0.5	10.2	2.1
2	IDT, p=31 atm, φ=1.0	5.8	4.6
3	IDT, p=50 atm, φ=1.0	2.9	6.4
4	PSR, p=20 atm, φ=0.2, CH_3OH	54.2	58.0
5	PSR, p=20 atm, φ=0.2, CO	25.7	19.7
6	PSR, p=20 atm, φ=0.2, CO_2	18.9	16.3
7	PSR, p=20 atm, φ=0.5, CH_3OH	28.6	32.3
8	PSR, p=20 atm, φ=0.5, CO	31.9	28.3
9	PSR, p=20 atm, φ=0.5, CO_2	8.5	11.3

10	PSR, p=100 atm, φ=0.1, CH_3OH	39.2	31.0
11	PSR, p=100 atm, φ=1.0, CH_3OH	27.7	21.0
12	PSR, p=100 atm, φ=9.0, CH_3OH	6.6	19.4
13	LFS, p=1.0 bar, T_{un} = 373 K	19.7	43.9
14	LFS, p=5.0 bar, T_{un} = 373 K	9.0	33.2
15	LFS, p=10.0 bar, T_{un} = 373 K	13.9	12.9

3.4.1 IDT SIMULATIONS RELATIVE ERRORS

Table 13. Relative error of HP Mech and Nilsson ignition delay time simulation results relative to the experimental data for homogeneous CH_3OH-air mixtures of φ = 0.5, P = 20 atm, (Mixture 1).

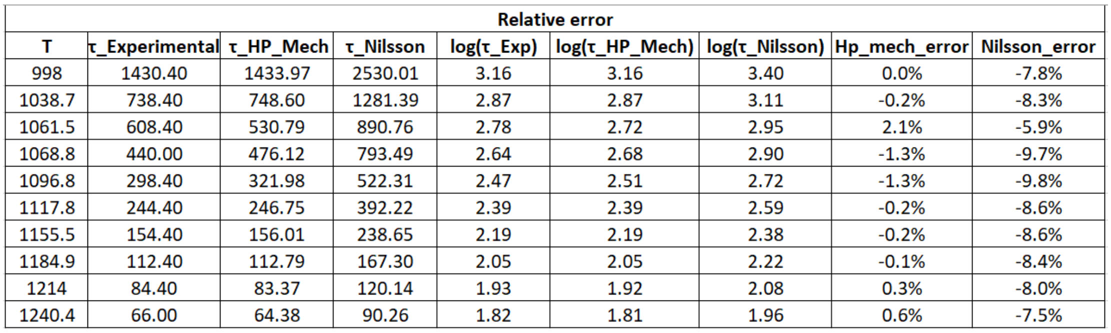

Relative error								
T	τ_Experimental	τ_HP_Mech	τ_Nilsson	log(τ_Exp)	log(τ_HP_Mech)	log(τ_Nilsson)	Hp_mech_error	Nilsson_error
998	1430.40	1433.97	2530.01	3.16	3.16	3.40	0.0%	-7.8%
1038.7	738.40	748.60	1281.39	2.87	2.87	3.11	-0.2%	-8.3%
1061.5	608.40	530.79	890.76	2.78	2.72	2.95	2.1%	-5.9%
1068.8	440.00	476.12	793.49	2.64	2.68	2.90	-1.3%	-9.7%
1096.8	298.40	321.98	522.31	2.47	2.51	2.72	-1.3%	-9.8%
1117.8	244.40	246.75	392.22	2.39	2.39	2.59	-0.2%	-8.6%
1155.5	154.40	156.01	238.65	2.19	2.19	2.38	-0.2%	-8.6%
1184.9	112.40	112.79	167.30	2.05	2.05	2.22	-0.1%	-8.4%
1214	84.40	83.37	120.14	1.93	1.92	2.08	0.3%	-8.0%
1240.4	66.00	64.38	90.26	1.82	1.81	1.96	0.6%	-7.5%

Table 14. Relative error of HP Mech and Nilsson ignition delay time simulation results relative to the experimental data for homogeneous CH_3OH-air mixtures of φ = 0.5, P = 50 atm, (Mixture 2).

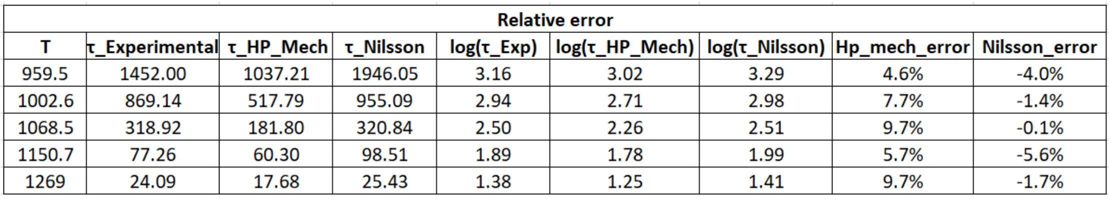

Relative error								
T	τ_Experimental	τ_HP_Mech	τ_Nilsson	log(τ_Exp)	log(τ_HP_Mech)	log(τ_Nilsson)	Hp_mech_error	Nilsson_error
959.5	1452.00	1037.21	1946.05	3.16	3.02	3.29	4.6%	-4.0%
1002.6	869.14	517.79	955.09	2.94	2.71	2.98	7.7%	-1.4%
1068.5	318.92	181.80	320.84	2.50	2.26	2.51	9.7%	-0.1%
1150.7	77.26	60.30	98.51	1.89	1.78	1.99	5.7%	-5.6%
1269	24.09	17.68	25.43	1.38	1.25	1.41	9.7%	-1.7%

Table 15. Relative error of HP Mech and Nilsson ignition delay time simulation results relative to the experimental data for homogeneous CH_3OH-air mixtures of φ = 1, P = 20 atm, (Mixture 3).

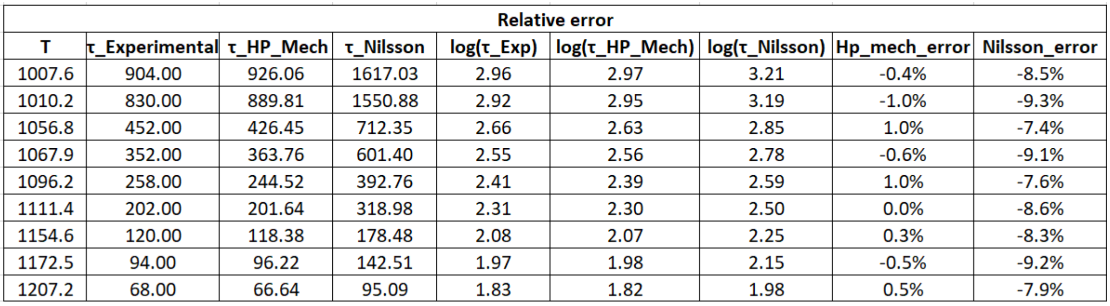

Relative error								
T	τ_Experimental	τ_HP_Mech	τ_Nilsson	log(τ_Exp)	log(τ_HP_Mech)	log(τ_Nilsson)	Hp_mech_error	Nilsson_error
1007.6	904.00	926.06	1617.03	2.96	2.97	3.21	-0.4%	-8.5%
1010.2	830.00	889.81	1550.88	2.92	2.95	3.19	-1.0%	-9.3%
1056.8	452.00	426.45	712.35	2.66	2.63	2.85	1.0%	-7.4%
1067.9	352.00	363.76	601.40	2.55	2.56	2.78	-0.6%	-9.1%
1096.2	258.00	244.52	392.76	2.41	2.39	2.59	1.0%	-7.6%
1111.4	202.00	201.64	318.98	2.31	2.30	2.50	0.0%	-8.6%
1154.6	120.00	118.38	178.48	2.08	2.07	2.25	0.3%	-8.3%
1172.5	94.00	96.22	142.51	1.97	1.98	2.15	-0.5%	-9.2%
1207.2	68.00	66.64	95.09	1.83	1.82	1.98	0.5%	-7.9%

Table 16. Relative error of HP Mech and Nilsson ignition delay time simulation results relative to the experimental data for homogeneous CH_3OH-air mixtures of φ = 1, P = 31 atm, (Mixture 4).

Relative error								
T	τ_Experimental	τ_HP_Mech	τ_Nilsson	log(τ_Exp)	log(τ_HP_Mech)	log(τ_Nilsson)	Hp_mech_error	Nilsson_error
900.58	2028.00	3810.93	7398.98	3.31	3.58	3.87	-8.3%	-17.0%
962.95	1139.00	1075.84	2037.05	3.06	3.03	3.31	0.8%	-8.3%
1010	698.15	459.88	844.68	2.84	2.66	2.93	6.4%	-2.9%
1063.89	269.00	196.81	345.68	2.43	2.29	2.54	5.6%	-4.5%
1124.23	149.42	85.13	140.64	2.17	1.93	2.15	11.2%	1.2%

Table 17. Relative error of HP Mech and Nilsson ignition delay time simulation results relative to the experimental data for homogeneous CH_3OH-air mixtures of φ = 1, P = 50 atm, (Mixture 5).

Relative error								
T	τ_Experimental	τ_HP_Mech	τ_Nilsson	log(τ_Exp)	log(τ_HP_Mech)	log(τ_Nilsson)	Hp_mech_error	Nilsson_error
988.7	683.78	458.60	865.70	2.83	2.66	2.94	6.1%	-3.6%
1053.2	253.05	154.44	278.36	2.40	2.19	2.44	8.9%	-1.7%
1089.1	138.98	92.43	161.66	2.14	1.97	2.21	8.3%	-3.1%
1164	44.26	35.40	57.41	1.65	1.55	1.76	5.9%	-6.9%
1214	29.22	20.36	31.23	1.47	1.31	1.49	10.7%	-2.0%

Table 18. Relative error of HP Mech and Nilsson ignition delay time simulation results relative to the experimental data for homogeneous CH_3OH-air mixtures of φ = 1, P = 10 atm, (Mixture 6).

Relative error								
T	τ_Experimental	τ_HP_Mech	τ_Nilsson	log(τ_Exp)	log(τ_HP_Mech)	log(τ_Nilsson)	Hp_mech_error	Nilsson_error
998.9	3867.00	2955.52	4512.06	3.59	3.47	3.65	3.3%	-1.9%
1047	1785.00	1387.28	2028.45	3.25	3.14	3.31	3.4%	-1.7%
1059	1406.00	1171.85	1695.04	3.15	3.07	3.23	2.5%	-2.6%
1078.2	1095.00	885.09	1255.02	3.04	2.95	3.10	3.0%	-1.9%
1129.5	529.40	455.41	613.25	2.72	2.66	2.79	2.4%	-2.3%
1164.3	363.71	303.65	395.51	2.56	2.48	2.60	3.1%	-1.4%
1192	290.30	223.32	283.24	2.46	2.35	2.45	4.6%	0.4%
1222.3	194.19	162.08	199.79	2.29	2.21	2.30	3.4%	-0.5%
1260	140.23	112.89	135.95	2.15	2.05	2.13	4.4%	0.6%
1273.6	124.53	99.02	118.90	2.10	2.00	2.08	4.8%	1.0%

Table 19. Relative error of HP Mech and Nilsson ignition delay time simulation results relative to the experimental data for homogeneous CH_3OH-air mixtures of φ = 1, P = 49 atm, (Mixture 7).

Relative error								
T	τ_Experimental	τ_HP_Mech	τ_Nilsson	log(τ_Exp)	log(τ_HP_Mech)	log(τ_Nilsson)	Hp_mech_error	Nilsson_error
994.5	1113.00	783.94	1288.02	3.05	2.89	3.11	5.0%	-2.1%
998.9	1057.00	714.83	1169.66	3.02	2.85	3.07	5.6%	-1.5%
1054.1	461.85	294.82	461.34	2.66	2.47	2.66	7.3%	0.0%
1136.3	158.02	96.95	139.95	2.20	1.99	2.15	9.7%	2.4%
1295.6	29.57	18.47	23.15	1.47	1.27	1.36	13.9%	7.2%

Table 20. Relative error of HP Mech and Nilsson ignition delay time simulation results relative to the experimental data for homogeneous CH_3OH-air mixtures of φ = 1, P = 10 atm, (Mixture 8).

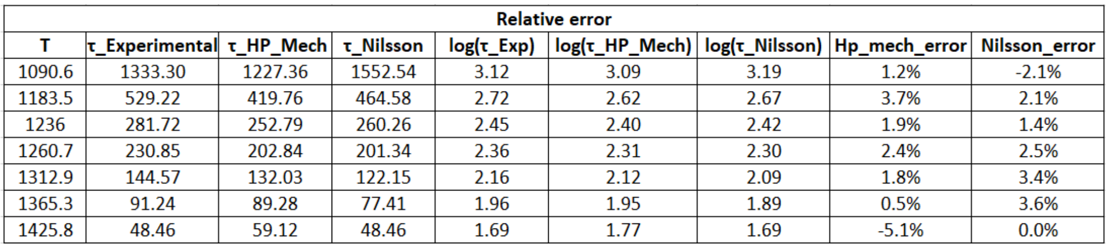

Relative error								
T	τ_Experimental	τ_HP_Mech	τ_Nilsson	log(τ_Exp)	log(τ_HP_Mech)	log(τ_Nilsson)	Hp_mech_error	Nilsson_error
1090.6	1333.30	1227.36	1552.54	3.12	3.09	3.19	1.2%	-2.1%
1183.5	529.22	419.76	464.58	2.72	2.62	2.67	3.7%	2.1%
1236	281.72	252.79	260.26	2.45	2.40	2.42	1.9%	1.4%
1260.7	230.85	202.84	201.34	2.36	2.31	2.30	2.4%	2.5%
1312.9	144.57	132.03	122.15	2.16	2.12	2.09	1.8%	3.4%
1365.3	91.24	89.28	77.41	1.96	1.95	1.89	0.5%	3.6%
1425.8	48.46	59.12	48.46	1.69	1.77	1.69	-5.1%	0.0%

Table 21. Relative error of HP Mech and Nilsson ignition delay time simulation results relative to the experimental data for homogeneous CH_3OH-air mixtures of φ = 2, P = 1.96 atm, (Mixture 9).

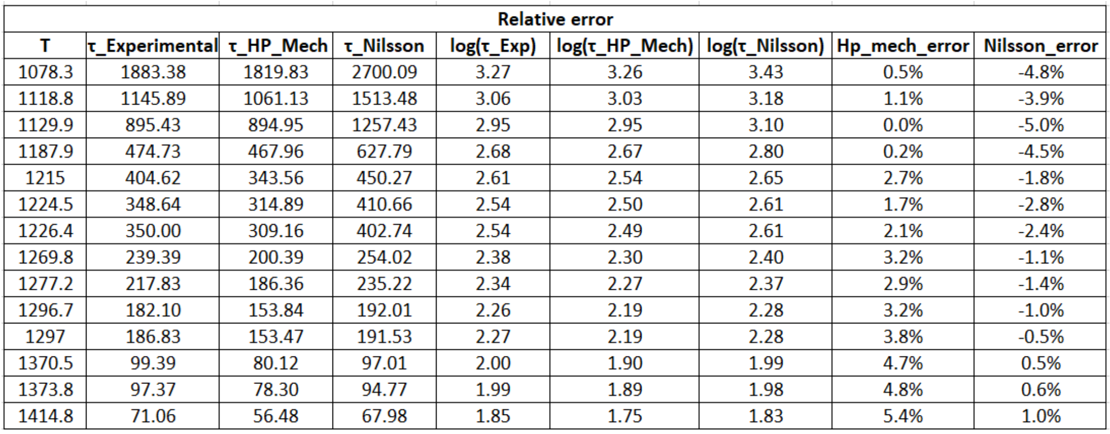

Relative error								
T	τ_Experimental	τ_HP_Mech	τ_Nilsson	log(τ_Exp)	log(τ_HP_Mech)	log(τ_Nilsson)	Hp_mech_error	Nilsson_error
1078.3	1883.38	1819.83	2700.09	3.27	3.26	3.43	0.5%	-4.8%
1118.8	1145.89	1061.13	1513.48	3.06	3.03	3.18	1.1%	-3.9%
1129.9	895.43	894.95	1257.43	2.95	2.95	3.10	0.0%	-5.0%
1187.9	474.73	467.96	627.79	2.68	2.67	2.80	0.2%	-4.5%
1215	404.62	343.56	450.27	2.61	2.54	2.65	2.7%	-1.8%
1224.5	348.64	314.89	410.66	2.54	2.50	2.61	1.7%	-2.8%
1226.4	350.00	309.16	402.74	2.54	2.49	2.61	2.1%	-2.4%
1269.8	239.39	200.39	254.02	2.38	2.30	2.40	3.2%	-1.1%
1277.2	217.83	186.36	235.22	2.34	2.27	2.37	2.9%	-1.4%
1296.7	182.10	153.84	192.01	2.26	2.19	2.28	3.2%	-1.0%
1297	186.83	153.47	191.53	2.27	2.19	2.28	3.8%	-0.5%
1370.5	99.39	80.12	97.01	2.00	1.90	1.99	4.7%	0.5%
1373.8	97.37	78.30	94.77	1.99	1.89	1.98	4.8%	0.6%
1414.8	71.06	56.48	67.98	1.85	1.75	1.83	5.4%	1.0%

Table 22. Relative error of HP Mech and Nilsson ignition delay time simulation results relative to the experimental data for homogeneous CH_3OH-air mixtures of φ = 2, P = 51 atm, (Mixture 10).

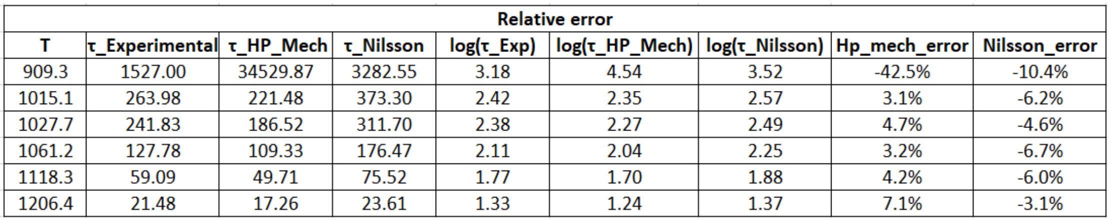

Relative error								
T	τ_Experimental	τ_HP_Mech	τ_Nilsson	log(τ_Exp)	log(τ_HP_Mech)	log(τ_Nilsson)	Hp_mech_error	Nilsson_error
909.3	1527.00	34529.87	3282.55	3.18	4.54	3.52	-42.5%	-10.4%
1015.1	263.98	221.48	373.30	2.42	2.35	2.57	3.1%	-6.2%
1027.7	241.83	186.52	311.70	2.38	2.27	2.49	4.7%	-4.6%
1061.2	127.78	109.33	176.47	2.11	2.04	2.25	3.2%	-6.7%
1118.3	59.09	49.71	75.52	1.77	1.70	1.88	4.2%	-6.0%
1206.4	21.48	17.26	23.61	1.33	1.24	1.37	7.1%	-3.1%

3.4.2 PSR SIMULATIONS RELATIVE ERRORS

Table 23. Relative error of HP Mech and Nilsson CH_3OH mole fraction simulation results relative to the experimental data for neat CH_3OH combustion at φ = 0.2, P = 10 atm, (Mixture 1).

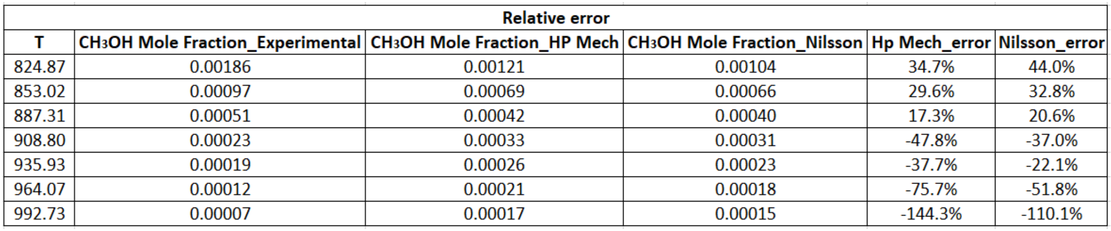

Relative error					
T	CH_3OH Mole Fraction_Experimental	CH_3OH Mole Fraction_HP Mech	CH_3OH Mole Fraction_Nilsson	Hp Mech_error	Nilsson_error
824.87	0.00186	0.00121	0.00104	34.7%	44.0%
853.02	0.00097	0.00069	0.00066	29.6%	32.8%
887.31	0.00051	0.00042	0.00040	17.3%	20.6%
908.80	0.00023	0.00033	0.00031	-47.8%	-37.0%
935.93	0.00019	0.00026	0.00023	-37.7%	-22.1%
964.07	0.00012	0.00021	0.00018	-75.7%	-51.8%
992.73	0.00007	0.00017	0.00015	-144.3%	-110.1%

Table 24. Relative error of HP Mech and Nilsson CH_3OH mole fraction simulation results relative to the experimental data for neat CH_3OH combustion at φ = 0.2, P = 10 atm, (Mixture 2).

Relative error					
T	CH_3OH Mole Fraction_Experimental	CH_3OH Mole Fraction_HP Mech	CH_3OH Mole Fraction_Nilsson	Hp Mech_error	Nilsson_error
798.32	0.00416	0.00329	0.00281	20.9%	32.3%
834.88	0.00349	0.00170	0.00158	51.3%	54.9%
871.44	0.00133	0.00094	0.00089	29.2%	33.5%
907.51	0.00044	0.00064	0.00056	-42.9%	-26.3%
944.07	0.00038	0.00046	0.00038	-20.9%	-1.3%
981.13	0.00025	0.00034	0.00028	-36.3%	-10.0%
1018.18	0.00014	0.00026	0.00020	-89.6%	-47.1%

Table 25. Relative error of HP Mech and Nilsson CH_3OH mole fraction simulation results relative to the experimental data for neat CH_3OH combustion at φ = 0.5, P = 20 atm, (Mixture 3).

Relative error					
T	CH_3OH Mole Fraction_Experimental	CH_3OH Mole Fraction_HP Mech	CH_3OH Mole Fraction_Nilsson	Hp Mech_error	Nilsson_error
800.97	0.00171	0.00079	0.00077	53.8%	55.1%
833.50	0.00064	0.00039	0.00042	39.8%	34.3%
866.02	0.00024	0.00024	0.00025	-1.8%	-3.9%
897.09	0.00010	0.00018	0.00017	-88.5%	-73.9%
927.18	0.00005	0.00014	0.00012	-185.3%	-147.3%

Table 26. Relative error of HP Mech and Nilsson CH_3OH mole fraction simulation results relative to the experimental data for neat CH_3OH combustion at φ = 1, P = 20 atm, (Mixture 4).

Relative error					
T	CH_3OH Mole Fraction_Experimental	CH_3OH Mole Fraction_HP Mech	CH_3OH Mole Fraction_Nilsson	Hp Mech_error	Nilsson_error
802.14	0.00229	0.00089	0.00088	61.0%	61.4%
832.86	0.00106	0.00047	0.00050	55.3%	52.5%
864.47	0.00044	0.00031	0.00030	31.3%	31.9%
895.54	0.00022	0.00022	0.00020	-3.7%	6.5%
929.54	0.00013	0.00017	0.00014	-29.8%	-9.2%
960.09	0.00007	0.00014	0.00011	-99.7%	-63.1%
992.61	0.00003	0.00011	0.00009	-231.4%	-166.6%

Table 27. Relative error of HP Mech and Nilsson CH_3OH mole fraction simulation results relative to the experimental data for neat CH_3OH combustion at φ = 9, P = 100 atm, (Mixture 5).

Relative error					
T	CH_3OH Mole Fraction_Experimental	CH_3OH Mole Fraction_HP Mech	CH_3OH Mole Fraction_Nilsson	Hp Mech_error	Nilsson_error
534.8	0.0262	0.0265	0.0265	-1.3%	-1.3%
585.5	0.0264	0.0265	0.0265	-0.3%	-0.3%
589.7	0.0266	0.0265	0.0265	0.2%	0.2%
616.0	0.0262	0.0265	0.0265	-1.2%	-1.2%
636.2	0.0262	0.0265	0.0265	-1.3%	-1.3%
667.2	0.0260	0.0265	0.0265	-1.9%	-2.0%
709.1	0.0228	0.0247	0.0257	-8.6%	-13.1%
732.4	0.0205	0.0221	0.0234	-7.8%	-14.3%
750.0	0.0186	0.0209	0.0204	-12.9%	-10.0%
772.2	0.0174	0.0197	0.0179	-13.4%	-3.0%
803.8	0.0163	0.0177	0.0120	-8.7%	26.7%
840.0	0.0139	0.0148	0.0053	-6.7%	62.0%
867.4	0.0106	0.0117	0.0025	-10.6%	76.8%
890.2	0.0076	0.0086	0.0013	-12.4%	82.5%

Table 28. Relative error of HP Mech and Nilsson CH_3OH mole fraction simulation results relative to the experimental data for neat CH_3OH combustion at φ = 1, P = 100 atm, (Mixture 6).

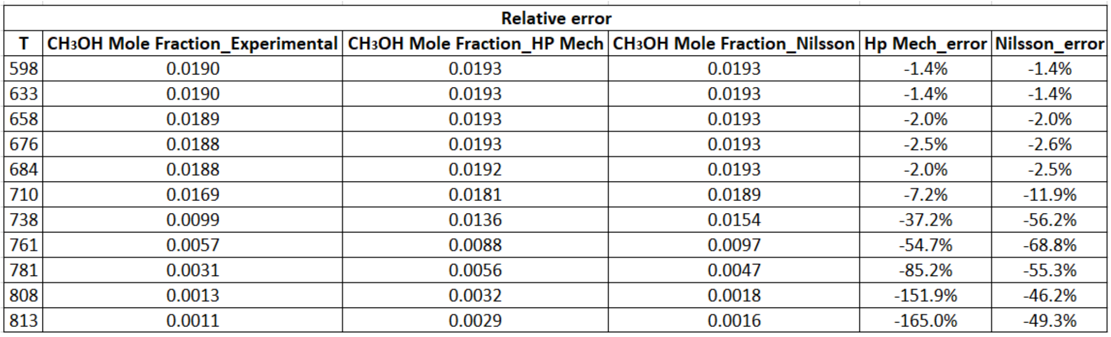

Relative error					
T	CH_3OH Mole Fraction_Experimental	CH_3OH Mole Fraction_HP Mech	CH_3OH Mole Fraction_Nilsson	Hp Mech_error	Nilsson_error
598	0.0190	0.0193	0.0193	-1.4%	-1.4%
633	0.0190	0.0193	0.0193	-1.4%	-1.4%
658	0.0189	0.0193	0.0193	-2.0%	-2.0%
676	0.0188	0.0193	0.0193	-2.5%	-2.6%
684	0.0188	0.0192	0.0193	-2.0%	-2.5%
710	0.0169	0.0181	0.0189	-7.2%	-11.9%
738	0.0099	0.0136	0.0154	-37.2%	-56.2%
761	0.0057	0.0088	0.0097	-54.7%	-68.8%
781	0.0031	0.0056	0.0047	-85.2%	-55.3%
808	0.0013	0.0032	0.0018	-151.9%	-46.2%
813	0.0011	0.0029	0.0016	-165.0%	-49.3%

Table 29. Relative error of HP Mech and Nilsson CH_3OH mole fraction simulation results relative to the experimental data for neat CH_3OH combustion at φ = 0.1, P = 100 atm, (Mixture 7).

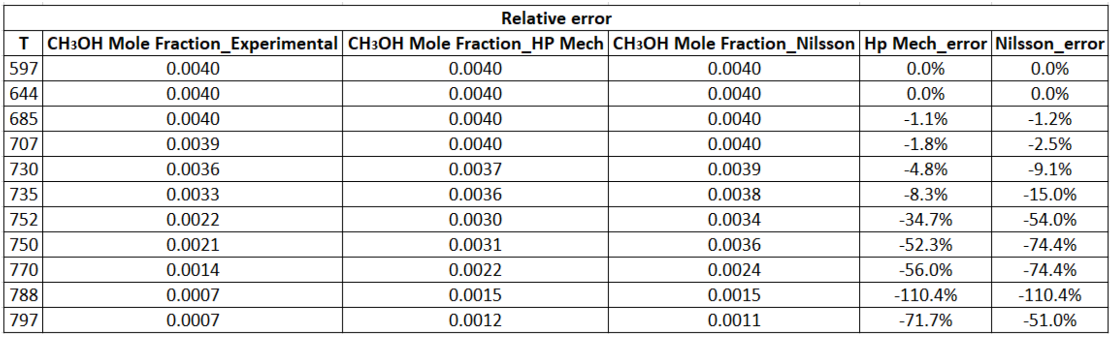

Relative error					
T	CH_3OH Mole Fraction_Experimental	CH_3OH Mole Fraction_HP Mech	CH_3OH Mole Fraction_Nilsson	Hp Mech_error	Nilsson_error
597	0.0040	0.0040	0.0040	0.0%	0.0%
644	0.0040	0.0040	0.0040	0.0%	0.0%
685	0.0040	0.0040	0.0040	-1.1%	-1.2%
707	0.0039	0.0040	0.0040	-1.8%	-2.5%
730	0.0036	0.0037	0.0039	-4.8%	-9.1%
735	0.0033	0.0036	0.0038	-8.3%	-15.0%
752	0.0022	0.0030	0.0034	-34.7%	-54.0%
750	0.0021	0.0031	0.0036	-52.3%	-74.4%
770	0.0014	0.0022	0.0024	-56.0%	-74.4%
788	0.0007	0.0015	0.0015	-110.4%	-110.4%
797	0.0007	0.0012	0.0011	-71.7%	-51.0%

Table 30. Relative error of HP Mech and Nilsson CH_3OH mole fraction simulation results relative to the experimental data for neat CH_3OH combustion at φ = 9, P = 10 atm, (Mixture 8).

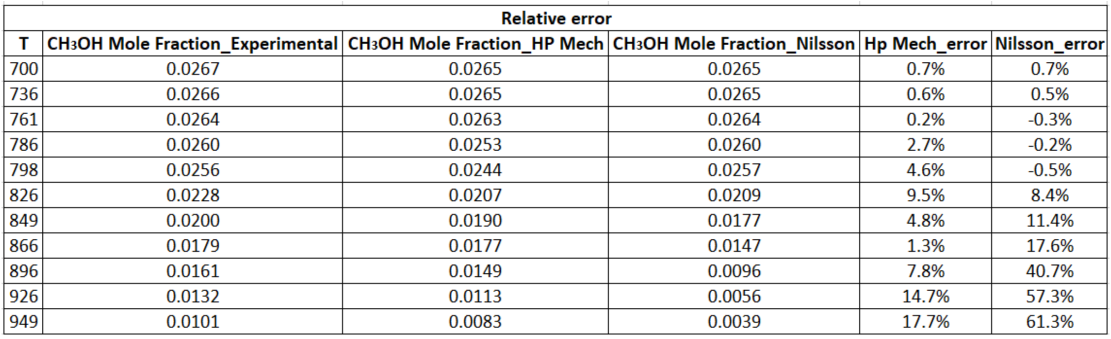

Relative error					
T	CH_3OH Mole Fraction_Experimental	CH_3OH Mole Fraction_HP Mech	CH_3OH Mole Fraction_Nilsson	Hp Mech_error	Nilsson_error
700	0.0267	0.0265	0.0265	0.7%	0.7%
736	0.0266	0.0265	0.0265	0.6%	0.5%
761	0.0264	0.0263	0.0264	0.2%	-0.3%
786	0.0260	0.0253	0.0260	2.7%	-0.2%
798	0.0256	0.0244	0.0257	4.6%	-0.5%
826	0.0228	0.0207	0.0209	9.5%	8.4%
849	0.0200	0.0190	0.0177	4.8%	11.4%
866	0.0179	0.0177	0.0147	1.3%	17.6%
896	0.0161	0.0149	0.0096	7.8%	40.7%
926	0.0132	0.0113	0.0056	14.7%	57.3%
949	0.0101	0.0083	0.0039	17.7%	61.3%

Table 31. Relative error of HP Mech and Nilsson CH_3OH mole fraction simulation results relative to the experimental data for neat CH_3OH combustion at φ = 1, P = 10 atm, (Mixture 9).

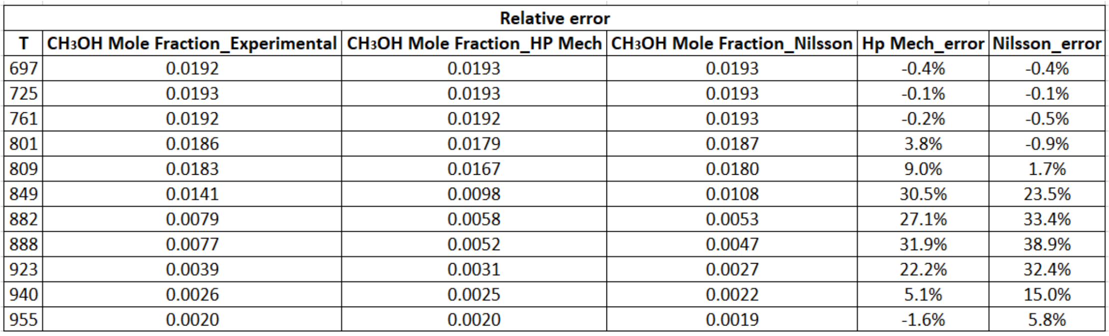

Relative error					
T	CH_3OH Mole Fraction_Experimental	CH_3OH Mole Fraction_HP Mech	CH_3OH Mole Fraction_Nilsson	Hp Mech_error	Nilsson_error
697	0.0192	0.0193	0.0193	-0.4%	-0.4%
725	0.0193	0.0193	0.0193	-0.1%	-0.1%
761	0.0192	0.0192	0.0193	-0.2%	-0.5%
801	0.0186	0.0179	0.0187	3.8%	-0.9%
809	0.0183	0.0167	0.0180	9.0%	1.7%
849	0.0141	0.0098	0.0108	30.5%	23.5%
882	0.0079	0.0058	0.0053	27.1%	33.4%
888	0.0077	0.0052	0.0047	31.9%	38.9%
923	0.0039	0.0031	0.0027	22.2%	32.4%
940	0.0026	0.0025	0.0022	5.1%	15.0%
955	0.0020	0.0020	0.0019	-1.6%	5.8%

Table 32. Relative error of HP Mech and Nilsson CH_3OH mole fraction simulation results relative to the experimental data for neat CH_3OH combustion at φ = 0.1, P = 10 atm, (Mixture 10).

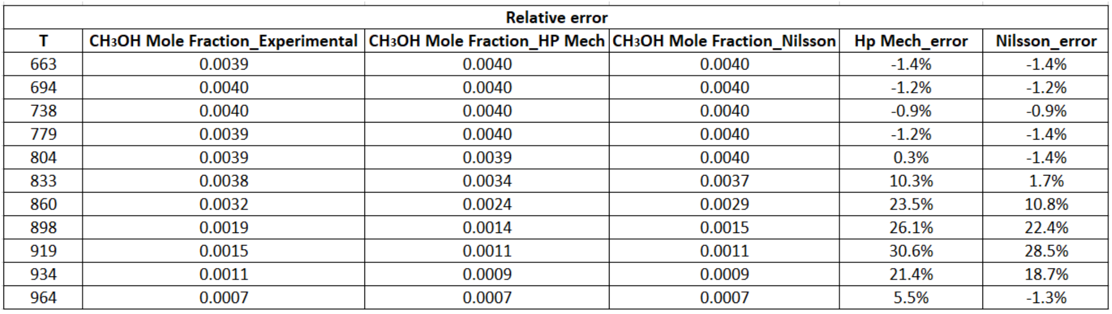

Relative error					
T	CH_3OH Mole Fraction_Experimental	CH_3OH Mole Fraction_HP Mech	CH_3OH Mole Fraction_Nilsson	Hp Mech_error	Nilsson_error
663	0.0039	0.0040	0.0040	-1.4%	-1.4%
694	0.0040	0.0040	0.0040	-1.2%	-1.2%
738	0.0040	0.0040	0.0040	-0.9%	-0.9%
779	0.0039	0.0040	0.0040	-1.2%	-1.4%
804	0.0039	0.0039	0.0040	0.3%	-1.4%
833	0.0038	0.0034	0.0037	10.3%	1.7%
860	0.0032	0.0024	0.0029	23.5%	10.8%
898	0.0019	0.0014	0.0015	26.1%	22.4%
919	0.0015	0.0011	0.0011	30.6%	28.5%
934	0.0011	0.0009	0.0009	21.4%	18.7%
964	0.0007	0.0007	0.0007	5.5%	-1.3%

3.4.3 LFS SIMULATIONS RELATIVE ERRORS

Table 33. Relative error of HP Mech and Nilsson laminar flame speed simulation results relative to the experimental data for neat CH_3OH combustion, at P = 1.0 bar and T_{un} = 373 K (Mixture 1).

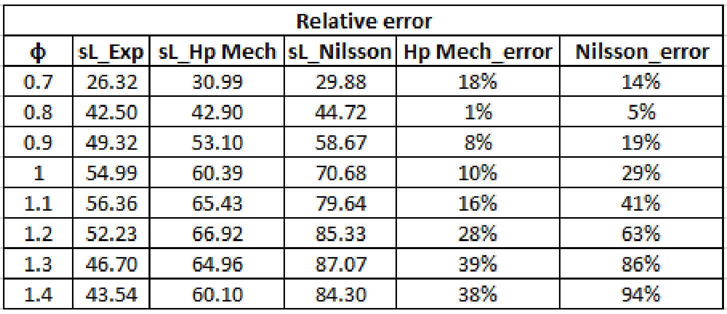

Relative error					
ɸ	sL_Exp	sL_Hp Mech	sL_Nilsson	Hp Mech_error	Nilsson_error
0.7	26.32	30.99	29.88	18%	14%
0.8	42.50	42.90	44.72	1%	5%
0.9	49.32	53.10	58.67	8%	19%
1	54.99	60.39	70.68	10%	29%
1.1	56.36	65.43	79.64	16%	41%
1.2	52.23	66.92	85.33	28%	63%
1.3	46.70	64.96	87.07	39%	86%
1.4	43.54	60.10	84.30	38%	94%

Table 34. Relative error of HP Mech and Nilsson laminar flame speed simulation results relative to the experimental data for neat CH_3OH combustion, at P = 5.0 bar and T_{un} = 373 K (Mixture 2).

Relative error					
ϕ	sL_Exp	sL_Hp Mech	sL_Nilsson	Hp Mech_error	Nilsson_error
0.7	19.09	17.71	16.10	-7%	-16%
0.8	27.48	25.79	25.53	-6%	-7%
0.9	35.17	33.08	35.45	-6%	1%
1	40.77	38.73	45.25	-5%	11%
1.1	41.61	42.24	52.81	2%	27%
1.2	39.37	42.94	57.70	9%	47%
1.3	35.04	40.81	59.17	16%	69%
1.4	30.28	36.41	57.08	20%	89%

Table 35. Relative error of HP Mech and Nilsson laminar flame speed simulation results relative to the experimental data for neat CH_3OH combustion, at P = 10 bar and T_{un} = 373 K (Mixture 3).

Relative error					
ϕ	sL_Exp	sL_Hp Mech	sL_Nilsson	Hp Mech_error	Nilsson_error
0.712	13.52	13.55	12.35	0%	-9%
0.816	24.64	19.79	19.52	-20%	-21%
0.918	29.02	25.31	27.17	-13%	-6%
1.016	35.39	29.30	33.89	-17%	-4%
1.124	37.92	31.63	40.07	-17%	6%
1.221	37.88	31.27	43.10	-17%	14%
1.326	33.22	28.71	43.37	-14%	31%

Table 36. Relative error of HP Mech and Nilsson laminar flame speed simulation results relative to the experimental data for neat CH_3OH combustion, at P = 1 atm and T_{un} = 298 K (Mixture 4).

Relative error					
ϕ	sL_Exp	sL_Hp Mech	sL_Nilsson	Hp Mech_error	Nilsson_error
0.7	20.5	20.45	18.00	0%	-12%
0.8	29.2	28.28	30.37	-3%	4%
0.9	37.1	37.06	41.33	0%	11%
1	43.2	42.01	49.40	-3%	14%
1.1	46.3	45.61	57.54	-1%	24%
1.5	34.6	35.52	54.63	3%	58%

Table 37. Relative error of HP Mech and Nilsson laminar flame speed simulation results relative to the experimental data for neat CH_3OH combustion, at P = 1 atm and T_{un} = 423 K (Mixture 5).

Relative error					
ϕ	sL_Exp	sL_Hp Mech	sL_Nilsson	Hp Mech_error	Nilsson_error
0.8	50.91	53.63	55.83	5%	10%
0.9	61.35	65.26	72.83	6%	19%
1	69.16	74.14	86.29	7%	25%
1.1	75.30	79.66	96.92	6%	29%
1.2	76.25	81.84	103.40	7%	36%
1.3	73.78	79.80	105.40	8%	43%

CHAPTER 4: Study of methanol combustion in supercritical CO_2 conditions

Extremely high-pressure combustion is an emerging technique for enhancing thermodynamic efficiency and lowering pollutant emissions. Under such high-pressure conditions, multiple body collisions may cause significant uncertainties of the rate constants calculated using the typical transition state theory. Consequently, the pressure dependency of reaction rates should be re-evaluated for the transition from gas-phase to supercritical conditions. Furthermore, thermodynamic properties and transport properties may deviate significantly from the ideal gas law at ultrahigh pressures. Therefore, it is enormously valuable to perform kinetics experiments of CH_3OH oxidation and to develop its chemical kinetic model under extremely high-pressure conditions (above 100 atm).

No experimental data relating to the above conditions were found in the literature.

4.1 Ignition delay time

The main aim of the investigation presented here is to identify the differences between the ignition delay times of methanol mixtures in sCO_2 conditions and the more 'conventional' ignition delay times of methanol mixtures, represented by N_2 diluent conditions. To this end, the ACR55 mechanism is employed to quantify the effect of the sCO_2 environment on the ignition delay times of CH_3OH-O_2 mixtures, as well as to quantify the ignition delay time of methanol mixtures in an N_2 diluent environment. In particular, computational results of ignition delay times are presented here for methanol-oxygen mixtures. These results cover a pressure range of p=175-250 bar, a temperature range of T=1300-1800 K, and an equivalence ratio range of φ=0.5-2.0. They encompass a substantial range of conditions and local mixture compositions found in many practical applications, including gas turbines. It is noted that in all cases investigated, the percentage of either CO_2 or N_2 was 85%, consistent with the corresponding percentage found in the literature characterizing applications operating in an sCO_2 environment. Initial conditions for all mixtures investigated are presented in Table 38. It is noted that, due to the lack of experimental data in these conditions (i.e., high pressures, sCO_2 environment), results of the Updated HP-Mech mechanism are also included as a validation backbone.

Table 38. Simulations of ignition in homogeneous methanol mixtures: values of equivalence ratio, initial pressure and temperature, and initial concentration of CH_3OH, O_2, CO_2/ N_2.

φ	p (bar)	T(K)	CH_3OH (%)	O_2 (%)	CO_2/N_2 (%)
0.5	175.0	1300-1800	3.75	11.25	85.00
0.5	200.0	1300-1800	3.75	11.25	85.00
0.5	220.0	1300-1800	3.75	11.25	85.00
0.5	250.0	1300-1800	3.75	11.25	85.00
0.8	175.0	1300-1800	5.22	9.78	85.00
0.8	200.0	1300-1800	5.22	9.78	85.00
0.8	220.0	1300-1800	5.22	9.78	85.00
0.8	250.0	1300-1800	5.22	9.78	85.00
1.0	175.0	1300-1800	6.00	9.00	85.00
1.0	200.0	1300-1800	6.00	9.00	85.00
1.0	220.0	1300-1800	6.00	9.00	85.00
1.0	250.0	1300-1800	6.00	9.00	85.00
1.5	175.0	1300-1800	7.50	7.50	85.00

1.5	200.0	1300-1800	7.50	7.50	85.00
1.5	220.0	1300-1800	7.50	7.50	85.00
1.5	250.0	1300-1800	7.50	7.50	85.00
2.0	175.0	1300-1800	8.57	6.43	85.00
2.0	200.0	1300-1800	8.57	6.43	85.00
2.0	220.0	1300-1800	8.57	6.43	85.00
2.0	250.0	1300-1800	8.57	6.43	85.00

Figures 46-49 present computational results of ignition delay time for lean CH_3OH-O_2 mixtures (φ=0.5, 0.8) at pressures ranging from 175 to 250 bar, illustrating the effects of pressure and sCO_2 conditions on ignition. These results confirm that ignition delay times for both the ACR55 and Updated HP-Mech mechanisms are within the same order of magnitude under these conditions (high pressures, sCO_2 environment). Additionally, ignition delay times in an N_2 environment are higher compared to those in the sCO_2 environment at the high-temperature regime for stoichiometries of φ=0.5 and 0.8 (refer to Figures 46-49). This trend is observed in the results of both the ACR55 and Updated HP-Mech mechanisms. However, particularly in the case of φ=0.5, the ACR55 mechanism exhibits a quite milder trend. Finally, the trend of higher ignition delay times in the N_2 environment compared to those observed in the sCO_2 conditions gradually diminishes as the pressure increases, in terms of the extent of the temperature range over which this phenomenon is observed. For instance, concerning the results of the ACR55 mechanism, at a stoichiometry of φ=0.8 and pressure of p=175 bar, the temperature regime in which ignition delay times in the N_2 environment are higher compared to those in the sCO_2 environment spans T=1550-1800 K. Similarly, for a stoichiometry of φ=0.8 and pressure of p=250 bar, the corresponding temperature regime is T=1730-1800 K (see Figures 48(a) and 49). Computations for the stoichiometric case (Figure 50) demonstrate a significant resemblance to those shown for φ=0.8. As a direct result of this similarity, the trend of higher ignition delay times in the N_2 environment compared to those in the sCO_2 environment persists for the stoichiometric case with exactly the same characteristics. (this trend is observed in a larger temperature regime for low pressures and in a lower temperature regime as the pressure rises). The results for the rich mixtures (φ=1.5, 2.0 – Figures 51 and 52) demonstrate that the trend of higher ignition delay times in the N_2 environment compared to those in the sCO_2 conditions has been eliminated. An exception to this outcome is observed in the case of φ=1.5 and p=175 bar, where higher ignition delay times in the N_2 environment are observed within a very narrow temperature range (1750-1800 K) among the considered temperature ranges.

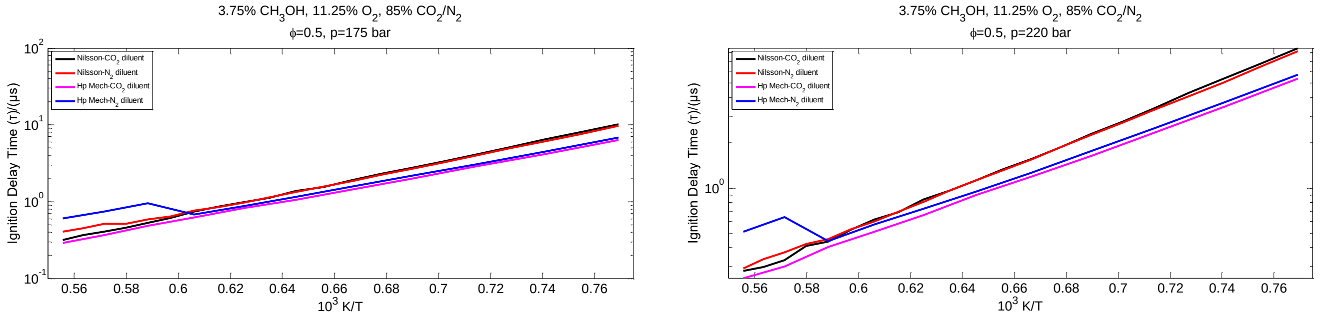

Figure 46. Ignition delay time profiles versus initial temperature for homogeneous CH_3OH-air mixtures of (a) φ = 0.5, P = 175 bar, (Mixture 1); and (b) φ = 0.5, P = 220 bar (Mixture 2), with mixture composition per volume: 3.75% CH_3OH, 11.25% O_2, 85% N_2/CO_2.

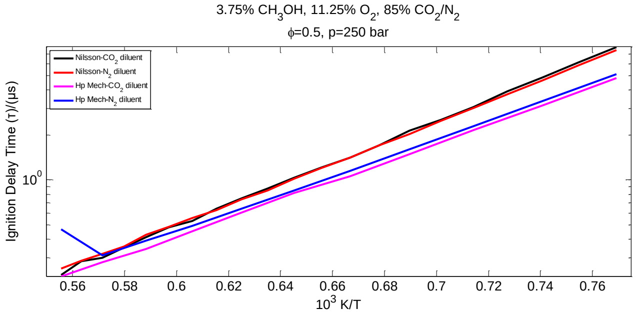

Figure 47. Ignition delay time profiles versus initial temperature for homogeneous CH_3OH-air mixtures of $\varphi = 0.5$, P = 250 bar, (Mixture 3) and with mixture composition per volume: 3.75% CH_3OH, 11.25% O_2, 85% N_2/CO_2

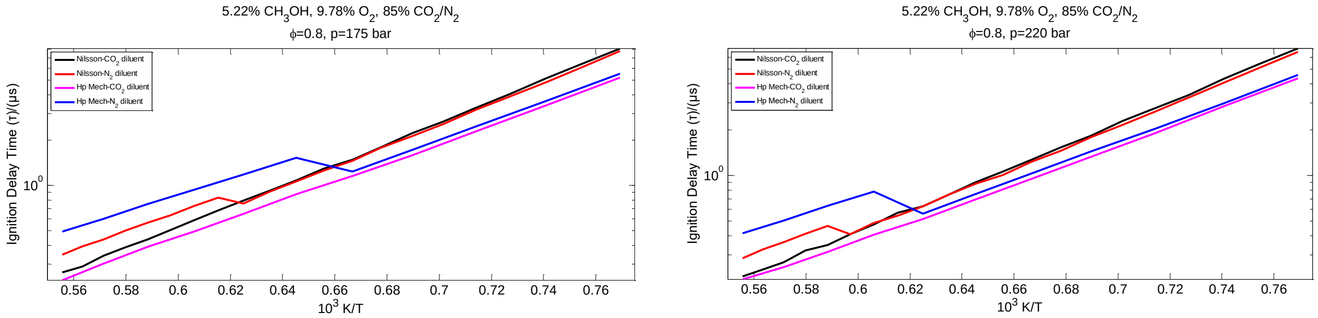

Figure 48. Ignition delay time profiles versus initial temperature for homogeneous CH_3OH-air mixtures of (a) $\varphi = 0.8$, P = 175 bar, (Mixture 4); and (b) $\varphi = 0.8$, P = 220 bar (Mixture 5), with mixture composition per volume: 5.22% CH_3OH, 9.78% O_2, 85% N_2/CO_2.

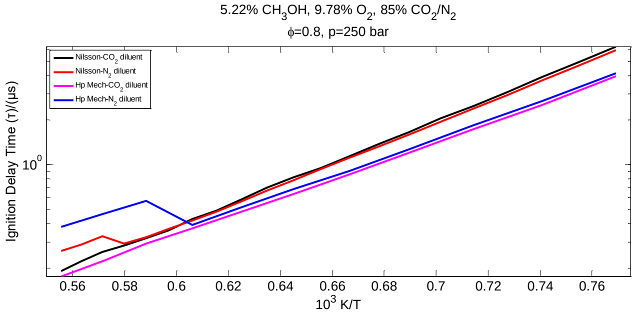

Figure 49. Ignition delay time profiles versus initial temperature for homogeneous CH_3OH-air mixtures of $\varphi = 0.8$, P = 250 bar, (Mixture 6) and with mixture composition per volume: 5.22% CH_3OH, 9.78% O_2, 85% N_2/CO_2.

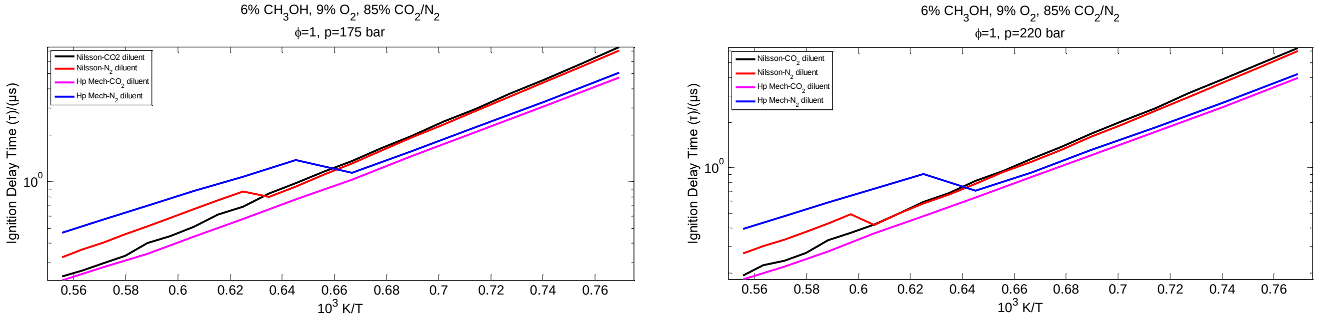

Figure 50. Ignition delay time profiles versus initial temperature for homogeneous CH_3OH-air mixtures of (a) $\varphi = 1$, P = 175 bar, (Mixture 7); and (b) $\varphi = 1$, P = 220 bar (Mixture 8), with mixture composition per volume: 6% CH_3OH, 9% O_2, 85% N_2/CO_2.

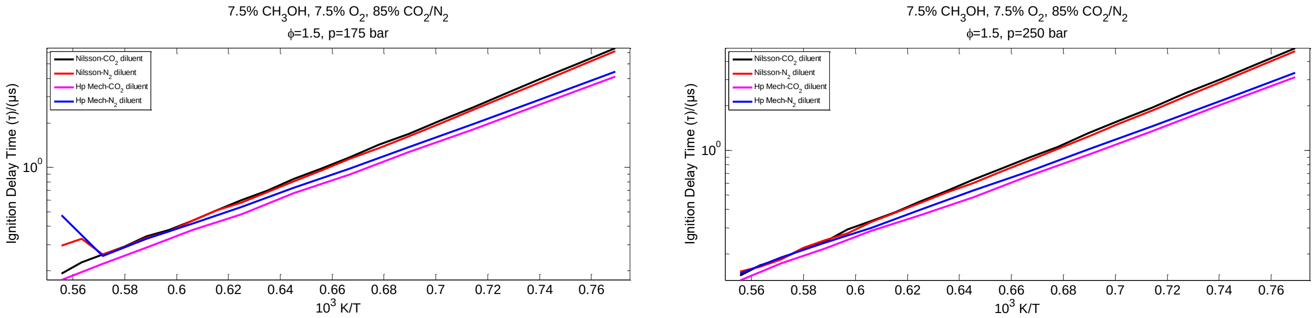

Figure 51. Ignition delay time profiles versus initial temperature for homogeneous CH_3OH-air mixtures of (a) φ = 1, P = 175 bar, (Mixture 9); and (b) φ = 1.5, P = 250 bar (Mixture 10), with mixture composition per volume: 7.5% CH_3OH, 7.5% O_2, 85% N_2/CO_2.

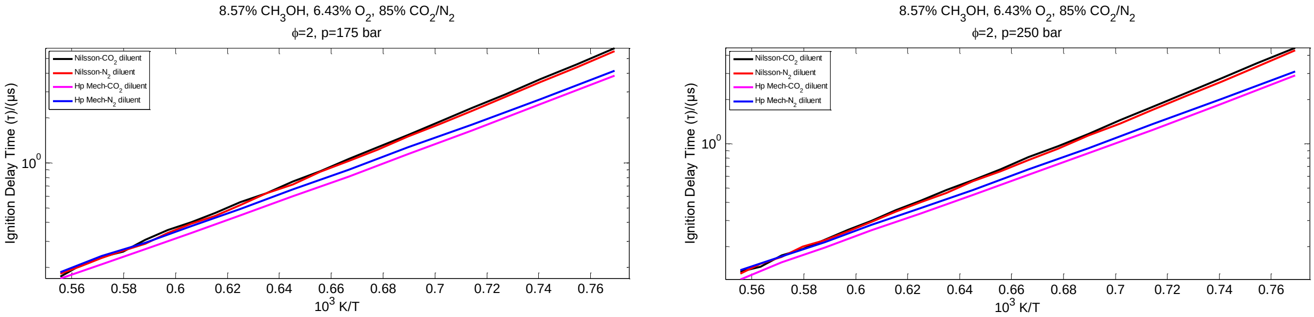

Figure 52. Ignition delay time profiles versus initial temperature for homogeneous CH_3OH-air mixtures of (a) φ = 2, P = 175 bar, (Mixture 11); and (b) φ = 2, P = 250 bar (Mixture 12), with mixture composition per volume: 8.57% CH_3OH, 6.43% O_2, 85% N_2/CO_2.

4.2 Concentration profiles as function of temperature

In this section, the ACR55 mechanism is utilized to quantify the effect of sCO_2 conditions on the combustion of CH_3OH–O_2 mixtures at PSR conditions, in comparison to combustion in an N_2 environment. Once again, in the absence of relevant experimental data, results of the Updated HP-Mech are also included for comparison. In particular, simulations were performed for the conditions and mixtures outlined in Table 38, covering pressures ranging from p=175 to 250 bar, temperatures from T=1300 to 1800 K, and stoichiometry from φ=0.5 to 2.0. It is worth noting that a residence time of τ=0.43 s, as referenced in the work of Wang et al., was utilized in all computations. This choice stems from the fact that the experiments conducted by Wang et al. were carried out at pressures up to 100 bar, which closely aligns with the pressure conditions of interest in our investigation. Therefore, this specific value of residence time was selected for our study. Figures 21-30 present computational results for lean, stoichiometric, and rich mixtures of CH_3OH–O_2 combustion at PSR conditions in the presence of either N_2 or sCO_2. Specifically, the results depict fuel (methanol) consumption and the production of basic combustion products, namely carbon monoxide (CO) and carbon dioxide (CO_2), as a function of temperature (mole fraction profiles versus temperature). These results demonstrate three main behaviors regarding combustion at PSR conditions. Firstly, the fuel is fully consumed across the entire temperature range considered in all cases investigated, both in N_2 and sCO_2 supercritical conditions. Additionally, CO production is consistently higher in the sCO_2 environment compared to the N_2 environment in all cases (refer to Figures 54(a), 57(a), 60(a), 63(a), and 66(a)). The behavior of CO_2 production differs between lean and rich mixtures. It is noted that in the case of sCO_2 conditions, the production of CO_2 refers to the additional mole fraction of CO_2 produced beyond the initial 85% CO_2 mole fraction of the reactants considered. In particular, for lean mixtures, a production of CO_2 is observed in both N_2 and sCO_2 cases; however, the produced CO_2 is higher for the N_2 environment compared to the corresponding CO_2 production observed for the sCO_2 conditions across all the lean mixtures considered here (refer to Figures 54(b) and 57(b)). On the other hand, under fuel-rich conditions, the mole fraction of CO_2 presented in Figures 63(b) and 66(b) for the sCO_2 conditions corresponds to the mole fraction of CO_2 consumed with reference to the initial mole fraction of 85% CO_2.In other words, in the fuel-rich cases for sCO_2 conditions, the initial CO_2 is predominantly converted to CO, and this CO is not further converted back to CO_2 at the end of combustion. This trend explains the extremely high levels of CO observed for rich mixtures under sCO_2 conditions. It is worth noting that the stoichiometric case follows the trend of CO and CO_2 production demonstrated in lean mixtures (refer to Figure 60). In conclusion, similar computational results were obtained using both the ACR55 mechanism and the Updated HP-Mech mechanism, thus verifying their validity.

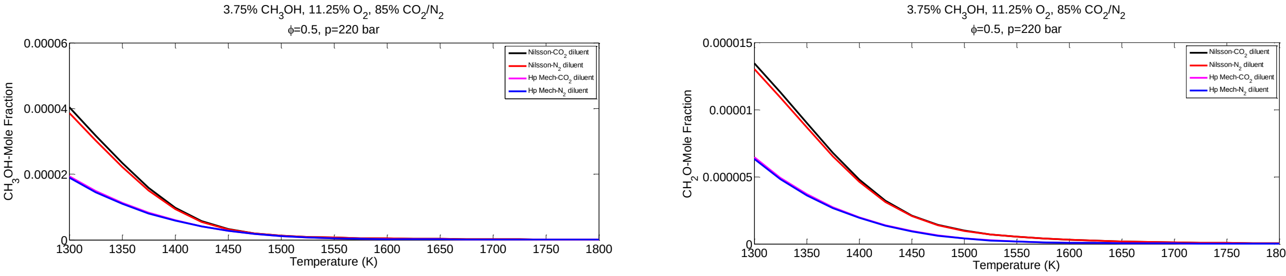

Figure 53. Mole fraction profiles versus temperature for CH_3OH combustion under PSR conditions at P = 220 bar, φ = 0.5, and τ_{res}=0.0.43 s of (a) CH_3OH; and (b) CH_2O. Mixture composition per volume: 3.75% CH_3OH, 11.25% O_2, 85% CO_2/ N_2 (Mixture 1).

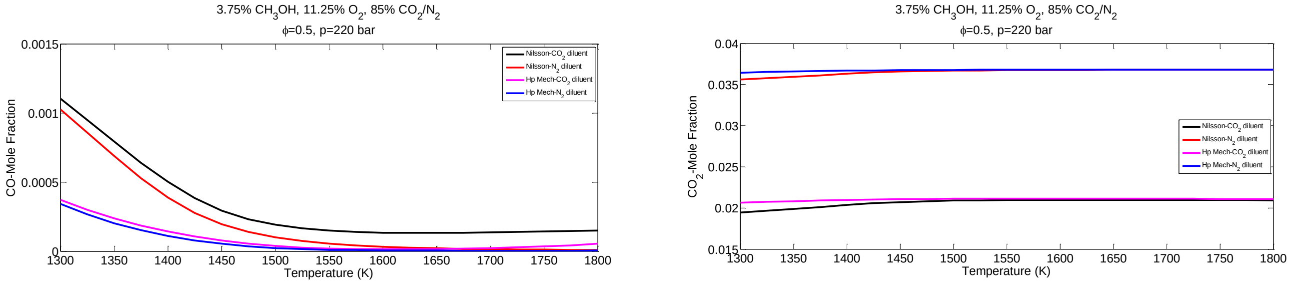

Figure 54. Mole fraction profiles versus temperature for neat CH_3OH combustion under PSR conditions at P = 220 bar, φ = 0.5, and τ_{res}=0.0.43 s of (a) CO; and (b) CO_2. Mixture composition per volume: 3.75% CH_3OH, 11.25% O_2, 85% CO_2/ N_2 (Mixture 1).

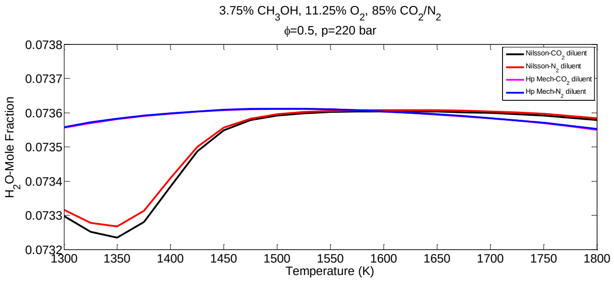

Figure 55. Mole fraction profiles versus temperature for neat CH_3OH combustion under PSR conditions at P = 220 bar, φ = 0.5, and τ_{res}=0.0.43 s of H_2O. Mixture composition per volume: 3.75% CH_3OH, 11.25% O_2, 85% CO_2/ N_2 (Mixture 1).

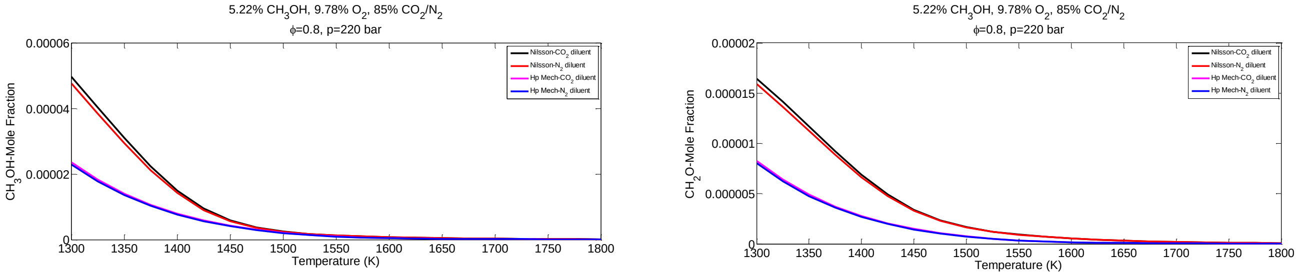

Figure 56. Mole fraction profiles versus temperature for CH_3OH combustion under PSR conditions at P = 220 bar, φ = 0.8, and τ_{res}=0.0.43 s of (a) CH_3OH; and (b) CH_2O. Mixture composition per volume: 5.22% CH_3OH, 9.78% O_2, 85% CO_2/ N_2 (Mixture 2).

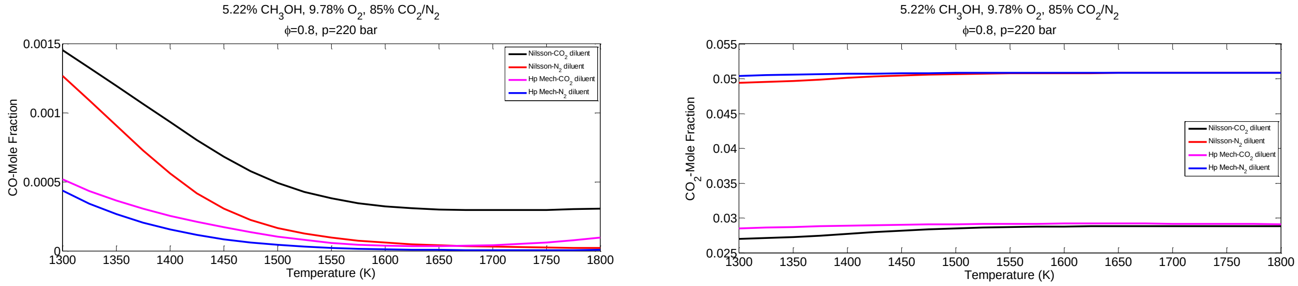

Figure 57. Mole fraction profiles versus temperature for neat CH_3OH combustion under PSR conditions at P = 220 bar, φ = 0.8, and τ_{res}=0.0.43 s of (a) CO; and (b) CO_2. Mixture composition per volume: 5.22% CH_3OH, 9.78% O_2, 85% CO_2/ N_2 (Mixture 2).

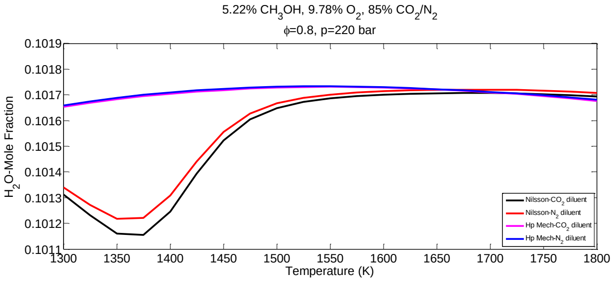

Figure 58. Mole fraction profiles versus temperature for neat CH_3OH combustion under PSR conditions at P = 220 bar, φ = 0.8, and τ_{res}=0.0.43 s of H_2O. Mixture composition per volume: 5.22% CH_3OH, 9.78% O_2, 85% CO_2/ N_2 (Mixture 2).

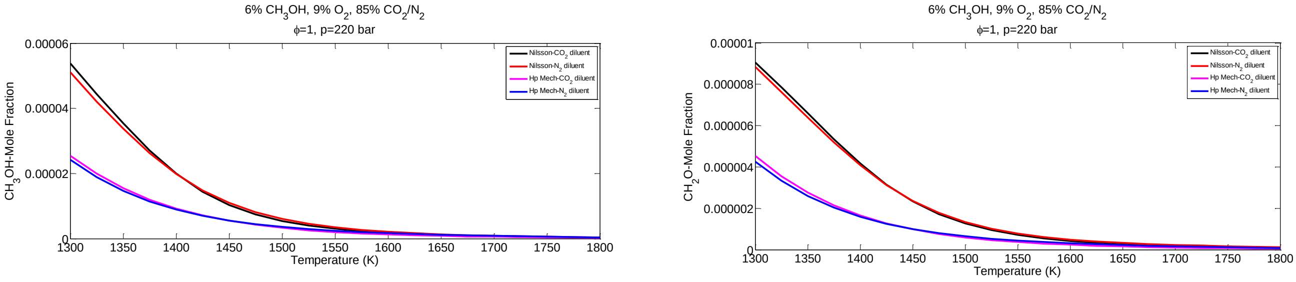

Figure 59. Mole fraction profiles versus temperature for CH_3OH combustion under PSR conditions at P = 220 bar, φ = 1, and τ_{res}=0.0.43 s of (a) CH_3OH; and (b) CH_2O. Mixture composition per volume: 6% CH_3OH, 9 % O_2, 85% CO_2/ N_2, (Mixture 3).

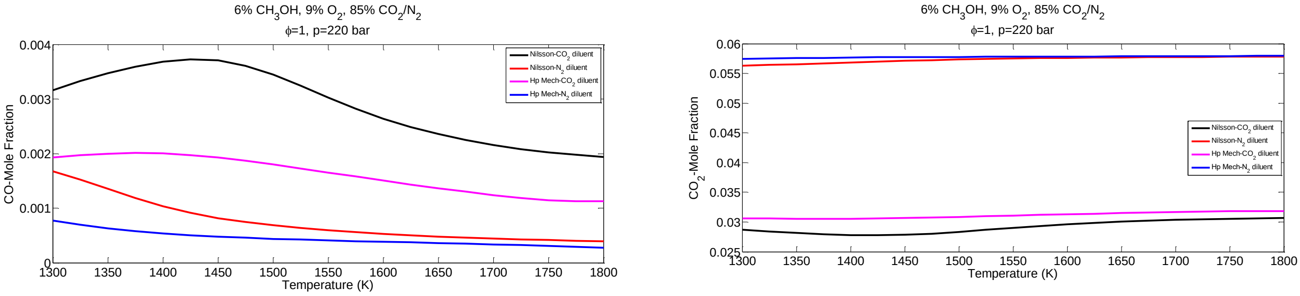

Figure 60. Mole fraction profiles versus temperature for neat CH_3OH combustion under PSR conditions at P = 220 bar, φ = 1, and τ_{res}=0.0.43 s of (a) CO; and (b) CO_2. Mixture composition per volume6% CH_3OH, 9 % O_2, 85% CO_2/ N_2, (Mixture 3).

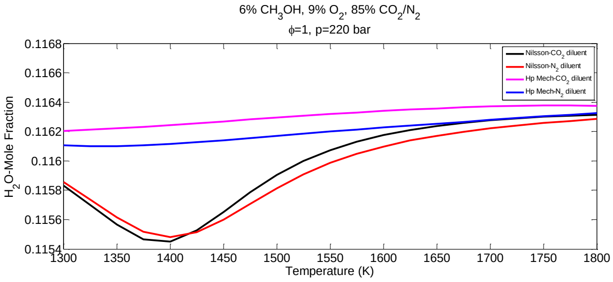

Figure 61. Mole fraction profiles versus temperature for neat CH_3OH combustion under PSR conditions at P = 220 bar, φ = 1, and τ_{res}=0.0.43 s of H_2O. Mixture composition per volume: 6% CH_3OH, 9 % O_2, 85% CO_2/ N_2, (Mixture 3).

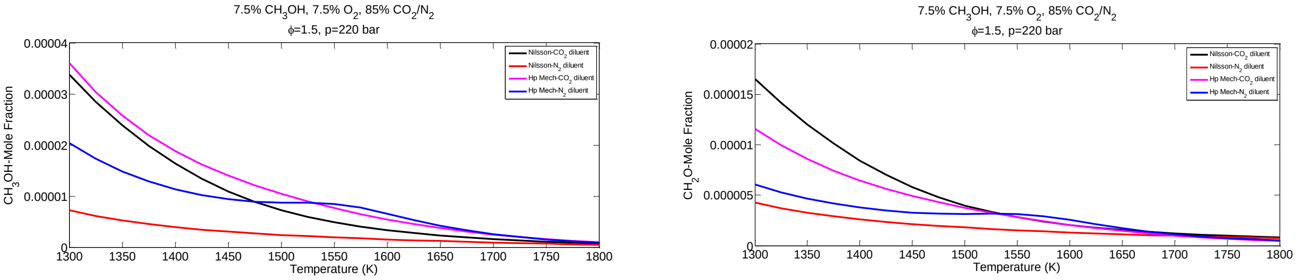

Figure 62. Mole fraction profiles versus temperature for CH_3OH combustion under PSR conditions at P = 220 bar, φ = 1.5, and τ_{res}=0.0.43 s of (a) CH_3OH; and (b) CH_2O. Mixture composition per volume: 7.5% CH_3OH, 7.5 % O_2, 85% CO_2/ N_2, (Mixture 4).

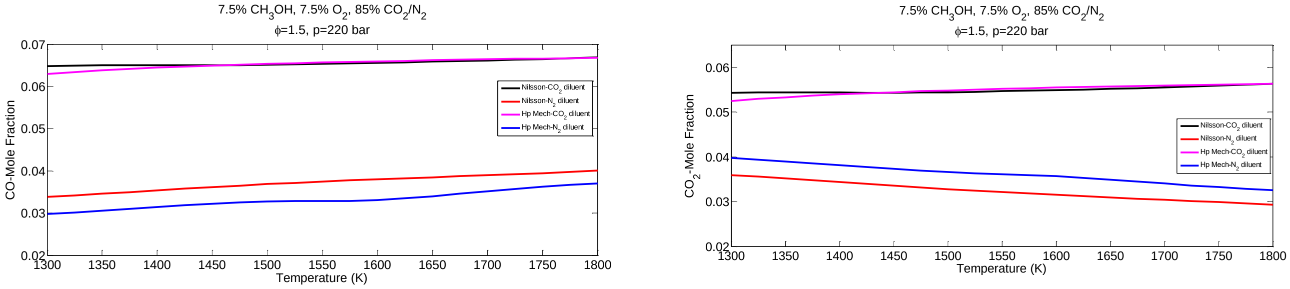

Figure 63. Mole fraction profiles versus temperature for neat CH_3OH combustion under PSR conditions at P = 220 bar, φ = 1.5, and τ_{res}=0.0.43 s of (a) CO; and (b) CO_2. Mixture composition per volume: 7.5% CH_3OH, 7.5 % O_2, 85% CO_2/ N_2, (Mixture 4).

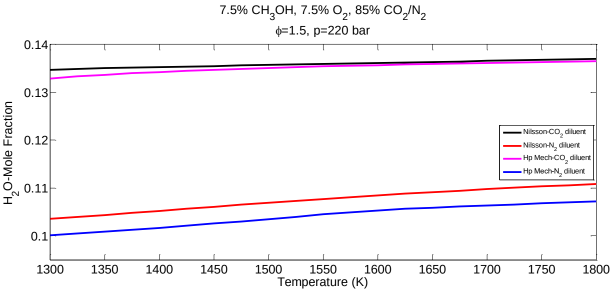

Figure 64. Mole fraction profiles versus temperature for neat CH_3OH combustion under PSR conditions at P = 220 bar, φ = 1.5, and τ_{res}=0.0.43 s of H_2O. Mixture composition per volume: 7.5% CH_3OH, 7.5 % O_2, 85% CO_2/ N_2, (Mixture 4).

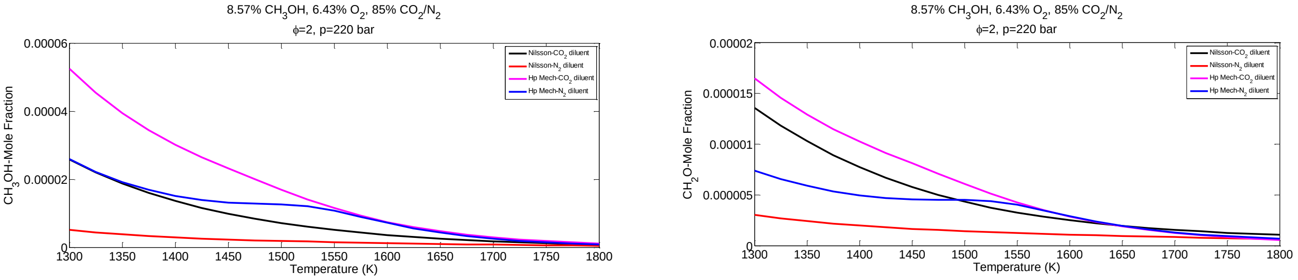

Figure 65. Mole fraction profiles versus temperature for CH_3OH combustion under PSR conditions at P = 220 bar, φ = 2, and τ_{res}=0.0.43 s of (a) CH_3OH; and (b) CH_2O. Mixture composition per volume: 8.57% CH_3OH, 6.43 % O_2,85% CO_2/ N_2, (Mixture 5).

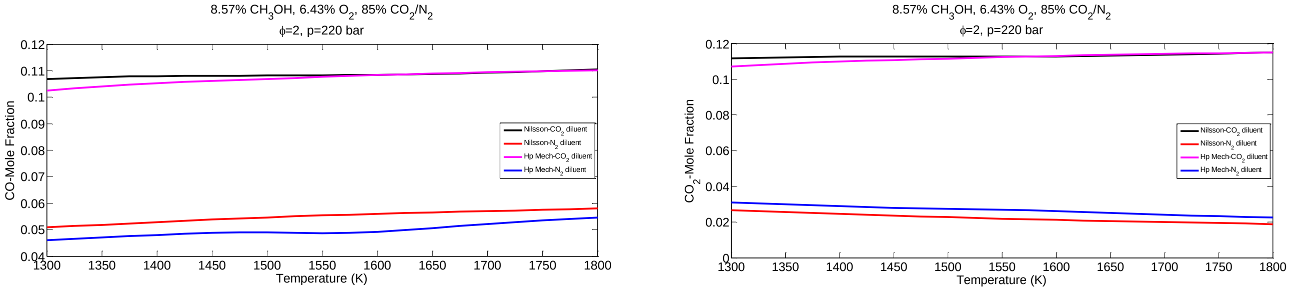

Figure 66. Mole fraction profiles versus temperature for neat CH_3OH combustion under PSR conditions at P = 220 bar, φ = 2, and τ_{res}=0.0.43 s of (a) CO; and (b) CO_2. Mixture composition per volume: 8.57% CH_3OH, 6.43 % O_2,85% CO_2/ N_2, (Mixture 5).

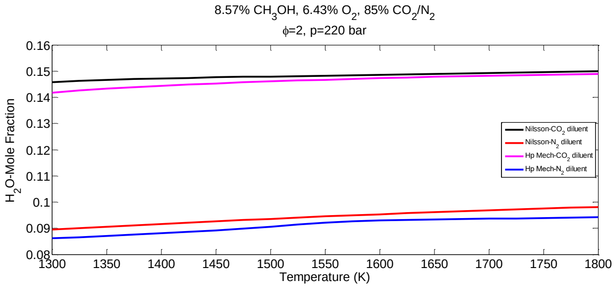

Figure 67. Mole fraction profiles versus temperature for neat CH_3OH combustion under PSR conditions at P = 220 bar, φ = 2, and τ_{res}=0.0.43 s of H_2O. Mixture composition per volume: 8.57% CH_3OH, 6.43 % O_2,85% CO_2/ N_2, (Mixture 5).

4.3 Premixed laminar flame speed

In this section, the main aim of the investigation presented is to identify the differences between the laminar flame speed of methanol mixtures in sCO_2 conditions and the laminar flame speed of methanol mixtures, represented by N_2 diluent conditions. The ACR55 mechanism is utilized to quantify the effect of sCO_2 conditions on the laminar flame speed of CH_3OH-O_2 mixtures, as well as to quantify the laminar flame speed of methanol mixtures in an N_2 diluent environment. In particular, computational results of laminar flame speed are presented here for methanol-oxygen mixtures. These results cover a pressure range of p=200-220 atm, a temperature range of T=600-1800 K, and an equivalence ratio range of φ=0.3-2.0. Figures 68-69 present computational results of laminar flame speed of CH_3OH–O_2 mixtures in the presence of either N_2 or sCO_2. These results confirm that laminar flame speeds for both the ACR55 and Updated HP-Mech mechanisms are within the same order of magnitude for N_2 and CO_2 diluents, respectively. Additionally, laminar flame speeds in an N_2 environment are higher compared to those in the sCO_2 environment across the entire range of temperature, equivalence ratio, and pressure. It is worth noting that laminar flame speeds reach their maximum value at stoichiometric conditions, while for lean and rich mixtures, laminar flame speeds are lower. Specifically, laminar flame speeds decrease as the mixtures become leaner and richer. This trend is consistently observed in the results of both the ACR55 and Updated HP-Mech mechanisms. However, this trend is reversed at higher temperatures. For instance, regarding the results of the ACR55 mechanism, at a temperature of T=1800K and a pressure of p=200 atm, the laminar flame speed reaches its minimum value around the stoichiometric equivalence ratio (φ=1), while as the mixtures become leaner and richer, laminar flame speeds increase in both N_2 and sCO_2 environments.

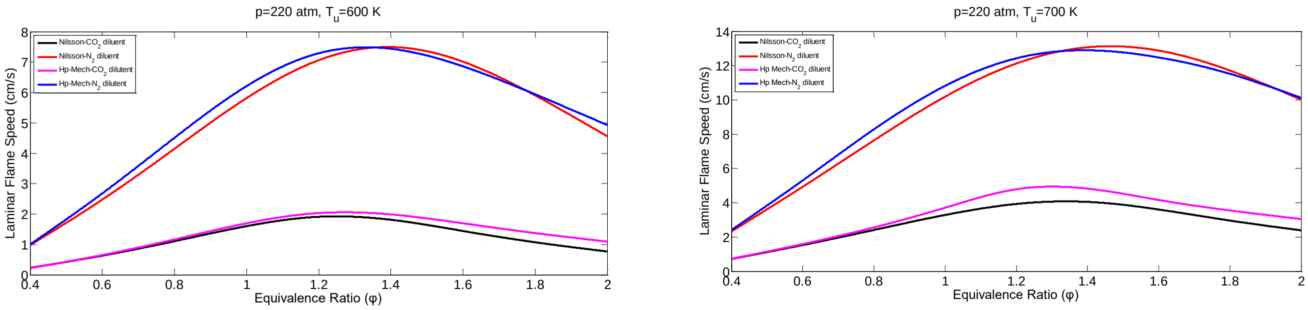

Figure 68. Laminar flame speed versus equivalence ratio for CH_3OH combustion in N_2/CO_2, at (a) P = 200 atm and T_{un} = 600 K (Mixture 1), (b) P = 220 atm and T_{un} = 700 K (Mixture 2).

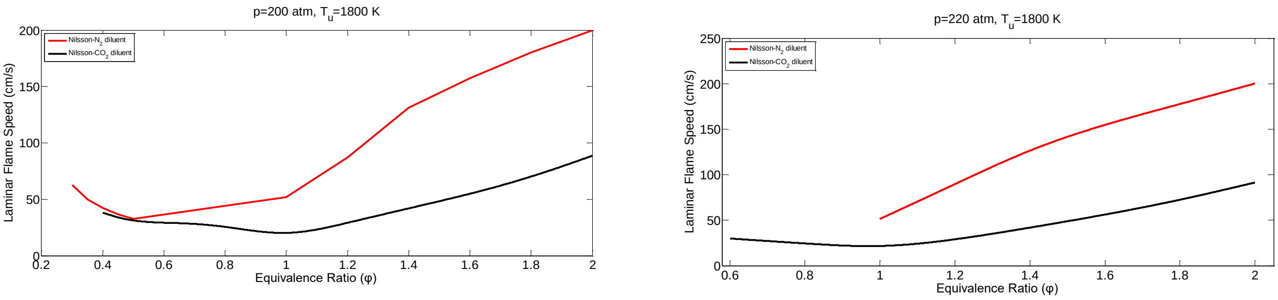

Figure 69. Laminar flame speed versus equivalence ratio for CH_3OH combustion in N_2/CO_2, at (a) P = 200 atm and T_{un} = 1800 K (Mixture 3), (b) P = 220 atm and T_{un} = 1800 K (Mixture 4).

CHAPTER 5: Chemical Analysis

5.1 ROP - Ignition delay time

The effect of N_2 and CO_2 on ignition, which was determined in the previous section, is analyzed here through the Rate Of Production analysis (ROP analysis) for a representative case, in which the effect of those species was shown to be significant. This case concerns conditions φ=0.8, P=220 atm, and T=1700 K. The rate of production analysis showed that, at the time of ignition, the chemistry for the two cases of diluents (N_2 or CO_2) is different. For this reason, the rate of production analysis was carried out at an earlier, appropriately chosen, point in time to explore what led to these differences. The choice of this time is based on the criterion that the difference in the production rates of the compounds is evident, and this is important in relation to the evolution of the phenomenon. In this context, the timing of 0.029 μs was chosen, mainly based on the production rate of hydroxyl radical (OH) and hydrogen radical (H). The increased concentration of these roots demonstrates the pronounced activity of the mixture.

Tables x and y present the normalized and absolute consumption rates, respectively, of the significant, for the consumption of CH_3OH reactions, as identified in the context of this work, for the cases of the mixture of methanol using CO_2 and N_2 as diluent. The normalized value of the rate of production (or consumption) of a chemical compound in an elementary reaction is calculated as the corresponding rate of production (or consumption) divided by the sum of all absolute rates of production (or consumption) of that chemical compound from all elementary reactions. It is evident that the most important reactions contributing to CH_3OH consumption are R50 and R47. In the case of methanol mixture with CO_2 as a diluent, R50 and R47 reactions account for approximately 50% and 30% of CH_3OH consumption respectively. On the other hand, in the case of methanol mixture with N_2 as a diluent, R50 and R47 reactions account for approximately 37% and 35% of CH_3OH consumption respectively. Consequently, in both cases, the dominant radicals for the consumption of CH_3OH are hydroxyl radical (OH) and hydrogen radical (H), with the OH radical being more dominant. Generally, the total absolute rate of CH_3OH consumption at the ignition point for the CH_3OH-CO_2 mixture is $3.27\cdot10^2$ while for the CH_3OH-N_2 mixture is $1.54\cdot10^1$. So, the total absolute rate of CH_3OH consumption is an order of magnitude smaller in the case of the CH_3OH-N_2 mixture at the ignition point compared to the CH_3OH-CO_2 mixture.

The reactions denoted by RXX are as numbered in the Nilsson and Hp Mech mechanisms.

Table 39. Absolute rates of CH_3OH consumption, for CH_3OH mixture (φ=0.8, P=220 atm, and T=1700 K), with CO_2 and N_2 as diluent at the ignition point (τ_{ign} = 0.349 μs and τ_{ign} = 0.467 μs respectively).

Reactions		Absolute rate (moles/cc-s)	
CH_3OH consumption		CO_2 diluent	N_2 diluent
$CH_3OH(+M)=CH_3+OH(+M)$	(R44)	3.53E+00	3.80E-01
$CH_3OH+H=CH_3O+H_2$	(R45)	8.45E+00	5.38E-01
$CH_3OH+H=CH_2OH+H_2$	(R47)	1.04E+02	5.40E+00
$CH_3OH+O=CH_2OH+OH$	(R49)	1.76E+01	3.82E-01
$CH_3OH+OH=CH_2OH+H2O$	(R50)	1.65E+02	5.77E+00
$CH_3OH+HO_2=CH_2OH+H_2O_2$	(R52)	2.84E+01	2.93E+00

Table 40. Normalized rates of CH_3OH consumption, for CH_3OH mixture ($\varphi=0.8$, P=220 atm, and T=1700 K), with CO_2 and N_2 as diluent at the ignition point (τ_{ign} = 0.349 μs and τ_{ign} = 0.467 μs respectively).

Reactions	**Normalized rate**	
CH_3OH consumption	**CO_2 diluent**	**N_2 diluent**
$CH_3OH(+M)=CH_3+OH(+M)$ (R44)	0.011	0.025
$CH_3OH+H=CH_3O+H_2$ (R45)	0.025	0.035
$CH_3OH+H=CH_2OH+H_2$ (R47)	0.312	0.349
$CH_3OH+O=CH_2OH+OH$ (R49)	0.053	0.025
$CH_3OH+OH=CH_2OH+H2O$ (R50)	0.498	0.373
$CH_3OH+HO_2=CH_2OH+H_2O_2$ (R52)	0.085	0.189

Tables 41 and 42 present the absolute and normalized production rates, respectively, of the significant, for the production of OH radicals, reactions, as identified in the context of this work, for the cases of the mixture of methanol using CO_2 and N_2 as diluent. For the case of CH_3OH-CO_2 mixture the most important reactions for the production of OH are R13 and R28 while for the case of CH_3OH- N_2 mixture are R9, R5, R28 and R4. The main reaction that demonstrates a significant transformation of chemistry in the case of CH_3OH- CO_2 mixture is R13. This transformation of chemistry is less pronounced in the case of CH_3OH- N_2 mixture and in particular an order of magnitude smaller. Therefore, it is important to investigate the cause of this difference at an earlier point in time.

Additionally, at the time of ignition, although the total absolute rate of OH production is lower for the CH_3OH-CO_2 mixture, the methanol consumption based on OH is higher compared to the CH_3OH-N_2 mixture. The total absolute rate of OH production for the CH_3OH-CO_2 mixture, is 5.6961E+02 moles/cc-s, while for the CH_3OH-N_2 mixture, is 6.6192E+02 moles/cc-s. However, in earlier moments this is reversed, meaning that the total absolute rate of OH production for the CH_3OH-CO_2 mixture is higher compared to the CH_3OH-N_2 mixture.

Lastly, at the time of ignition, the R50 reaction is not included in the significant consumption reactions of OH in the case of N_2.

$CH_3OH+OH=>CH_2OH+H_2O$ (R50)

Table 41. Absolute production rates for the OH-producing elementary reactions at the ignition point for CH_3OH mixtures with CO_2 and N_2 as diluent ($\varphi=0.8$, P=220 atm, and T=1700 K).

Reactions	**Absolute rate (moles/cc-s)**	
OH production	**CO_2 diluent**	**N_2 diluent**
$H+H_2O=H_2+OH$ (R4)	-	1.19E+02
$H_2+O=H+OH$ (R5)	-	1.28E+02
$O_2+H=O+OH$ (R9)	2.52E+01	1.76E+02
$H_2O_2(+M)=2OH(+M)$ (R13)	3.93E+02	2.70E+01
$CH_2O+O=HCO+OH$ (R18)	-	1.53E+01
$HO_2+H=2OH$ (R28)	9.77E+01	1.33E+02
$CO_2+H=CO+OH$ (R33)	2.10E+01	-
$CH_3OH+O=CH_2OH+OH$ (R49)	1.76E+01	-

Table 42. Normalized production rates for the OH-producing elementary reactions at the ignition point for CH_3OH mixtures with CO_2 and N_2 as diluent (φ=0.8, P=220 atm, and T=1700 K).

Reactions		**Normalized rate**	
OH production		**CO_2 diluent**	**N_2 diluent**
$H+H_2O=H_2+OH$	(R4)	-	0.197
$H_2+O=H+OH$	(R5)	-	0.21
$O_2+H=O+OH$	(R9)	0.044	0.291
$H_2O_2(+M)=2OH(+M)$	(R13)	0.69	0.044
$CH_2O+O=HCO+OH$	(R18)	-	0.025
$HO_2+H=2OH$	(R28)	0.172	0.22
$CO_2+H=CO+OH$	(R33)	0.037	-
$CH_3OH+O=CH_2OH+OH$	(R49)	0.031	-

Tables 43 and 44 present the absolute and normalized production rates, respectively, of the significant, for the production of H radicals, reactions, as identified in the context of this work, for the cases of the mixture of methanol using CO_2 and N_2 as diluent. For the case of CH_3OH-CO_2 mixture the most important reactions for the production of H are R30, R3 and R37 while for the case of CH_3OH- N_2 mixture are R3, R5 and R30.The main reaction that demonstrates a significant transformation of chemistry in the case of CH_3OH- CO_2 mixture is R30. This transformation of chemistry is less pronounced in the case of CH_3OH- N_2 mixture and in particular an order of magnitude smaller. Therefore, it is important to investigate the cause of this difference at an earlier point in time.

Additionally, at the time of ignition, although the total absolute rate of H production is lower for the CH_3OH-CO_2 mixture, the methanol consumption based on the H radical is higher compared to the CH_3OH-N_2 mixture. The total absolute rate of H production for the CH_3OH-CO_2 mixture, is 4.3890E+02 moles/cc-s, while for the CH_3OH-N_2 mixture, is 4.7107E+02moles/cc-s. However, in earlier moments this is reversed, meaning that total absolute rate of H production for the CH_3OH-CO_2 mixture is higher compared to the CH_3OH-N_2 mixture.

Table 43. Absolute production rates for the H-producing elementary reactions at the ignition point for CH_3OH mixtures with CO_2 and N_2 as diluent (φ=0.8, P=220 atm, and T=1700 K).

Reactions		**Absolute rate (moles/cc-s)**	
H production		**CO_2 diluent**	**N_2 diluent**
$H_2+OH=H+H_2O$	(R3)	6.41E+01	3.54E+02
$H_2+O=H+OH$	(R5)	-	1.28E+02
$O+OH=O_2+H$	(R10)	-	1.28E+01
$HCO+M=H+CO+M$	(R30)	3.01E+02	9.39E+01
$CO+OH=CO_2+H$	(R32)	6.02E+00	5.13E+01
$HO_2(+M)=H+O_2(+M)$	(R37)	4.98E+01	2.82E+01
$CH_2OH(+M)=CH_2O+H(+M)$	(R41)	9.41E+00	-
$CH_3O(+M)=CH_2O+H(+M)$	(R42)	5.35E+00	-

Table 44. Normalized production rates for the H-producing elementary reactions at the ignition point for CH_3OH mixture with CO_2 and N_2 as diluent (φ=0.8, P=220 atm, and T=1700 K).

Reactions		**Normalized rate**	
H production		**CO_2 diluent**	**N_2 diluent**
H_2+OH=H+H_2O	(R3)	0.146	0.525
H_2+O=H+OH	(R5)	-	0.189
O+OH=O_2+H	(R10)	-	0.019
HCO+M=H+CO+M	(R30)	0.686	0.139
CO+OH=CO_2+H	(R32)	0.014	0.076
HO_2(+M)=H+O_2(+M)	(R37)	0.114	0.042
CH_2OH(+M)=CH_2O+H(+M)	(R41)	0.021	-
CH_3O(+M)=CH_2O+H(+M)	(R42)	0.012	-

Tables 45 and 46 present the absolute and normalized production rates, respectively, of the significant, for the production of O radicals, reactions, as identified in the context of this work, for the cases of the mixture of methanol using CO_2 and N_2 as diluent.

Table 45. Absolute production rates for the O-producing elementary reactions at the ignition point for CH_3OH mixtures with CO_2 and N_2 as diluent (φ=0.8, P=220 atm, and T=1700 K).

Reactions		**Absolute rate (moles/cc-s)**	
O production		**CO_2 diluent**	**N_2 diluent**
H+OH=H_2+O	(R6)	2.84E-01	9.66E+00
O_2+H=O+OH	(R9)	2.52E+01	1.76E+02

Table 46. Normalized production rates for the OH-producing elementary reactions at the ignition point for CH_3OH mixtures with CO_2 and N_2 as diluent (φ=0.8, P=220 atm, and T=1700 K).

Reactions		**Normalized rate**	
O production		**CO_2 diluent**	**N_2 diluent**
H+OH=H_2+O	(R6)	0.011	0.052
O_2+H=O+OH	(R9)	0.989	0.948

Tables 47 and 48 present the absolute and normalized production rates, respectively, of the significant, for the production of HO_2 radicals, reactions, as identified in the context of this work, for the cases of the mixture of methanol using CO_2 and N_2 as diluent. For the case of CH_3OH- CO_2 mixture the most important reactions for the production of HO_2 are R1 and R36 while for the case of CH_3OH- N_2 mixture is R36.

Table 47. Absolute production rates for the HO_2-producing elementary reactions at the ignition point for CH_3OH mixtures with CO_2 and N_2 as diluent (φ=0.8, P=220 atm, and T=1700 K).

Reactions		**Absolute rate (moles/cc-s)**	
HO_2 production		**CO_2 diluent**	**N_2 diluent**
CH_2OH+O_2=CH_2O+HO_2	(R1)	4.08E+02	1.91E+01
HCO+O_2=CO+HO_2	(R34)	5.22E+01	7.61E+00
H+O_2(+M)=HO_2(+M)	(R36)	1.30E+02	1.81E+02
CH_3O+O_2=CH_2O+HO_2	(R12)	6.36E+00	-

Table 48. Normalized production rates for the HO_2-producing elementary reactions at the ignition point for CH_3OH mixtures with CO_2 and N_2 as diluent (φ=0.8, P=220 atm, and T=1700 K).

Reactions	**Normalized rate**	
HO_2 production	**CO_2 diluent**	**N_2 diluent**
$CH_2OH+O_2=CH_2O+HO_2$ (R1)	0.682	0.091
$HCO+O_2=CO+HO_2$ (R34)	0.087	0.036
$H+O_2(+M)=HO_2(+M)$ (R36)	0.217	0.866
$CH_3O+O_2=CH_2O+HO_2$ (R12)	0.011	-

At the ignition time the absolute consumption rate of CH_2OH for the production of HO_2 is $4.0750 \cdot 10^{2}$ moles/cc-s for the CH_3OH-CO_2 mixture, while for the CH_3OH-N_2 mixture it is $1.9094E \cdot 10^{1}$ moles/cc-s.

$CH_2OH+O_2=>CH_2O+HO_2$ (R1)

As a result, the total production rate of HO_2 is $5.9726 \cdot 10^{2}$ moles/cc-s for the CH_3OH-CO_2 mixture, while for the CH_3OH-N_2 mixture it is $2.0900 \cdot 10^{2}$ moles/cc-s.

The higher production rate of HO_2 leads to a higher total absolute production rate of H_2O_2 for the CH_3OH-CO_2 mixture. The total absolute production rate of H_2O_2 is $1.8300 \cdot 10^{2}$ moles/cc-s for the CH_3OH-CO_2 mixture, while for the CH_3OH-N_2 mixture it is $1.3121E \cdot 10^{-1}$ moles/cc-s.

$2HO_2=>H_2O_2+O_2$ (R26)

The higher production rate of H_2O_2 leads to a higher absolute production rate of OH for the CH_3OH-CO_2 mixture through the reaction R13. However, the total absolute production rate of OH is $5.6961 \cdot 10^{2}$ moles/cc-s for the CH_3OH-CO_2 mixture, while for the CH_3OH-N_2 mixture it is $6.0610 \cdot 10^{2}$ moles/cc-s. Although the total absolute production rate of OH is higher for the CH_3OH-N_2 mixture at the ignition point, the R13 reaction is faster for the CH_3OH-CO_2 mixture, while the R3 reaction, that consumes OH, is faster for the CH_3OH-N_2 mixture.

$H_2O_2(+M)=>2OH(+M)$ (R13)

$H_2+OH=>H+H_2O$ (R3)

At time t=0.029 μs the absolute consumption rate of CO_2 is $1.8289 \cdot 10^{-2}$ moles/cc-s for the CH_3OH-CO_2 mixture, while for the CH_3OH-N_2 mixture it is $4.4864 \cdot 10^{-15}$ moles/cc-s.

$CO_2+H=CO+OH$ (R33)

As a result, the total production rate of CO is $3.0852 \cdot 10^{-2}$ moles/cc-s for the CH_3OH-CO_2 mixture, while for the CH_3OH-N_2 mixture it is $7.6203 \cdot 10^{-3}$ moles/cc-s.

The higher production rate of CO leads to a higher total absolute production rate of HCO for the CH_3OH-CO_2 mixture. The total absolute production rate of HCO is $1.2870 \cdot 10^{-2}$ moles/cc-s for the CH_3OH-CO_2 mixture, while for the CH_3OH-N_2 mixture it is $7.9548 \cdot 10^{-3}$ moles/cc-s.

$H+CO+M=HCO+M$ (R31)

The higher production rate of HCO leads to a higher total absolute production rate for H of the CH_3OH-CO_2 mixture. The total production rate of H is $5.9417 \cdot 10^{-1}$ moles/cc-s for the CH_3OH-CO_2 mixture, while for the CH_3OH-N_2 mixture it is $2.2319 \cdot 10^{-1}$ moles/cc-s.

$HCO+M=H+CO+M$ (R30)

The higher production rate of H leads to a higher total absolute production rate of HO_2 for the CH_3OH-CO_2 mixture. The total production rate of HO_2 is 4.8452 moles/cc-s for the CH_3OH-CO_2 mixture, while for the CH_3OH-N_2 mixture it is 3.9449 moles/cc-s.

$H+O_2(+M)=HO_2(+M)$ (R36)

The higher production rate of HO_2 leads to a higher total absolute production rate of H_2O_2 for the CH_3OH-CO_2 mixture. The total production rate of H_2O_2 is $9.5856 \cdot 10^{-1}$ moles/cc-s for the CH_3OH-CO_2 mixture, while for the CH_3OH-N_2 mixture it is $7.2308 \cdot 10^{-1}$ moles/cc-s.

$2HO_2=H_2O_2+O_2$ (R26)

$CH_3OH+HO_2=CH_3O+H_2O_2$ (R51)

$CH_3OH+HO_2=CH_2OH+H_2O_2$ (R52)

The higher production rate of H_2O_2 leads to a higher total absolute production rate of OH for the CH_3OH-CO_2 mixture. The total production rate of OH is 3.3851 moles/cc-s for the CH_3OH-CO_2 mixture, while for the CH_3OH-N_2 mixture it is 3.0061 moles/cc-s.

$H_2O_2(+M)=>2OH(+M)$ (R13)

Table 49. Absolute production rates for the OH-producing elementary reactions at τ=0.029μs for CH_3OH mixtures with CO_2 and N_2 as diluent (φ=0.8, P=220 atm, and T=1700 K).

Reactions	Absolute rate (moles/cc-s)	
OH production	**CO_2 diluent**	**N_2 diluent**
$O_2+H=O+OH$ (R9)	3.48E-02	-
$H_2O_2(+M)={}_2OH(+M)$ (R13)	9.37E-01	6.10E-01
$CH_3OH+O=CH_2OH+OH$ (R49)	2.36E+00	2.36E+00

Table 50. Normalized production rates for the OH-producing elementary reactions at τ=0.029μs for CH_3OH mixtures with CO_2 and N_2 as diluent (φ=0.8, P=220 atm, and T=1700 K).

Reactions	Normalized rate	
OH production	**CO_2 diluent**	**N_2 diluent**
$O_2+H=O+OH$ (R9)	0.01	-
$H_2O_2(+M)={}_2OH(+M)$ (R13)	0.277	0.203
$CH_3OH+O=CH_2OH+OH$ (R49)	0.697	0.785

Table 51. Absolute production rates for the H-producing elementary reactions at τ=0.029μs for CH_3OH mixtures with CO_2 and N_2 as diluent (φ=0.8, P=220 atm, and T=1700 K).

Reactions	Absolute rate (moles/cc-s)	
H production	**CO_2 diluent**	**N_2 diluent**
$HCO+M=H+CO+M$ (R30)	9.39E-03	4.71E-03
$HO_2(+M)=H+O_2(+M)$ (R37)	3.85E-01	9.57E-02
$CH_2OH(+M)=CH_2O+H(+M)$ (R41)	5.08E-02	3.18E-02
$CH_3O(+M)=CH_2O+H(+M)$ (R42)	1.48E-01	9.05E-02

Table 52. Normalized production rates for the H-producing elementary reactions at τ=0.029μs for CH_3OH mixtures with CO_2 and N_2 as diluent (φ=0.8, P=220 atm, and T=1700 K).

Reactions		**Normalized rate**	
H production		**CO_2 diluent**	**N_2 diluent**
$HCO+M=H+CO+M$	(R30)	0.016	0.021
$HO_2(+M)=H+O_2(+M)$	(R37)	0.649	0.429
$CH_2OH(+M)=CH_2O+H(+M)$	(R41)	0.085	0.143
$CH_3O(+M)=CH_2O+H(+M)$	(R42)	0.249	0.406

Table 53. Absolute production rates for the OH-producing elementary reactions at τ=0.029μs for CH_3OH mixtures with CO_2 and N_2 as diluent (φ=0.8, P=220 atm, and T=1700 K).

Reactions		**Absolute rate (moles/cc-s)**	
O production		**CO_2 diluent**	**N_2 diluent**
$O_2+H=O+OH$	(R9)	3.48E-02	1.87E-02

Table 54. Normalized production rates for the O-producing elementary reactions at τ=0.029μs for CH_3OH mixtures with CO_2 and N_2 as diluent (φ=0.8, P=220 atm, and T=1700 K).

Reactions		**Normalized rate**	
O production		**CO_2 diluent**	**N_2 diluent**
$O_2+H=O+OH$	(R9)	1	1

Table 55. Absolute production rates for the HO_2-producing elementary reactions at τ=0.029μs for CH_3OH mixtures with CO_2 and N_2 as diluent (φ=0.8, P=220 atm, and T=1700 K).

Reactions		**Absolute rate (moles/cc-s)**	
HO_2 production		**CO_2 diluent**	**N_2 diluent**
$CH_2OH+O_2=CH_2O+HO_2$	(R1)	4.40E+00	3.71E+00
$CH_3O+O_2=CH_2O+HO_2$	(R12)	2.02E-01	1.86E-01
$H+O_2(+M)=HO_2(+M)$	(R36)	2.38E-01	4.19E-02

Table 56. Normalized production rates for the HO_2-producing elementary reactions at τ=0.029μs for CH_3OH mixtures with CO_2 and N_2 as diluent (φ=0.8, P=220 atm, and T=1700 K).

Reactions		**Normalized rate**	
HO_2 production		**CO_2 diluent**	**N_2 diluent**
$CH_2OH+O_2=CH_2O+HO_2$	(R1)	0.909	0.942
$CH_3O+O_2=CH_2O+HO_2$	(R12)	0.042	0.047
$H+O_2(+M)=HO_2(+M)$	(R36)	0.049	0.011

Φ=0.5

Tables x and y present the normalized and absolute consumption rates, respectively, of the significant, for the consumption of CH_3OH reactions, as identified in the context of this work, for the cases of the mixture of methanol using CO_2 and N_2 as diluent. It is evident that, the most important reactions contributing to CH_3OH consumption are R50 and R47. In the case of methanol mixture with CO_2 as a diluent, R50 and R47 reactions account for approximately 60% and 25% of CH_3OH consumption respectively. On the other hand, in the case of methanol mixture with N_2 as a diluent, R50 and R47 reactions account for approximately 50% and 35% of CH_3OH consumption respectively. Consequently, in both cases, the dominant radicals for the consumption of CH_3OH are hydroxyl radical (OH) and hydrogen radical (H), with the OH radical being more dominant. Generally, the total absolute rate of CH_3OH consumption at the ignition point for the CH_3OH-CO_2 mixture is $1.58 \cdot 10^2$ while for the CH_3OH-N_2 mixture is $2.17 \cdot 10^2$. So, the total absolute rate of CH_3OH consumption in the case of the CH_3OH-N_2 mixture at the ignition point is a bit higher but of the same order as that of CH_3OH-CO_2 mixture.

Table 57. Absolute rates of CH_3OH consumption, for CH_3OH mixture ($\varphi=0.8$, P=220 atm, and T=1500 K), with CO_2 and N_2 as diluent at the ignition point (τ_{ign} = 1.273 μs and τ_{ign} = 1.227 μs respectively).

Reactions	**Absolute rate (moles/cc-s)**	
CH_3OH consumption	**CO_2 diluent**	**N_2 diluent**
$CH_3OH+H=CH_3O+H_2$ (R45)	2.81E+00	5.68E+00
$CH_3OH+H=CH_2OH+H_2$ (R47)	3.91E+01	7.36E+01
$CH_3OH+O=CH_2OH+OH$ (R49)	6.97E+00	1.42E+01
$CH_3OH+OH=CH_2OH+H_2O$ (R50)	9.46E+01	1.07E+02
$CH_3OH+HO_2=CH_2OH+H_2O_2$ (R52)	1.47E+01	1.58E+01

Table 58. Normalized rates of CH_3OH consumption, for CH_3OH mixture ($\varphi=0.8$, P=220 atm, and T=1500 K), with CO_2 and N_2 as diluent at the ignition point (τ_{ign} = 1.227 μs and τ_{ign} = 1.223 μs respectively).

Reactions	**Normalized rate**	
CH_3OH consumption	**CO_2 diluent**	**N_2 diluent**
$CH_3OH+H=CH_3O+H_2$ (R45)	0.018	0.026
$CH_3OH+H=CH_2OH+H_2$ (R47)	0.244	0.334
$CH_3OH+O=CH_2OH+OH$ (R49)	0.044	0.065
$CH_3OH+OH=CH_2OH+H_2O$ (R50)	0.59	0.487
$CH_3OH+HO_2=CH_2OH+H_2O_2$ (R52)	0.092	0.071

Tables 59 and 60 present the absolute and normalized production rates, respectively, of the significant, for the production of OH radicals, reactions, as identified in the context of this work, for the cases of the mixture of methanol using CO_2 and N_2 as diluent. For both cases the most important reactions for the production of OH are R13 and R28. The main reaction that demonstrates a significant transformation of chemistry in both cases is R13. In the case of CH_3OH- N_2 mixture, this transformation of chemistry is a bit more rapid than in the case of CH_3OH-CO_2 mixture. The total absolute rate of OH production for the CH_3OH-CO_2 mixture, is $3.37 \cdot 10^6$ moles/cc-s, while for the CH_3OH-N_2 mixture, is $4.33 \cdot 10^6$ moles/cc-s.

As a result, at the time of ignition, in the case CH_3OH-N_2 mixture the methanol consumption based on OH is bit higher compared to the CH_3OH-CO_2 mixture.

Table 59. Absolute production rates for the OH-producing elementary reactions at the ignition point for CH_3OH mixtures with CO_2 and N_2 as diluent ($\varphi=0.8$, P=220 atm, and T=1500 K).

Reactions	**Absolute rate (moles/cc-s)**	
OH production	**CO_2 diluent**	**N_2 diluent**
$H+H_2O=H_2+OH$ (R4)	-	4.76E+00
$O_2+H=O+OH$ (R9)	1.021E+01	2.17E+01
$H_2O_2(+M)=2OH(+M)$ (R13)	2.587E+02	2.92E+02
$CH_2O+O=HCO+OH$ (R18)	-	5.24E+00

HO_2+H=2OH (R28)	5.4500E+01	9.51E+01
CO_2+H=CO+OH (R33)	6.7865E+00	-
CH_3OH+O=CH_2OH+OH (R49)	6.9739E+00	1.42E+01

Table 60. Normalized production rates for the OH-producing elementary reactions at the ignition point for CH_3OH mixtures with CO_2 and N_2 as diluent (φ=0.8, P=220 atm, and T=1500 K).

Reactions	**Normalized rate**	
OH production	**CO_2 diluent**	**N_2 diluent**
H+H_2O=H_2+OH (R4)	-	0.011
O_2+H=O+OH (R9)	0.030	0.050
H_2O_2(+M)=2OH(+M) (R13)	0.755	0.669
CH_2O+O=HCO+OH (R18)	-	0.012
HO_2+H=2OH (R28)	0.159	0.218
CO_2+H=CO+OH (R33)	0.020	-
CH_3OH+O=CH_2OH+OH (R49)	0.020	0.033

Tables 61 and 62 present the absolute and normalized production rates, respectively, of the significant, for the production of H radicals, reactions, as identified in the context of this work, for the cases of the mixture of methanol using CO_2 and N_2 as diluent. For both cases the most important reactions for the production of H are R30 and R3. The main reaction that demonstrates a significant transformation of chemistry in both cases is R30. In the case of CH_3OH- N_2 mixture, this transformation of chemistry is a bit more rapid than in the case of CH_3OH-CO_2 mixture. The total absolute rate of H production for the CH_3OH-CO_2 mixture, is $2.23 \cdot 10^6$ moles/cc-s, while for the CH_3OH-N_2 mixture, is $2.36 \cdot 10^6$ moles/cc-s. As a result, at the time of ignition, in the case CH_3OH-N_2 mixture the methanol consumption based on H presents almost double absolute rate compared to the CH_3OH-CO_2 mixture. However, in earlier moments this is reversed, meaning that total absolute rate of H production for the CH_3OH-CO_2 mixture is higher compared to the CH_3OH-N_2 mixture.

Table 61. Absolute production rates for the H-producing elementary reactions at the ignition point for CH_3OH mixtures with CO_2 and N_2 as diluent (φ=0.8, P=220 atm, and T=1500 K).

Reactions	**Absolute rate (moles/cc-s)**	
H production	**CO_2 diluent**	**N_2 diluent**
H_2+OH=H+H_2O (R3)	3.67E+01	6.33E+01
HCO+M=H+CO+M (R30)	1.62E+02	2.09E+02
CO+OH=CO_2+H (R32)	5.84E+00	7.49E+00
HO_2(+M)=H+O_2(+M) (R37)	1.65E+01	1.22E+01
CH_2OH(+M)=CH_2O+H(+M) (R41)	2.86E+00	4.24E+00
CH_3O(+M)=CH_2O+H(+M) (R42)	-	3.23E+00

Table 62. Normalized production rates for the H-producing elementary reactions at the ignition point for CH_3OH mixtures with CO_2 and N_2 as diluent (φ=0.8, P=220 atm, and T=1500 K).

Reactions	**Normalized rate**	
H production	**CO_2 diluent**	**N_2 diluent**
H_2+OH=H+H_2O (R3)	0.162	0.21
HCO+M=H+CO+M (R30)	0.713	0.692
CO+OH=CO_2+H (R32)	0.026	0.025
HO_2(+M)=H+O_2(+M) (R37)	0.073	0.040

$CH_2OH(+M)=CH_2O+H(+M)$ (R41)	0.013	0.014
$CH_3O(+M)=CH_2O+H(+M)$ (R42)	-	0.011

Tables 63 and 64 present the absolute and normalized production rates, respectively, of the significant, for the production of O radicals, reactions, as identified in the context of this work, for the cases of the mixture of methanol using CO_2 and N_2 as diluent.

Table 63. Absolute production rates for the O-producing elementary reactions at the ignition point for CH_3OH mixtures with CO_2 and N_2 as diluent (φ=0.8, P=220 atm, and T=1500 K).

Reactions	**Absolute rate (moles/cc-s)**	
O production	**CO_2 diluent**	**N_2 diluent**
$H+OH=H_2+O$ (R6)	-	2.47E-01
$O_2+H=O+OH$ (R9)	1.02E+01	2.17E+01

Table 64. Normalized production rates for the O-producing elementary reactions at the ignition point for CH_3OH mixtures with CO_2 and N_2 as diluent (φ=0.8, P=220 atm, and T=1500 K).

Reactions	**Normalized rate**	
O production	**CO_2 diluent**	**N_2 diluent**
$H+OH=H_2+O$ (R6)	-	0.011
$O_2+H=O+OH$ (R9)	0.991	0.989

Tables 65 and 66 present the absolute and normalized production rates, respectively, of the significant, for the production of HO_2 radicals, reactions, as identified in the context of this work, for the cases of the mixture of methanol using CO_2 and N_2 as diluent. For both cases the most important reactions for the production of H are R1, R34 and R36.

Table 65. Absolute production rates for the HO_2-producing elementary reactions at the ignition point for CH_3OH mixtures with CO_2 and N_2 as diluent (φ=0.8, P=220 atm, and T=1500 K).

Reactions	**Absolute rate (moles/cc-s)**	
HO_2 production	**CO_2 diluent**	**N_2 diluent**
$CH_2OH+O_2=CH_2O+HO_2$ (R1)	1.98E+02	2.68E+02
$CH_3O+O_2=CH_2O+HO_2$ (R12)	-	4.07E+00
$HCO+O_2=CO+HO_2$ (R34)	3.78E+01	6.31E+01
$H+O_2(+M)=HO_2(+M)$ (R36)	9.31E+01	6.20E+01

Table 66. Normalized production rates for the HO_2-producing elementary reactions at the ignition point for CH_3OH mixtures with CO_2 and N_2 as diluent (φ=0.8, P=220 atm, and T=1500 K).

Reactions	**Normalized rate**	
HO_2 production	**CO_2 diluent**	**N_2 diluent**
$CH_2OH+O_2=CH_2O+HO_2$ (R1)	0.596	0.671
$CH_3O+O_2=CH_2O+HO_2$ (R12)	-	0.010
$HCO+O_2=CO+HO_2$ (R34)	0.114	0.158
$H+O_2(+M)=HO_2(+M)$ (R36)	0.281	0.156

At the ignition time the absolute consumption rate of CH_2OH for the production of HO_2 is $1.9780 \cdot 10^2$ moles/cc-s for the CH_3OH-CO_2 mixture, while for the CH_3OH-N_2 mixture it is $2.6762 \cdot 10^2$ moles/cc-s.

$CH_2OH+O_2 => CH_2O+HO_2$ (R1)

As a result, the total production rate of HO_2 is $3.3186 \cdot 10^2$ moles/cc-s for the CH_3OH-CO_2 mixture, while for the CH_3OH-N_2 mixture it is $3.9879 \cdot 10^2$ moles/cc-s.

The higher production rate of HO_2 leads to a higher total absolute production rate of H_2O_2 for the CH_3OH-N_2 mixture. The total absolute production rate of H_2O_2 is $1.1004 \cdot 10^2$ moles/cc-s for the CH_3OH-CO_2 mixture, while for the CH_3OH-N_2 mixture it is $1.2215 \cdot 10^2$ moles/cc-s.

$2HO_2 => H_2O_2+O_2$ (R26)

The higher production rate of H_2O_2 leads to a higher total absolute production rate of OH for the CH_3OH-N_2 mixture. The total absolute production rate of OH is $3.4277 \cdot 10^2$ moles/cc-s for the CH_3OH-CO_2 mixture, while for the CH_3OH-N_2 mixture it is $4.3588 \cdot 10^2$ moles/cc-s.

$H_2O_2(+M) => 2OH(+M)$ (R13)

The aforementioned path explains why methanol is being consumed with a bit higher rate in the case of CH_3OH-N_2 mixture compared to the CH_3OH-CO_2 mixture.

At time t= 0.378 μs the absolute consumption rate of CH_2OH for the production of HO_2 is 2.3103 moles/cc-s for the CH_3OH-CO_2 mixture, while for the CH_3OH-N_2 mixture it is 2.6197 moles/cc-s.

$CH_2OH+O_2 => CH_2O+HO_2$ (R1)

As a result, the total production rate of HO_2 is $3.3186 \cdot 10^2$ moles/cc-s for the CH_3OH-CO_2 mixture, while for the CH_3OH-N_2 mixture it is $3.9879 \cdot 10^2$ moles/cc-s.

The higher production rate of HO_2 leads to a higher total absolute production rate of H_2O_2 for the CH_3OH-N_2 mixture. The total production rate of H_2O_2 is 1.0658 moles/cc-s for the CH_3OH-CO_2 mixture, while for the CH_3OH-N_2 mixture it is 1.2321 moles/cc-s.

$2HO_2=H_2O_2+O_2$ (R26)

$CH_3OH+HO_2=CH_3O+H_2O_2$ (R51)

$CH_3OH+HO_2=CH_2OH+H_2O_2$ (R52)

The higher production rate of H_2O_2 leads to a higher total absolute production rate of OH for the CH_3OH-CO_2 mixture. The total production rate of OH is 1.318 moles/cc-s for the CH_3OH-CO_2 mixture, while for the CH_3OH-N_2 mixture it is 1.4973 moles/cc-s.

$H_2O_2(+M) => 2OH(+M)$ (R13)

Table 67. Absolute production rates for the OH-producing elementary reactions at τ=0.37831μs for CH_3OH mixtures with CO_2 and N_2 as diluent (φ=0.8, P=220 atm, and T=1500 K).

Reactions		**Absolute rate (moles/cc-s)**	
OH production		**CO_2 diluent**	**N_2 diluent**
$H_2O_2(+M) => 2OH(+M)$	(R13)	1.22E+00	1.40E+00

CH_3OH(+M)=>CH3+OH(+M) (R44)	7.91E-02	7.92E-02

Table 68. Normalized production rates for the OH-producing elementary reactions at $\tau=0.37831\mu s$ for CH_3OH mixtures with CO_2 and N_2 as diluent ($\varphi=0.8$, P=220 atm, and T=1500 K).

Reactions	Normalized rate	
OH production	**CO_2 diluent**	**N_2 diluent**
H_2O_2(+M)=>2OH(+M) (R13)	0.925	0.936
CH_3OH(+M)=>CH_3+OH(+M) (R44)	0.060	0.053

Table 69. Absolute production rates for the H-producing elementary reactions at $\tau=0.37831\mu s$ for CH_3OH mixtures with CO_2 and N_2 as diluent ($\varphi=0.8$, P=220 atm, and T=1500 K).

Reactions	Absolute rate (moles/cc-s)	
H production	**CO_2 diluent**	**N_2 diluent**
HCO+M=>H+CO+M (R30)	1.13E-02	1.12E-02
HO_2(+M)=>H+O_2(+M) (R37)	1.42E-01	5.46E-02
CH2OH(+M)=>CH2O+H(+M) (R41)	1.07E-02	9.10E-03
CH3O(+M)=>CH2O+H(+M) (R42)	4.54E-02	3.97E-02

Table 70. Normalized production rates for the H-producing elementary reactions at $\tau=0.37831\mu s$ for CH_3OH mixtures with CO_2 and N_2 as diluent ($\varphi=0.8$, P=220 atm, and T=1500 K).

Reactions	Normalized rate	
H production	**CO_2 diluent**	**N_2 diluent**
HCO+M=>H+CO+M (R30)	0.054	0.097
HO_2(+M)=>H+O_2(+M) (R37)	0.677	0.475
CH2OH(+M)=>CH2O+H(+M) (R41)	0.051	0.079
CH3O(+M)=>CH2O+H(+M) (R42)	0.217	0.346

Table 71. Absolute production rates for the OH-producing elementary reactions at $\tau=0.37831\mu s$ for CH_3OH mixtures with CO_2 and N_2 as diluent ($\varphi=0.8$, P=220 atm, and T=1500 K).

Reactions	Absolute rate (moles/cc-s)	
O production	**CO_2 diluent**	**N_2 diluent**
O_2+H=>O+OH (R9)	7.98E-03	7.42E-03

Table 72. Normalized production rates for the O-producing elementary reactions at $\tau=0.37831\mu s$ for CH_3OH mixtures with CO_2 and N_2 as diluent ($\varphi=0.8$, P=220 atm, and T=1500 K).

Reactions	Normalized rate	
O production	**CO_2 diluent**	**N_2 diluent**
O_2+H=>O+OH (R9)	1	1

Table 73. Absolute production rates for the HO_2-producing elementary reactions at $\tau=0.37831\mu s$ for CH_3OH mixtures with CO_2 and N_2 as diluent ($\varphi=0.8$, P=220 atm, and T=1500 K).

Reactions	Absolute rate (moles/cc-s)	
HO_2 production	**CO_2 diluent**	**N_2 diluent**
CH_2OH+O_2=>CH2O+HO_2 (R1)	2.31E+00	2.62E+00
CH_3O+O_2=>CH_2O+HO_2 (R12)	4.56E-02	5.75E-02

$H+O_2(+M)=>HO_2(+M)$ (R36)	1.26E-01	3.94E-02

Table 74. Normalized production rates for the HO_2-producing elementary reactions at τ=0.37831μs for CH_3OH mixtures with CO_2 and N_2 as diluent (φ=0.8, P=220 atm, and T=1500 K).

Reactions	Normalized rate	
HO_2 production	**CO_2 diluent**	**N_2 diluent**
$CH_2OH+O_2=>CH_2O+HO_2$ (R1)	0.928	0.960
$CH_3O+O_2=>CH_2O+HO_2$ (R12)	0.018	0.021
$H+O_2(+M)=>HO_2(+M)$ (R36)	0.051	0.014

5.2 ROP- Concentration Profiles

The effect of N_2 and CO_2 on concentration profiles, which was determined in the previous section, is analyzed here through the Rate Of Production analysis (ROP analysis) for two representative cases, in which the effect of those species was shown to be significant. These cases concern conditions φ=0.5 p=220 bar, T=1500K and φ=2 p=220 bar T=1500K. Particularly, in both cases the concentration profile of CO_2 is being investigated. In the first case, the production of CO_2 is higher in the CH_3OH- N_2 mixture, while in the second case the CO_2 is being consumed in the CH_3OH- CO_2 mixture. The tables below present the normalized and absolute consumption rates, respectively, of the significant, for the consumption of CH_3OH reactions, as identified in the context of this work, for the cases of the mixture of methanol using CO_2 and N_2 as diluent. It is evident that, the most important reactions contributing to CH_3OH consumption are R49 and R50. In both CH_3OH mixtures, with CO_2 and N_2 as a diluent, R49 and R50 reactions account for approximately 65% and 30% of CH_3OH consumption respectively. In addition, in both cases, the dominant radicals for the consumption of CH_3OH are oxygen radical (O) and hydroxyl radical (OH), with the O radical being more dominant. Generally, the total absolute rate of CH_3OH consumption at τ_{end} for both mixtures is $1.5299 \cdot 10^{-4}$ moles/cc-s. So, the effect of N_2 and CO_2 on CH_3OH concentration profile is the same.

Table 75. Absolute rates of CH_3OH consumption, for CH_3OH mixture (φ=0.5, P=220 bar, and T=1500 K), with CO_2 and N_2 as diluent at the end time, τ_{end} = 40s.

Reactions		**Absolute rate (moles/cc-s)**	
CH_3OH consumption		**CO_2 diluent**	**N_2 diluent**
$CH_3OH(+M)=CH_3+OH(+M)$	(R44)	1.96E-06	1.94E-06
$CH_3OH+O=CH_3O+OH$	(R48)	6.65E-06	6.67E-06
$CH_3OH+O=CH_2OH+OH$	(R49)	1.00E-04	1.01E-04
$CH_3OH+OH=CH_2OH+H_2O$	(R50)	4.32E-05	4.30E-05

Table 76. Normalized rates of CH_3OH consumption, for CH_3OH mixture (φ=0.5, P=220 bar, and T=1500 K), with CO_2 and N_2 as diluent at the end time, τ_{end} = 40s.

Reactions		**Normalized rate**	
CH_3OH consumption		**CO_2 diluent**	**N_2 diluent**
$CH_3OH(+M)=CH_3+OH(+M)$	(R44)	0.013	0.013
$CH_3OH+O=CH_3O+OH$	(R48)	0.043	0.044
$CH_3OH+O=CH_2OH+OH$	(R49)	0.656	0.658
$CH_3OH+OH=CH_2OH+H_2O$	(R50)	0.282	0.281

Tables 77 and 78 present the absolute and normalized production rates, respectively, of the significant, for the production of OH radicals, reactions, as identified in the context of this work, for the cases of the mixture of methanol using CO_2 and N_2 as diluent. For the case of CH_3OH-CO_2 mixture the most important reactions for the production of OH are R9, R13, R33, R39 and R49, while for the case of CH_3OH- N_2 mixture are R9, R13, R39 and R49. A main reaction that demonstrates a significant transformation of chemistry in the case of CH_3OH- CO_2 mixture is R33, which is not included in the significant production reactions of OH in the case of CH_3OH-N_2 mixture. The total absolute rate of OH production for the CH_3OH-CO_2 mixture, is $9.4135 \cdot 10^{-4}$ moles/cc-s, while for the CH_3OH-N_2 mixture, is $8.0121 \cdot 10^{-4}$ moles/cc-s.

Table 77. Absolute production rates for the OH-producing elementary reactions at τ_{end} =40s for CH_3OH mixture (φ=0.5, P=220 bar, and T=1500 K), with CO_2 and N_2 as diluent.

Reactions		**Absolute rate (moles/cc-s)**	
OH production		**CO_2 diluent**	**N_2 diluent**
$H+H_2O=H_2+OH$	(R4)	7.80E-05	7.88E-05
$H_2+O=H+OH$	(R5)	1.59E-05	1.61E-05
$O_2+H=O+OH$	(R9)	2.56E-04	2.58E-04
$H_2O_2(+M)=2OH(+M)$	(R13)	1.48E-04	1.47E-04
$CH_2O+O=HCO+OH$	(R18)	5.32E-05	5.35E-05
$CO_2+H=CO+OH$	(R33)	1.49E-04	-
$H_2O+O2=OH+HO_2$	(R39)	1.31E-04	1.31E-04
$CH_3OH+O=CH_2OH+OH$	(R49)	1.00E-04	1.01E-04

Table 78. Normalized production rates for the OH-producing elementary reactions at τ_{end} =40s for CH_3OH mixture (φ=0.5, P=220 bar, and T=1500 K), with CO_2 and N_2 as diluent.

Reactions		**Normalized rate**	
OH production		**CO_2 diluent**	**N_2 diluent**
$H+H_2O=H_2+OH$	(R4)	0.083	0.098
$H_2+O=H+OH$	(R5)	0.017	0.02
$O_2+H=O+OH$	(R9)	0.271	0.322
$H_2O_2(+M)=2OH(+M)$	(R13)	0.157	0.183
$CH_2O+O=HCO+OH$	(R18)	0.057	0.067
$CO_2+H=CO+OH$	(R33)	0.158	-
$H_2O+O_2=OH+HO_2$	(R39)	0.139	0.163
$CH_3OH+O=CH_2OH+OH$	(R49)	0.107	0.126

Tables 79 and 80 present the absolute and normalized production rates, respectively, of the significant, for the production of H radicals, reactions, as identified in the context of this work, for the cases of the mixture of methanol using CO_2 and N_2 as diluent. For both CH_3OH mixtures the most important reaction for the production of H is R37. The total absolute rate of H production for the CH_3OH-CO_2 mixture, is $5.2161 \cdot 10^{-3}$ moles/cc-s, while for the CH_3OH-N_2 mixture, is $2.6535 \cdot 10^{-3}$ moles/cc-s.

Table 79. Absolute production rates for the H-producing elementary reactions at τ_{end} =40s for CH_3OH mixture (φ=0.5, P=220 bar, and T=1500 K), with CO_2 and N_2 as diluent.

Reactions		Absolute rate (moles/cc-s)	
H production		CO_2 diluent	N_2 diluent
$H_2+OH=H+H_2O$	(R3)	6.26E-05	6.31E-05
$O+OH=O_2+H$	(R10)	7.95E-05	8.11E-05
HCO+M=H+CO+M	(R30)	1.18E-04	1.04E-04
$CO+OH=CO_2+H$	(R32)	3.01E-04	1.59E-04
$HO_2(+M)=H+O_2(+M)$	(R37)	4.63E-03	2.22E-03

Table 80. Normalized production rates for the H-producing elementary reactions at τ_{end} =40s for CH_3OH mixture (φ=0.5, P=220 bar, and T=1500 K), with CO_2 and N_2 as diluent.

Reactions		Normalized rate	
H production		CO_2 diluent	N_2 diluent
$H_2+OH=H+H_2O$	(R3)	0.012	0.024
$O+OH=O_2+H$	(R10)	0.015	0.031
HCO+M=H+CO+M	(R30)	0.023	0.039
$CO+OH=CO_2+H$	(R32)	0.058	0.06
$HO_2(+M)=H+O_2(+M)$	(R37)	0.888	0.838

Tables 81 and 82 present the absolute and normalized production rates, respectively, of the significant, for the production of O radicals, reactions, as identified in the context of this work, for the cases of the mixture of methanol using CO_2 and N_2 as diluent.

Table 81. Absolute production rates for the O-producing elementary reactions at τ_{end} =40s for CH_3OH mixture (φ=0.5, P=220 bar, and T=1500 K), with CO_2 and N_2 as diluent.

Reactions		Absolute rate (moles/cc-s)	
O production		CO_2 diluent	N_2 diluent
$O_2+H=O+OH$	(R9)	2.56E-04	2.58E-04

Table 82. Normalized production rates for the O -producing elementary reactions at τ_{end} =40s for CH_3OH mixture (φ=0.5, P=220 bar, and T=1500 K), with CO_2 and N_2 as diluent.

Reactions		Normalized rate	
O production		CO_2 diluent	N_2 diluent
$O_2+H=O+OH$	(R9)	1	1

Tables 83 and 84 present the absolute and normalized production rates, respectively, of the significant, for the production of HO_2 radicals, reactions, as identified in the context of this work, for the cases of the mixture of methanol using CO_2 and N_2 as diluent. For both cases the most important reaction for the production of HO_2 is R36.

Table 83. Absolute production rates for the HO_2-producing elementary reactions at τ_{end} =40s for CH_3OH mixture (φ=0.5, P=220 bar, and T=1500 K), with CO_2 and N_2 as diluent.

Reactions	Absolute rate (moles/cc-s)	
HO_2 production	CO_2 diluent	N_2 diluent

$CH_2OH+O_2=CH_2O+HO_2$ (R1)	1.47E-04	1.47E-04
$HCO+O_2=CO+HO_2$ (R34)	-	4.91E-05
$H+O_2(+M)=HO_2(+M)$ (R36)	4.73E-03	2.31E-03
$H_2O+O_2=OH+HO_2$ (R39)	1.31E-04	1.31E-04

Table 84. Normalized production rates for the HO_2 -producing elementary reactions at τ_{end} =40s for CH_3OH mixture (φ=0.5, P=220 bar, and T=1500 K), with CO_2 and N_2 as diluent.

Reactions	**Normalized rate**	
HO_2 production	**CO_2 diluent**	**N_2 diluent**
$CH_2OH+O_2=CH_2O+HO_2$ (R1)	0.029	0.056
$HCO+O_2=CO+HO_2$ (R34)	-	0.019
$H+O_2(+M)=HO_2(+M)$ (R36)	0.938	0.875
$H_2O+O_2=OH+HO_2$ (R39)	0.026	0.049

At time τ_{end} =40s the absolute total production rate of CO_2 is $3.0081\cdot10^{-4}$ moles/cc-s for the CH_3OH-CO_2 mixture, while for the CH_3OH-N_2 mixture it is $1.5887\cdot10^{-4}$ moles/cc-s.

$CO_2+H=CO+OH$ (R32)

However, at the same time, the total consumption rate of CO_2 through the reaction R33 is $1.4864\cdot10^{-4}$ moles/cc-s for the CH_3OH-CO_2 mixture, while for the CH_3OH-N_2 mixture it is $6.3261\cdot10^{-6}$ moles/cc-s. Consequently, the main reaction that demonstrates a significant transformation of chemistry in the case of CH_3OH- CO_2 mixture is R33. This transformation of chemistry is less pronounced in the case of CH_3OH- N_2 mixture and that is what causes the difference in the concentration profile of CO_2 between the two mixtures.

$CO_2+H=>CO+OH$ (R33)

Φ=2

In the case of methanol mixture with CO_2 as a diluent, R50 and R47 reactions account for approximately 68% and 23% of CH_3OH consumption respectively. On the other hand, in the case of methanol mixture with N_2 as a diluent, R47 reaction accounts for approximately 90% of CH_3OH consumption. Consequently, in both cases, the most dominant radical for the consumption of CH_3OH is the hydrogen radical (H), with the OH radical being important but yet less dominant in the case of CH_3OH-CO_2 mixture. Generally, the total absolute rate of CH_3OH consumption for the CH_3OH-CO_2 mixture is $3.2230\cdot10^{-4}$ while for the CH_3OH-N_2 mixture is $3.2392\cdot1\text{-}4^{1}$. So, the total absolute rate of CH_3OH consumption is an order of magnitude smaller in the case of the CH_3OH-N_2 mixture at the ignition point compared to the CH_3OH-CO_2 mixture. So, the effect of N_2 and CO_2 on CH_3OH concentration profile is the same.

Table 85. Absolute rates of CH_3OH consumption, for CH_3OH mixture (φ=2, P=220 bar, and T=1500 K), with CO_2 and N_2 as diluent at the end time, τ_{end} = 40s.

Reactions	**Absolute rate (moles/cc-s)**	
CH_3OH consumption	**CO_2 diluent**	**N_2 diluent**
$CH_3OH(+M)=CH_3+OH(+M)$ (R44)	1.08E-05	-
$CH_3OH+H=CH_3O+H_2$ (R45)	1.36E-05	1.84E-05
$CH_3OH+H=CH_2OH+H_2$ (R47)	2.20E-04	2.96E-04
$CH_3OH+OH=CH_2OH+H_2O$ (R50)	7.42E-05	6.17E-06

Table 86. Normalized rates of CH_3OH consumption, for CH_3OH mixture (φ=2, P=220 bar, and T=1500 K), with CO_2 and N_2 as diluent at the end time, τ_{end} = 40s.

Reactions		Normalized rate	
CH_3OH consumption		**CO_2 diluent**	**N_2 diluent**
$CH_3OH(+M)=CH_3+OH(+M)$	(R44)	0.034	-
$CH_3OH+H=CH_3O+H_2$	(R45)	0.042	0.057
$CH_3OH+H=CH_2OH+H_2$	(R47)	0.682	0.913
$CH_3OH+OH=CH_2OH+H_2O$	(R50)	0.23	0.019

Tables 87 and 88 present the absolute and normalized production rates, respectively, of the significant, for the production of OH radicals, reactions, as identified in the context of this work, for the cases of the mixture of methanol using CO_2 and N_2 as diluent. For the case of CH_3OH-CO_2 mixture the most important reactions for the production of OH are R4 and R33, while for the case of CH_3OH- N_2 mixture is R4. A main reaction that demonstrates a significant transformation of chemistry in the case of CH_3OH- CO_2 mixture is R33, which is much less intense in the case of CH_3OH- N_2 mixture. The total absolute rate of OH production for the CH_3OH-CO_2 mixture, is $1.2056 \cdot 10^{-1}$. moles/cc-s, while for the CH_3OH-N_2 mixture, is $2.2351 \cdot 10^{-1}$ moles/cc-s.

Table 87. Absolute production rates for the OH-producing elementary reactions at τ_{end} =40s for CH_3OH mixture (φ=2, P=220 bar, and T=1500 K), with CO_2 and N_2 as diluent.

Reactions		Absolute rate (moles/cc-s)	
OH production		**CO_2 diluent**	**N_2 diluent**
$H+H_2O=H_2+OH$	(R4)	6.66E-02	2.15E-01
$CO_2+H=CO+OH$	(R33)	5.35E-02	8.37E-03

Table 88. Normalized production rates for the OH-producing elementary reactions at τ_{end} =40s for CH_3OH mixture (φ=2, P=220 bar, and T=1500 K), with CO_2 and N_2 as diluent.

Reactions		Normalized rate	
OH production		**CO_2 diluent**	**N_2 diluent**
$H+H_2O=H_2+OH$	(R4)	0.553	0.96
$CO_2+H=CO+OH$	(R33)	0.443	0.037

Tables 89 and 90 present the absolute and normalized production rates, respectively, of the significant, for the production of H radicals, reactions, as identified in the context of this work, for the cases of the mixture of methanol using CO_2 and N_2 as diluent. For the case of CH_3OH-CO_2 mixture the most important reactions for the production of H are R3, R30 and R32 while for the case of CH_3OH- N_2 mixture are R3 and R30. The total absolute rate of H production for the CH_3OH-CO_2 mixture, is $2.7312 \cdot 10^{-1}$ moles/cc-s, while for the CH_3OH-N_2 mixture, is $4.6586 \cdot 10^{-1}$ moles/cc-s.

Table 89 Absolute production rates for the H-producing elementary reactions at τ_{end} =40s for CH_3OH mixture (φ=2, P=220 bar, and T=1500 K), with CO_2 and N_2 as diluent.

Reactions		**Absolute rate (moles/cc-s)**	
H production		**CO_2 diluent**	**N_2 diluent**
H_2+OH=H+H_2O	(R3)	6.69E-02	2.15E-01
HCO+M=H+CO+M	(R30)	1.51E-01	2.42E-01
CO+OH=CO_2+H	(R32)	5.33E-02	8.47E-03

Table 90. Normalized production rates for the H-producing elementary reactions at τ_{end} =40s for CH_3OH mixture (φ=2, P=220 bar, and T=1500 K), with CO_2 and N_2 as diluent.

Reactions		**Normalized rate**	
H production		**CO_2 diluent**	**N_2 diluent**
H_2+OH=H+H_2O	(R3)	0.245	0.461
HCO+M=H+CO+M	(R30)	0.554	0.519
CO+OH=CO_2+H	(R32)	0.195	0.018

Tables 91 and 92 present the absolute and normalized production rates, respectively, of the significant, for the production of O radicals, reactions, as identified in the context of this work, for the cases of the mixture of methanol using CO_2 and N_2 as diluent. For both cases the most important reaction for the production of O radical is R9. The total absolute rate of O production for the CH_3OH-CO_2 mixture, is $6.9741 \cdot 10^{-5}$ moles/cc-s, while for the CH_3OH-N_2 mixture, is $3.8448 \cdot 10^{-5}$ moles/cc-s.

Table 91. Absolute production rates for the O-producing elementary reactions at τ_{end} =40s for CH_3OH mixture (φ=2, P=220 bar, and T=1500 K), with CO_2 and N_2 as diluent.

Reactions		**Absolute rate (moles/cc-s)**	
O production		**CO_2 diluent**	**N_2 diluent**
H+OH=H_2+O	(R6)	2.56E-06	4.11E-06
O_2+H=O+OH	(R9)	6.72E-05	3.43E-05

Table 92. Normalized production rates for the O-producing elementary reactions at τ_{end} =40s for CH_3OH mixture (φ=2, P=220 bar, and T=1500 K), with CO_2 and N_2 as diluent.

Reactions		**Normalized rate**	
O production		**CO_2 diluent**	**N_2 diluent**
H+OH=H_2+O	(R6)	0.037	0.107
O_2+H=O+OH	(R9)	0.963	0.893

Tables 93 and 94 present the absolute and normalized production rates, respectively, of the significant, for the production of HO_2 radicals, reactions, as identified in the context of this work, for the cases of the mixture of methanol using CO_2 and N_2 as diluent. For both cases the most important reaction for the production of HO_2 is R36.

Table 93. Absolute production rates for the HO_2-producing elementary reactions at τ_{end} =40s for CH_3OH mixture (φ=2, P=220 bar, and T=1500 K), with CO_2 and N_2 as diluent.

Reactions		**Absolute rate (moles/cc-s)**	
HO_2 production		**CO_2 diluent**	**N_2 diluent**
$CH_2OH+O_2=CH_2O+HO_2$	(R1)	2.00E-05	-
$HCO+O_2=CO+HO_2$	(R34)	2.45E-05	6.32E-06
$H+O_2(+M)=HO_2(+M)$	(R36)	1.34E-03	3.40E-04

Table 94. Normalized production rates for the HO_2-producing elementary reactions at τ_{end} =40s for CH_3OH mixture (φ=2, P=220 bar, and T=1500 K), with CO_2 and N_2 as diluent.

Reactions		**Normalized rate**	
HO_2 production		**CO_2 diluent**	**N_2 diluent**
$CH_2OH+O_2=CH_2O+HO_2$	(R1)	0.014	-
$HCO+O_2=CO+HO_2$	(R34)	0.018	0.018
$H+O_2(+M)=HO_2(+M)$	(R36)	0.967	0.972

At time τ_{end} =40s the absolute total production rate of CO_2 is $5.3320 \cdot 10^{-2}$ moles/cc-s for the CH_3OH-CO_2 mixture, while for the CH_3OH-N_2 mixture it is $8.4692 \cdot 10^{-3}$ moles/cc-s.

$CO_2+H=CO+OH$ (R32)

However, at the same time, the total consumption rate of CO_2 is $5.3320 \cdot 10^{-2}$ moles/cc-s for the CH_3OH-CO_2 mixture, while for the CH_3OH-N_2 mixture it is $8.4692 \cdot 10^{-3}$ moles/cc-s. As a result, the net production rate of CO_2 is $-1.2973 \cdot 10^{-4}$ for the CH_3OH-CO_2 mixture, while for the CH_3OH-N_2 mixture it is $9.4305 \cdot 10^{-5}$ moles/cc-s.

$CO_2+H=>CO+OH$ (R33)

Consequently, the main reaction that demonstrates a significant transformation of chemistry in the case of CH_3OH- CO_2 mixture is R33. This transformation of chemistry is less pronounced in the case of CH_3OH- N_2 mixture and that is what causes the difference in the concentration profile of CO_2 between the two mixtures.

5.3 ROP - Laminar Flame Speed

The effect of N_2 and CO_2 on laminar flame speed, which was determined in the previous section, is analyzed here through the Rate Of Production analysis (ROP analysis) for two representative cases, in which the effect of those species was shown to be significant. These cases concern conditions $\varphi=0.5$, p=220 atm, $T_{un}=700$ K and $\varphi=0.5$, p=200 atm, $T_{un}=1800$K. In the first case, the laminar flame speed is higher in the CH_3OH- N_2 mixture, while in the second case the laminar flame speed is almost the same for both mixtures.

The figures below present the absolute consumption rates of the significant, for the consumption of CH_3OH reactions, as identified in the context of this work, for the cases of the mixture of methanol using N_2 and CO_2 as diluent at conditions $\varphi=0.5$, p=220 atm, $T_{un}=700$ K. It is evident that, in both cases, the dominant radical for the consumption of CH_3OH is the hydroxyl radical (OH), as the most important reaction contributing to CH_3OH consumption is the following:

$CH_3OH + OH = CH_2OH + H_2O$

The total absolute rate of CH_3OH consumption is an order of magnitude smaller in the case of the CH_3OH-CO_2 mixture compared to the CH_3OH-N_2 mixture.

Figure 70. Absolute rates of CH_3OH consumption, for (a) CH_3OH - N_2 mixture, (b) CH_3OH - CO_2 mixture ($\varphi=0.5$, P=220 atm, and T=700 K), at axial position x=0.1cm.

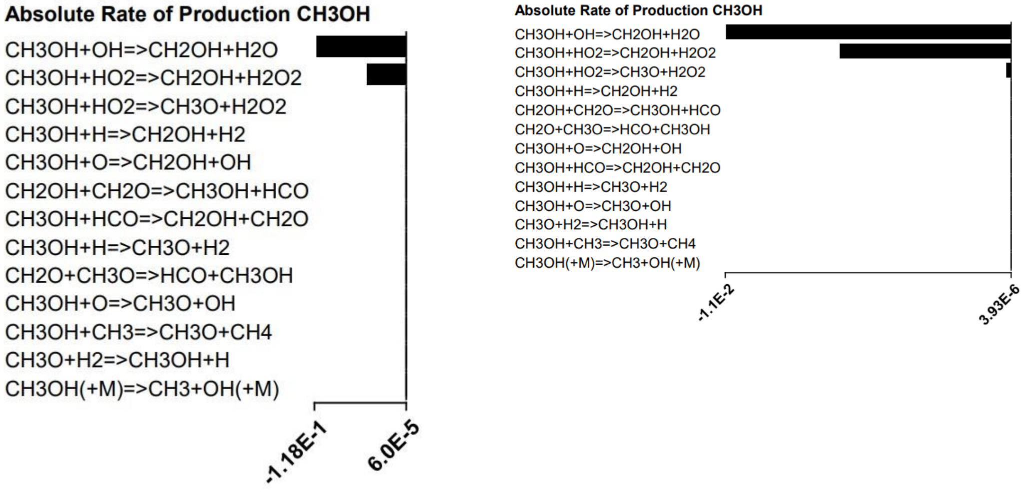

Figure 71 presents the absolute production rates of the significant, for the production of OH radicals, reactions, as identified in the context of this work, for the cases of the mixture of methanol using CO_2 and N_2 as diluent. In both cases, the most important reaction contributing to OH production is the following:

$H_2O_2 (+M) = 2OH (+M)$

The absolute rate of OH production of the above reaction equals $2.18\cdot 10^{-1}$ moles/cc-s. in the case of the CH_3OH-N_2 mixture, while in the CH_3OH-CO_2 mixture it equals $1.98\cdot 10^{-2}$ moles/cc-s.

The higher rate of OH production in the CH_3OH – N_2 mixture is related to the higher production rate of H_2O_2, which is produced mainly through the following reactions:

$CH_3OH + HO_2 = CH_2OH + H_2O_2$

$2HO_2 = H_2O_2 + O_2$

$CH_2O + HO_2 = HCO + H_2O_2$

The total absolute rate of H_2O_2 production equals $1.17\cdot 10^{-1}$ moles/cc-s in the case of the CH_3OH-N_2 mixture and is an order of magnitude higher than the respective rate in the CH_3OH-CO_2 mixture, which equals $1.53\cdot 10^{-2}$ moles/cc-s.

The higher rate of H_2O_2 production in the CH_3OH – N_2 mixture is related to the higher production rate of HO_2, which is produced mainly through the following reactions:

$CH_2OH + O_2 = CH_2O + HO_2$

$HCO + O_2 = CO + HO_2$

The total absolute rate of HO_2 production equals $2.79\cdot 10^{-1}$ moles/cc-s in the case of the CH_3OH-N_2 mixture and is an order of magnitude higher than the respective rate in the CH_3OH-CO_2 mixture, which equals $2.84\cdot 10^{-2}$ moles/cc-s.

Figure 71. Absolute production rates for the OH-producing elementary reactions for (a) CH_3OH - N_2 mixture, (b) CH_3OH - CO_2 mixture (φ=0.5, P=220 atm, and T=700 K), at axial position x=0.1cm.

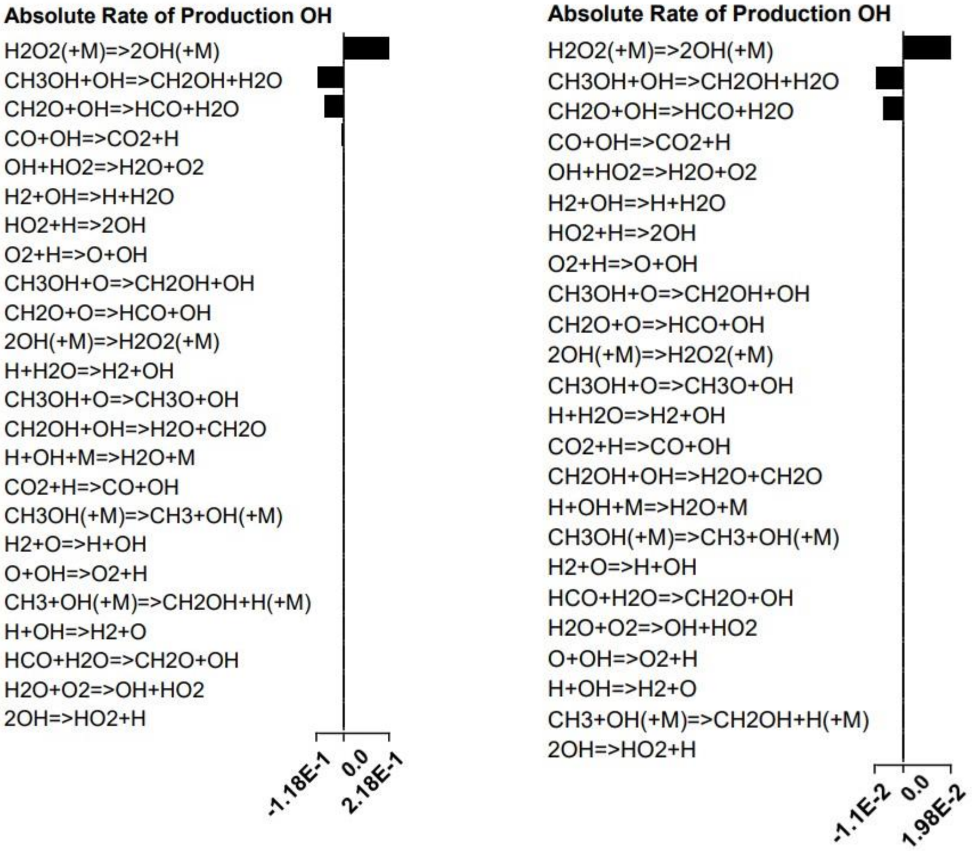

Figure 72 presents the absolute production rates of the significant, for the production of H radicals, reactions, as identified in the context of this work, for the cases of the mixture of methanol using N_2 and CO_2 as diluent. For both CH_3OH mixtures the most important reactions for the production of H are the following:

$HCO + M = H + CO + M$

$CO + OH = CO_2 + H$

Figure 72. Absolute production rates for the H-producing elementary reactions for (a) (a) CH_3OH - N_2 mixture, (b) CH_3OH - CO_2 mixture (φ=0.5, P=220 atm, and T=700 K), at axial position x=0.1cm.

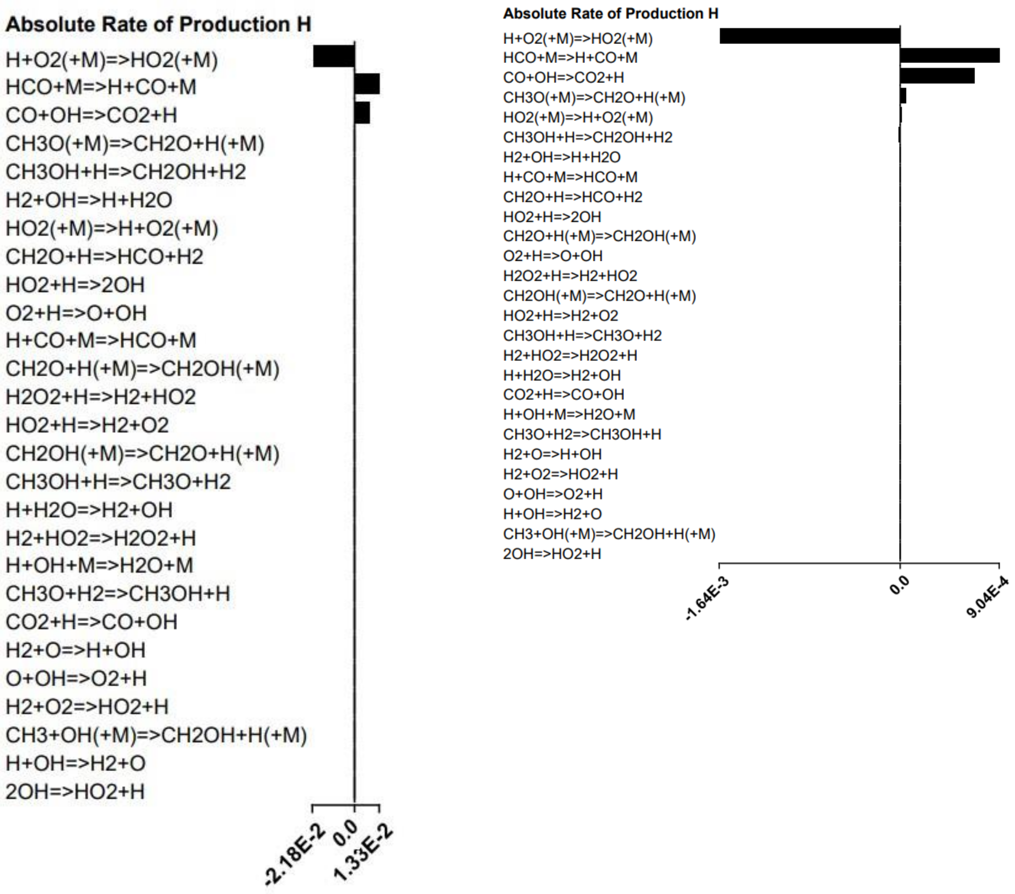

Figure 73 presents the absolute production rates of the significant for the production of O radicals, reactions, as identified in the context of this work, for the cases of the mixture of methanol using N_2 and CO_2 as diluent.

Figure 73. Absolute production rates for the O-producing elementary reactions for (a) CH_3OH - N_2 mixture, (b) CH_3OH - CO_2 mixture (φ=0.5, P=220 atm, and T=700 K), at axial position x=0.1cm.

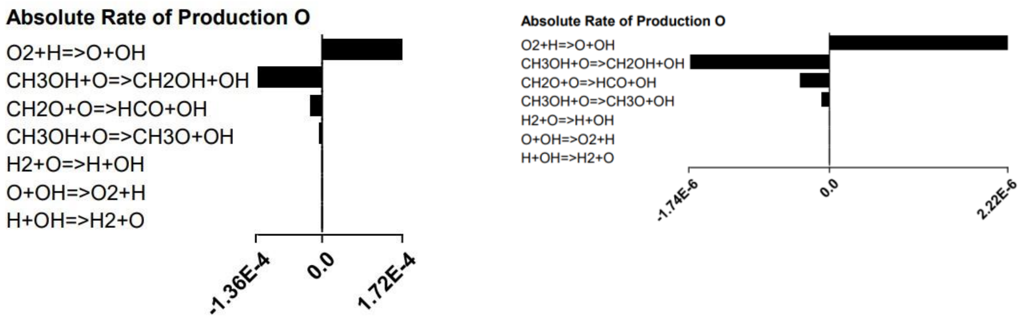

Figure 74 presents the absolute production rates of the significant for the production of HO_2 radicals, reactions, as identified in the context of this work, for the cases of the mixture of methanol using CO_2 and N_2 as diluent. In both cases, the most important reactions for the production of HO_2 are the following:

$CH_2OH + O_2 = CH_2O + HO_2$

$HCO + O_2 = CO + HO_2$

Figure 74. Absolute production rates for the HO_2-producing elementary reactions for (a) CH_3OH - N_2 mixture, (b) CH_3OH - CO_2 mixture (φ=0.5, P=220 atm, and T=700 K), at axial position x=0.1cm.

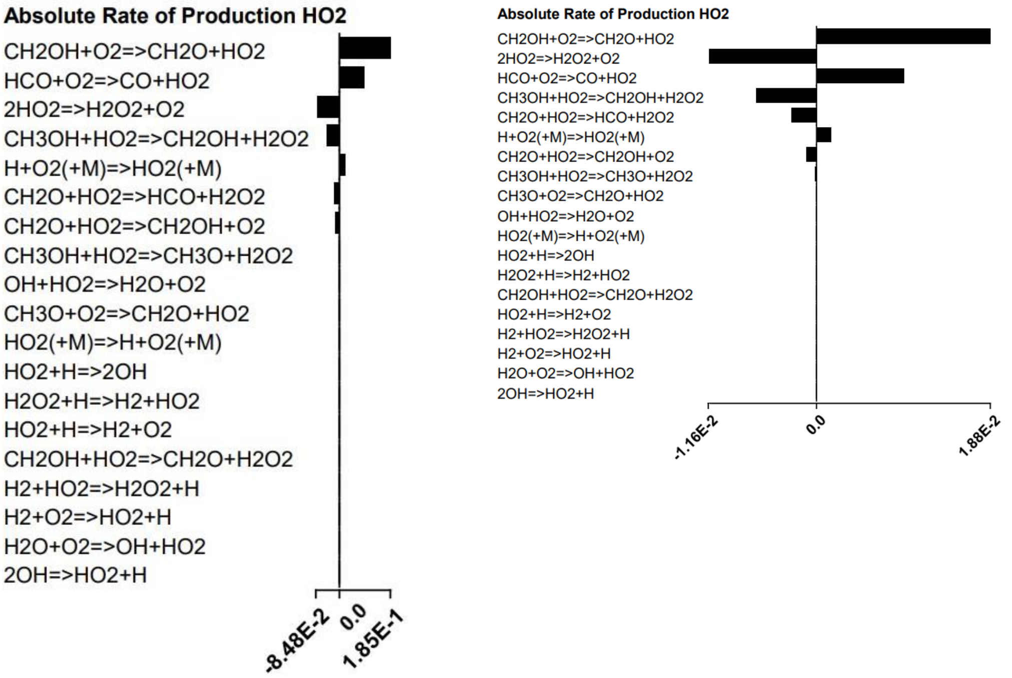

The below figures depict the absolute consumption and production rates, respectively, of the significant for the consumption of CH_3OH and production of OH, H, O and HO_2 radicals, reactions at the ending axial position x=0.2 cm.

It is evident that CH_3OH has been almost completely consumed.

Figure 75. Absolute rates of CH_3OH consumption, for (a) CH_3OH - N_2 mixture, (b) CH_3OH - CO_2 mixture (φ=0.5, P=220 atm, and T=700 K), at ending axial position x=0.2 cm.

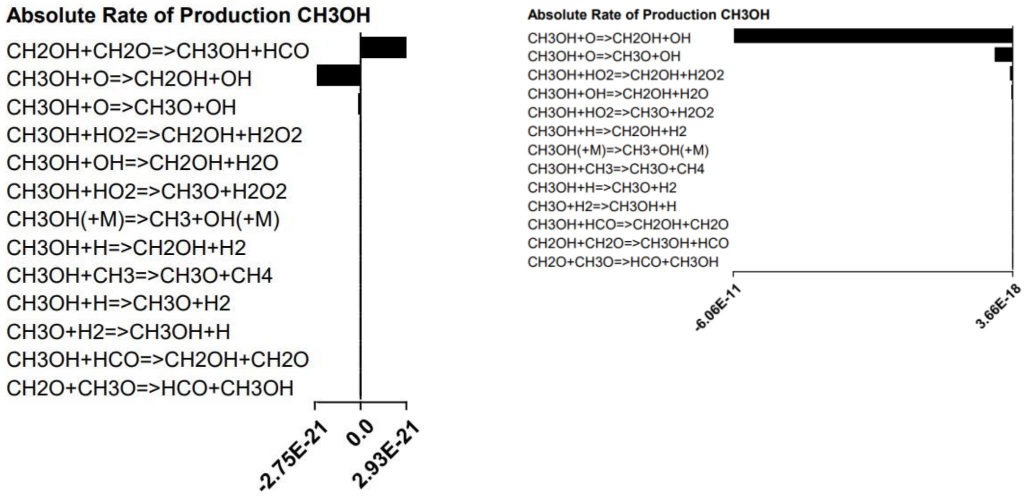

Figure 76. Absolute production rates for the OH-producing elementary reactions for (a) CH_3OH - N_2 mixture, (b) CH_3OH - CO_2 mixture (φ=0.5, P=220 atm, and T=700 K), at ending axial position x=0.2 cm.

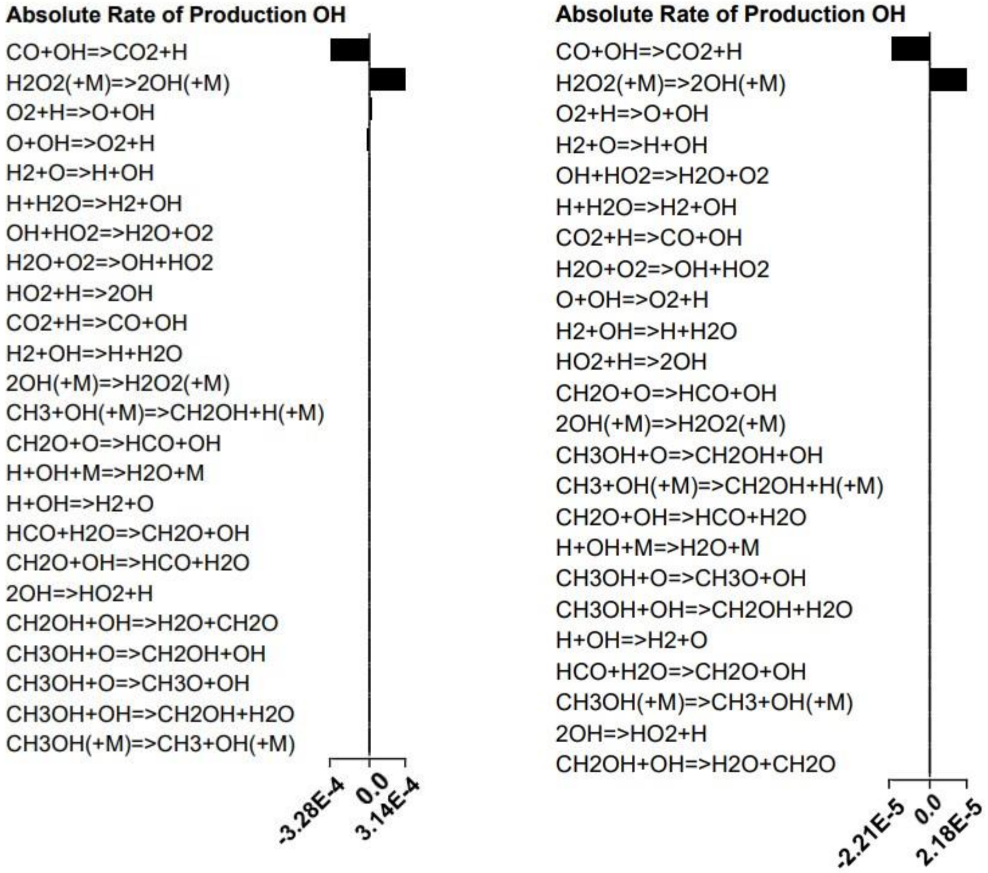

Figure 77. Absolute production rates for the H-producing elementary reactions for (a) CH_3OH - N_2 mixture, (b) CH_3OH - CO_2 mixture (φ=0.5, P=220 atm, and T=700 K), at ending axial position x=0.2 cm.

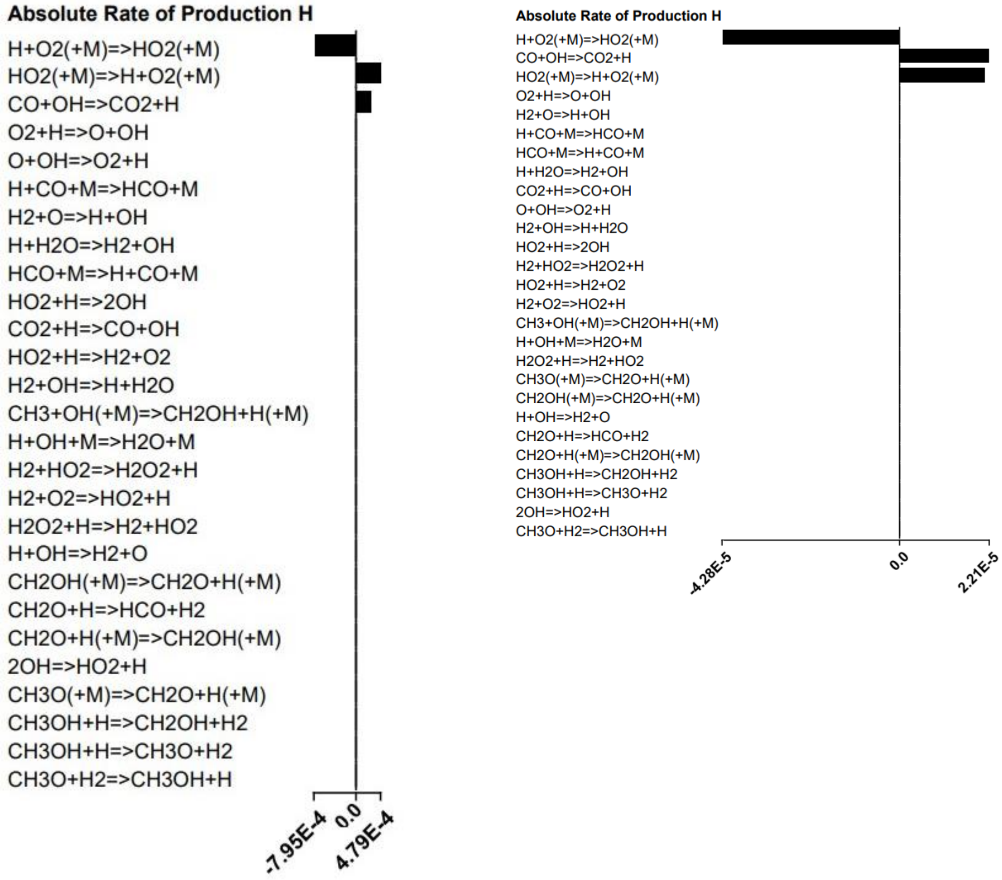

Figure 78. Absolute production rates for the O-producing elementary reactions for (a) CH_3OH - N_2 mixture, (b) CH_3OH - CO_2 mixture (φ=0.5, P=220 atm, and T=700 K), at ending axial position x=0.2 cm.

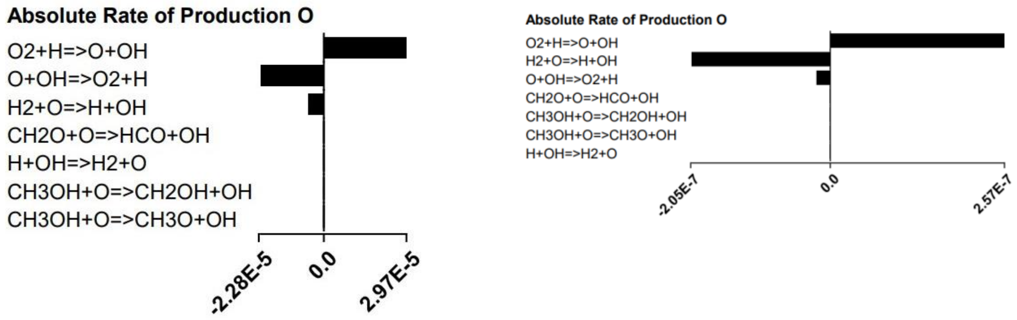

Figure 79. Absolute production rates for the HO_2-producing elementary reactions for (a) CH_3OH - N_2 mixture, (b) CH_3OH - CO_2 mixture (φ=0.5, P=220 atm, and T=700 K), at ending axial position x=0.2 cm.

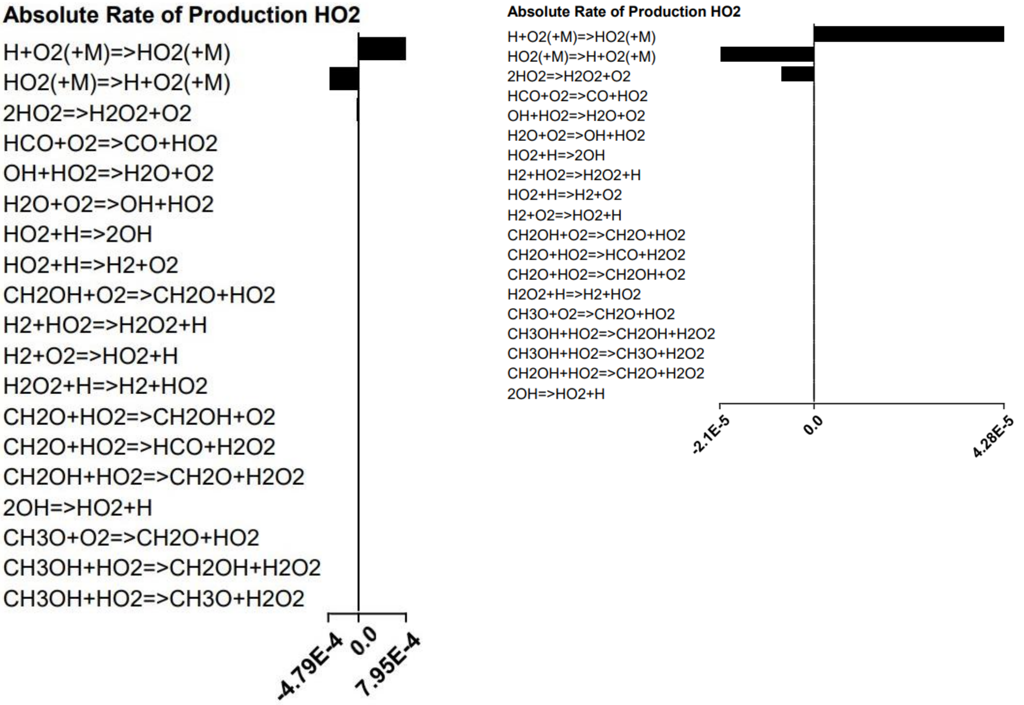

1800K

The figures below present the absolute consumption rates of the significant, for the consumption of CH_3OH reactions, as identified in the context of this work, for the cases of the mixture of methanol using N_2 and CO_2 as diluent at conditions φ=0.5, p=200 atm, T_{un}=1800 K. It is evident that, in both mixtures, the dominant radical for the consumption of CH_3OH is the hydroxyl radical (OH), as the most important reaction contributing to CH_3OH consumption is the following:

$CH_3OH + OH = CH_2OH + H_2O$

The total absolute consumption rate of CH_3OH is a little higher in the case on CH_3OH – N_2 mixture compared to the CH_3OH – CO_2 mixture.

Figure 80. Absolute rates of CH_3OH consumption, for (a) CH_3OH - N_2 mixture, (b) CH_3OH - CO_2 mixture (φ=0.5, P=200 atm, and T=1800 K), at axial position x=0 cm.

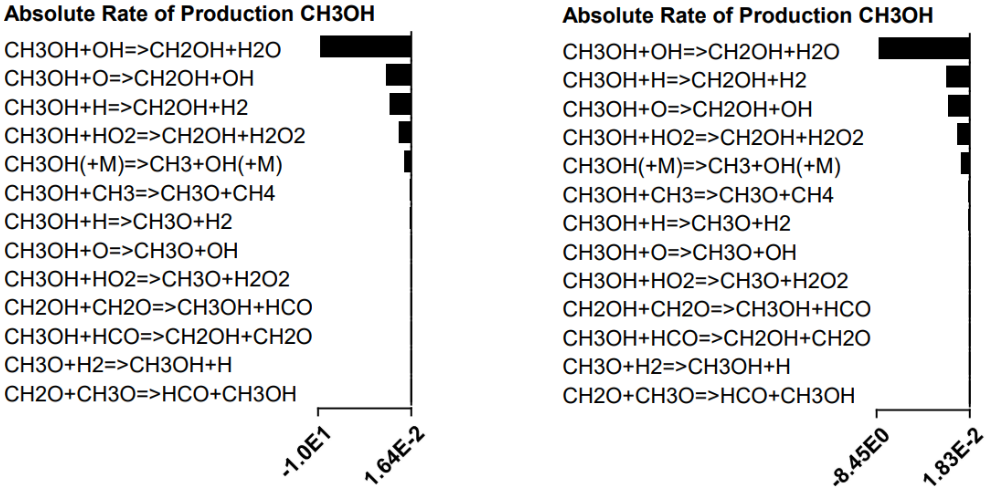

Figure 81 presents the absolute production rates of the significant, for the production of OH radicals, reactions, as identified in the context of this work, for the cases of the mixture of methanol using N_2 and CO_2 as diluent. In both cases, the most important reaction contributing to OH production is the following:

H_2O_2 (+M) = 2OH (+M)

The total absolute rate of OH production is almost equal between the two cases of the CH_3OH-N_2 mixture and CH_3OH - CO_2 mixture.

Figure 81. Absolute production rates for the OH-producing elementary reactions for (a) CH_3OH - N_2 mixture, (b) CH_3OH - CO_2 mixture (φ=0.5, P=200 atm, and T=1800 K), at axial position x=0 cm.

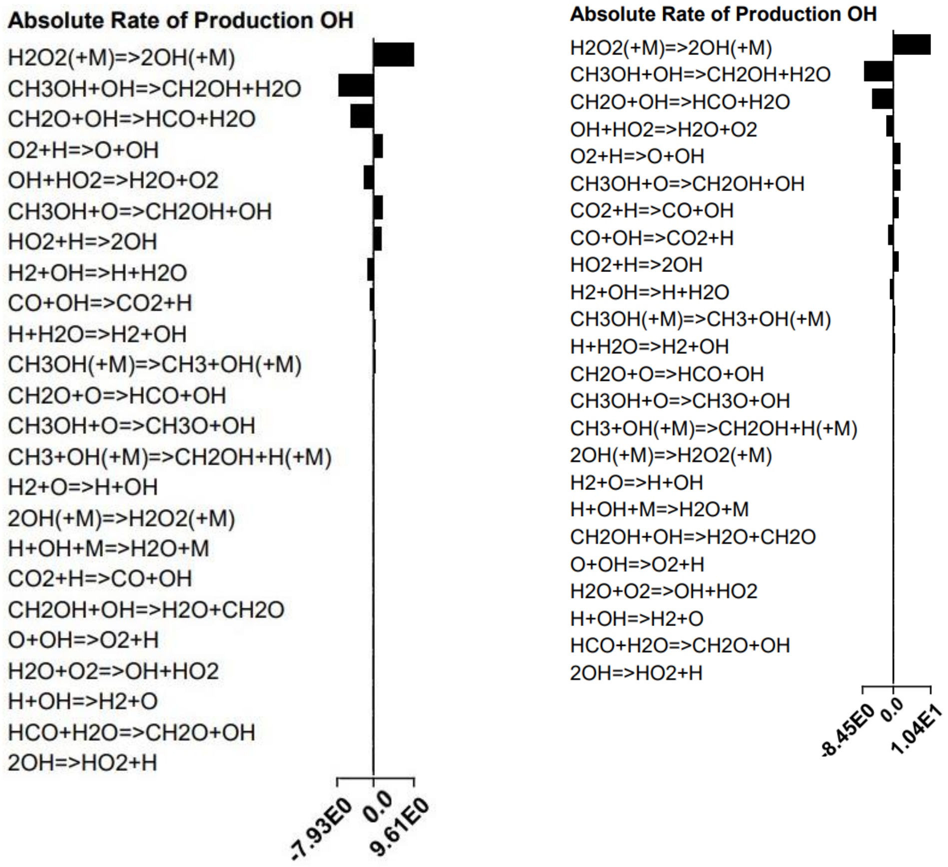

Figure 82 presents the absolute production rates of the significant, for the production of H radicals, reactions, as identified in the context of this work, for the cases of the mixture of methanol using N_2 and CO_2 as diluent. For both CH_3OH mixtures the most important reactions for the production of H are the following:

$HCO + M = H + CO + M$

$HO_2\ (+M) = H + O_2\ (+M)$

Figure 82. Absolute production rates for the H-producing elementary reactions for (a) CH_3OH - N_2 mixture, (b) CH_3OH - CO_2 mixture (φ=0.5, P=200 atm, and T=1800 K), at axial position x=0 cm.

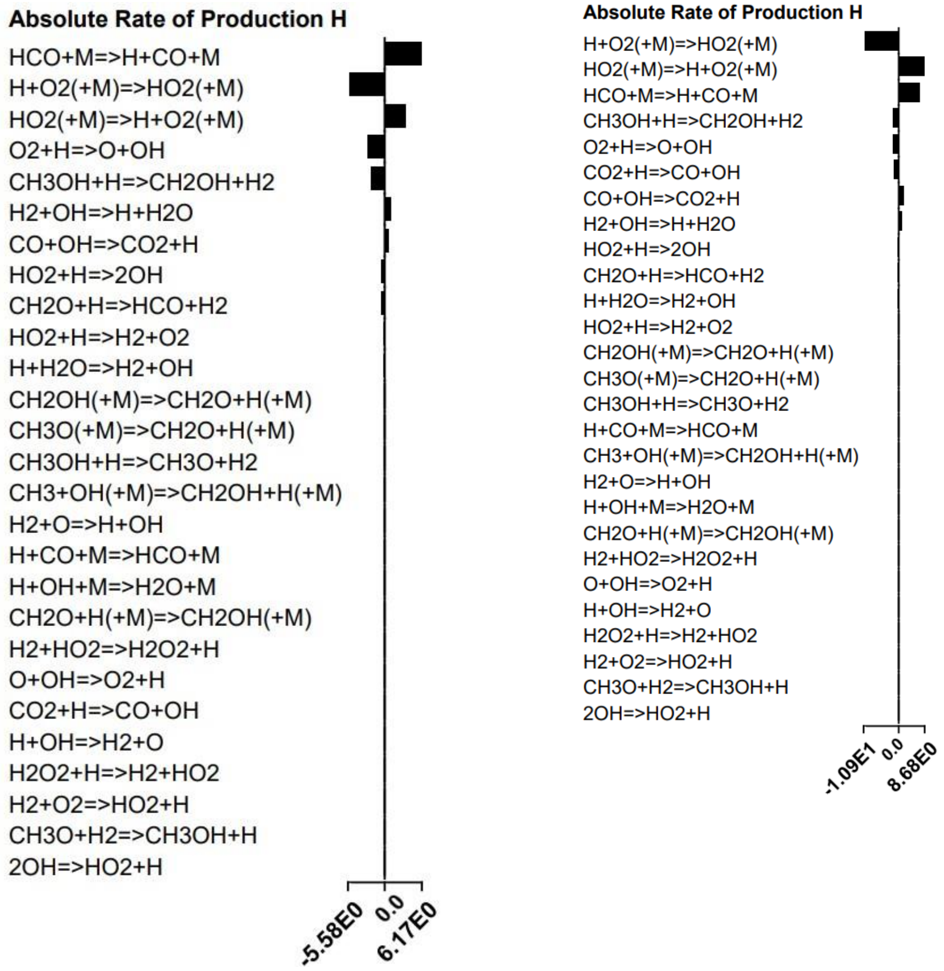

Figure 83 presents the absolute production rates of the significant for the production of O radicals, reactions, as identified in the context of this work, for the cases of the mixture of methanol using N_2 and CO_2 as diluent.

Figure 83. Absolute production rates for the O-producing elementary reactions for (a) CH_3OH - N_2 mixture, (b) CH_3OH - CO_2 mixture (φ=0.5, P=200 atm, and T=1800 K), at axial position x=0 cm.

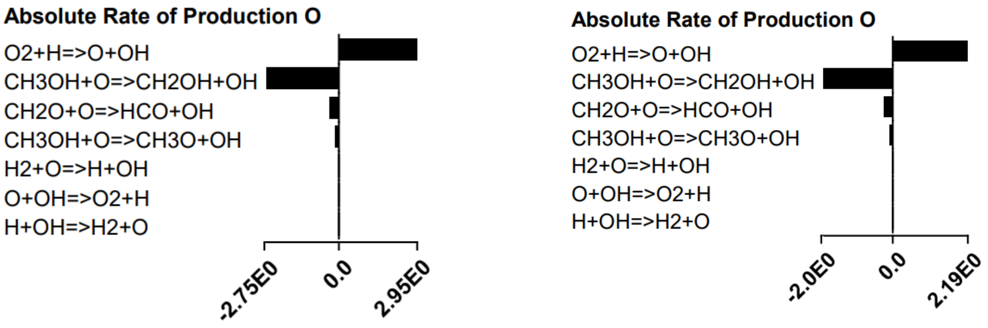

Figure 84 presents the absolute production rates of the significant for the production of HO_2 radicals, reactions, as identified in the context of this work, for the cases of the mixture of methanol using CO_2 and N_2 as diluent. In both cases, the most important reactions for the production of HO_2 are the following:

$CH_2OH + O_2 = CH_2O + HO_2$

$H + O_2\ (+M) = HO_2\ (+M)$

Figure 84. Absolute production rates for the HO_2-producing elementary reactions for (a) CH_3OH - N_2 mixture, (b) CH_3OH - CO_2 mixture (φ=0.5, P=200 atm, and T=1800 K), at axial position x=0 cm.

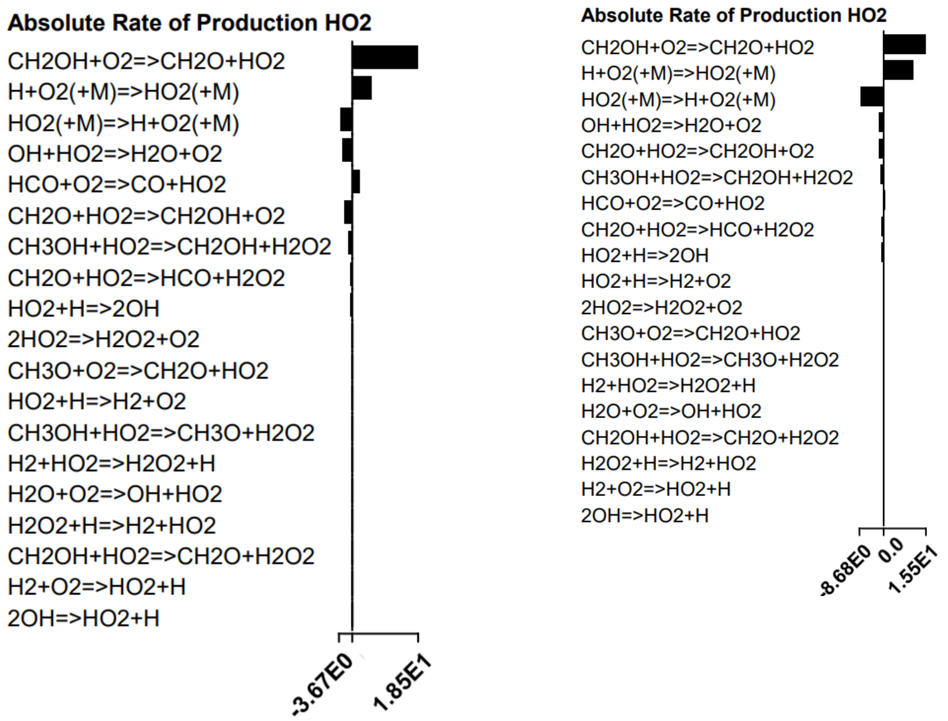

The below figures depict the absolute consumption and production rates, respectively, of the significant for the consumption of CH_3OH and production of OH, H, O and HO_2 radicals, reactions at the ending axial position x=0.2 cm.

It is evident that CH_3OH has been almost completely consumed.

Figure 85. Absolute rates of CH_3OH consumption, for (a) CH_3OH - N_2 mixture, (b) CH_3OH - CO_2 mixture (φ=0.5, P=200 atm, and T=1800 K), at ending axial position x=0.2 cm.

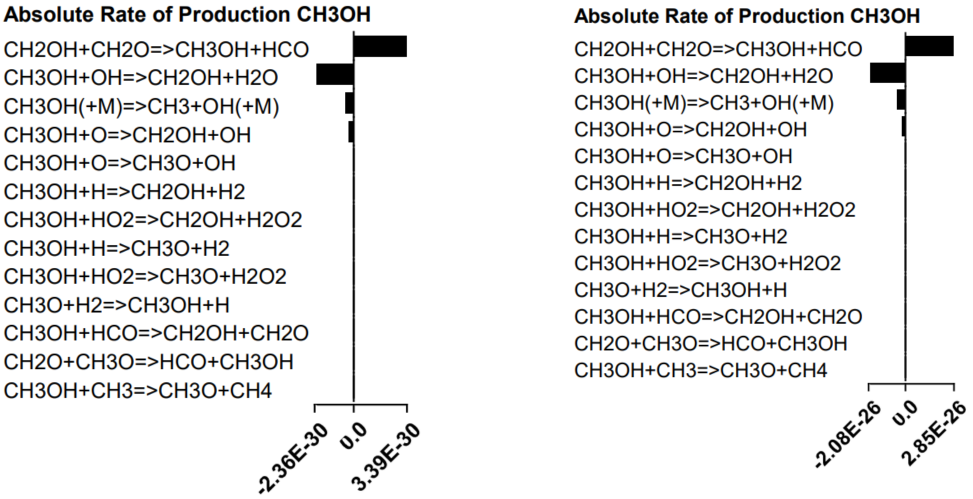

Figure 86. Absolute production rates for the OH-producing elementary reactions for (a) CH_3OH - N_2 mixture, (b) CH_3OH - CO_2 mixture (φ=0.5, P=200 atm, and T=1800 K), at ending axial position x=0.2 cm.

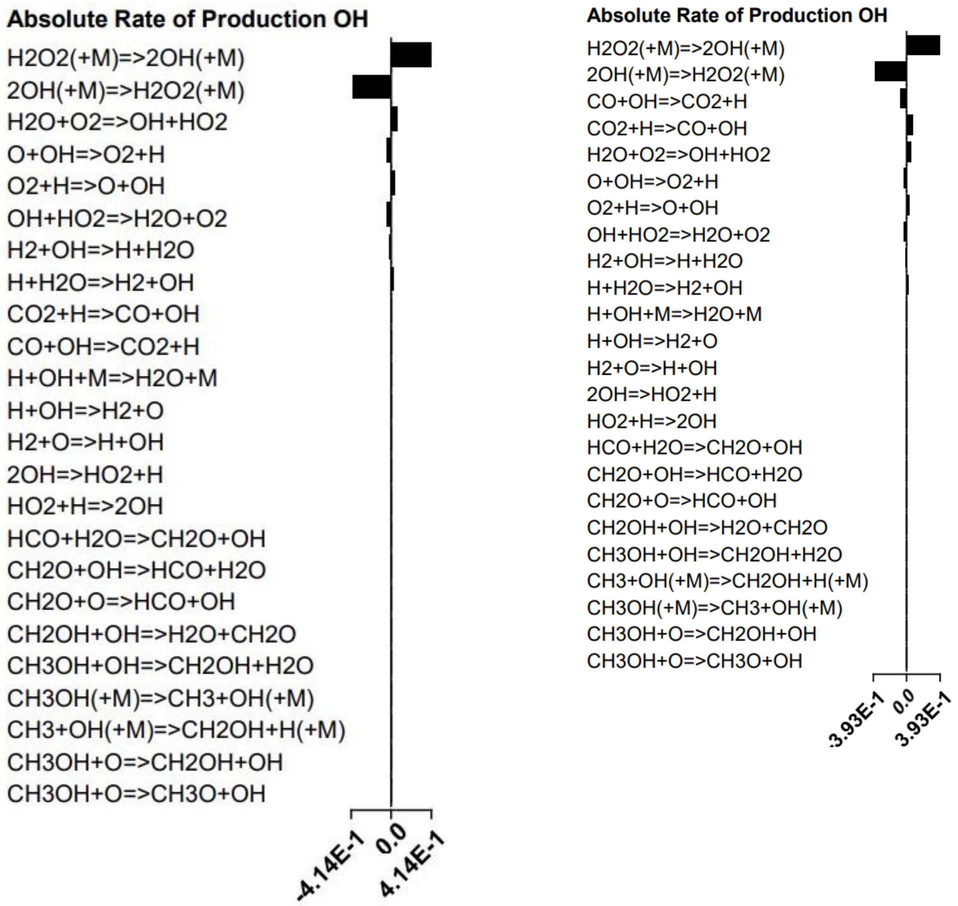

Figure 87. Absolute production rates for the H-producing elementary reactions for (a) CH_3OH - N_2 mixture, (b) CH_3OH - CO_2 mixture (φ=0.5, P=200 atm, and T=1800 K), at ending axial position x=0.2 cm.

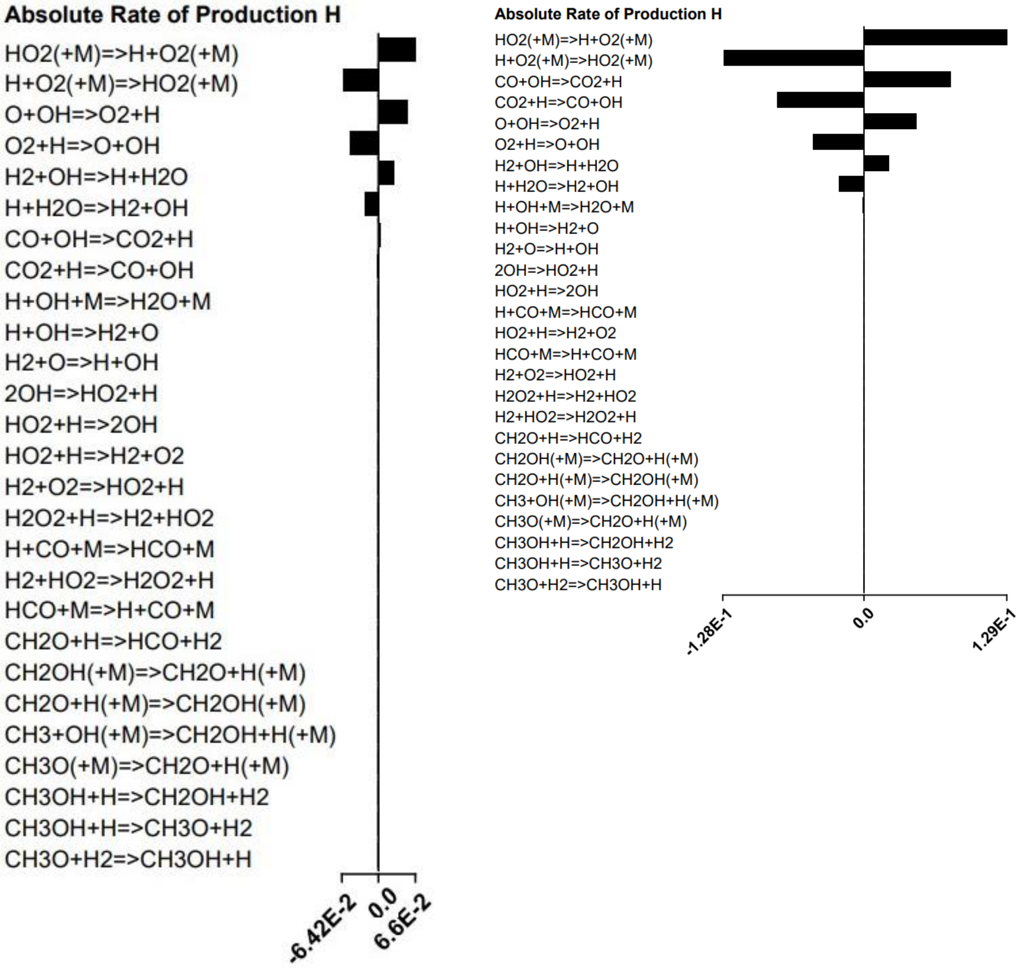

Figure 88. Absolute production rates for the O-producing elementary reactions for (a) CH_3OH - N_2 mixture (φ=0.5, P=200 atm, and T=1800 K), at ending axial position x=0.2 cm.

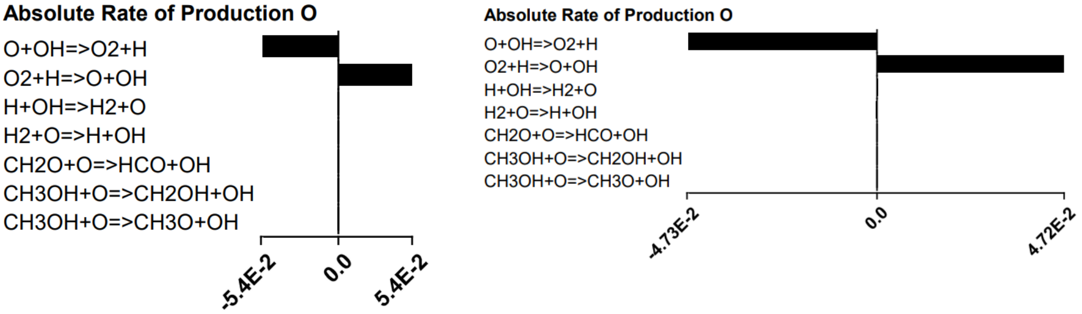

Figure 89. Absolute production rates for the HO_2-producing elementary reactions for (a) CH_3OH - N_2 mixture (φ=0.5, P=200 atm, and T=1800 K), at ending axial position x=0.2 cm.

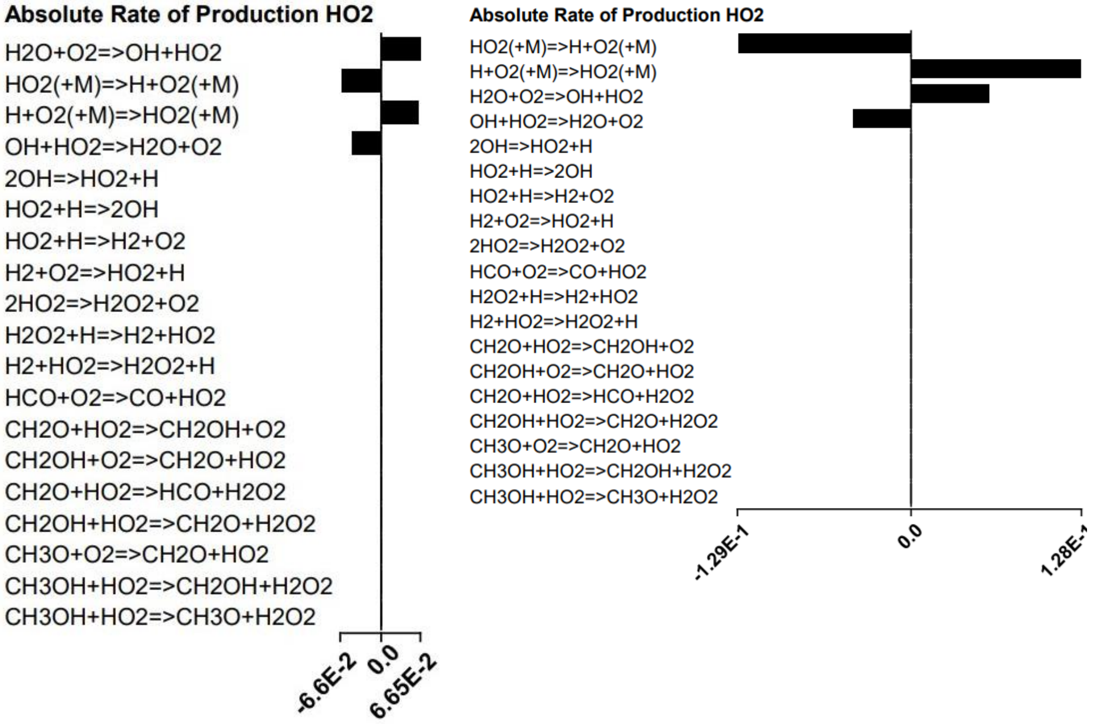

CHAPTER 6: Conclusions

The goal of the present study has been to perform a comprehensive investigation of ignition and combustion of CH_3OH – O_2 mixtures under sCO_2 conditions. To this end, an approach consisting of the following steps has been undertaken: (**i**) Extensive literature review for finding reduced and detailed chemical kinetic mechanisms pertinent to methanol combustion at high pressures, (**ii**) Assessment of the reduced-order chemical kinetic mechanism *ACR55*, comprising 18 species and 55 irreversible elementary reactions, against experimental data and present computational results of the *Updated HP-Mech* mechanism, including: (a) shock tube ignition delay times of CH_3OH mixtures, (b) JSR speciation data regarding CH_3OH oxidation, and (c) laminar flame speed of premixed flames for a reference set of conditions. The *ACR55* mechanism was shown to perform satisfactorily against the validation targets, for most of the cases considered, and was therefore adopted for further analysis. (**iii**) Investigation of the effects of s-CO_2 dilution in terms of calculations for the above three reference problems, for: (a) N_2 as diluent, and (b) s-CO_2 as diluent, at the same conditions, representative of gas turbine and marine dual-fuel engine combustion. Here, the following range was investigated: pressures of 175 – 250 atm, initial temperatures (mainly) of 1300 – 1800 K, equivalence ratios of 0.5 – 2.0. (**iv**) Rate Of Production (ROP) analysis, to identify the principal chemical pathways. ROP analysis can enable an understanding of the identified differences between N_2- and s-CO_2 dilution. The following cases were considered in the present ROP analysis: (a) Ignition of homogeneous mixture: $\varphi=0.5$, T=1500 K, p=220 bar. (b) Combustion at PSR conditions: T=1500 K, p=220 bar, $\varphi=0.8$ and $\varphi=2.0$. (c) Premixed laminar flame: unburned mixtures with T=700 K and T=1800 K, $\varphi=0.5$, p=200 atm and p=220 atm.

The main findings of the present investigation can be summarized as follows:

A. Ignition of Homogeneous Mixtures:

- Both mechanisms used, the *ACR55* and the *Updated HP-Mech*, bear similar results for ignition delay times for the two cases studied, namely: i) s-CO_2 dilution, and ii) N_2 dilution.
- For s-CO_2 dilution, ignition delay times are lower compared to the corresponding ones of N_2 dilution, for $\varphi=0.8$-1.5, for all pressures, in the high temperature range (T=1500-1800 K). The differences diminish for rich mixtures. This temperature range becomes narrower at increasing pressure.

B. Combustion at Perfectly Stirred Reactor conditions:

- The *ACR55* mechanism and the *Updated HP-Mech* mechanism bear similar results, in the entire range of conditions considered.
- CO production is found to be higher for s-CO_2 dilution.
- CO_2 production is higher for N_2 dilution, for lean and stoichiometric mixtures. For rich mixtures, the final concentration of CO_2 is lower than the initial 85% concentration of CO_2 for the case of sCO_2 as diluent.

C. Premixed Laminar Flames:

- The two mechanisms (*ACR55* mechanism and the *Updated HP-Mech*) bear similar results, in the entire range of conditions considered.
- For unburned mixture temperatures of 600 K and 700 K, for all stoichiometries, the laminar flame speed is significantly higher for N_2 dilution.

- For unburned mixture temperature of 1800 K and lean mixtures, the laminar flame speed is moderately higher for N_2 dilution; for rich mixtures, the laminar flame speed is substantially higher for N_2 dilution.

In summary, the present study forms a significant step towards understanding the ignition and combustion of methanol under s-CO_2 conditions, a topic of current interest for gas turbine and marine applications for greenhouse gas (GHG) emissions reduction.

The present results can be used in future studies of propulsion applications using s-CO_2 dilution. These can include gas turbine and marine propulsion applications, towards minimizing GHG emissions. The main conclusions presented above can be used in the preliminary design of such applications. In the same context, the *ACR55* mechanism, validated and extensively tested in the present study for a wide range of s-CO_2 dilution conditions, can be implemented in thermodynamic and CFD codes, and used in relevant parametric and optimization computational studies.

References

Bayraktar, M., & Yuksel, O. (2023). “A scenario-based assessment of the energy efficiency existing ship index (EEXI) and carbon intensity indicator (CII) regulations”. *Ocean Engineering 278:(Jun)* 114295. https://doi.org/10.1016/j.oceaneng.2023.114295

Beeckmann, J., Cai, L., & Pitsch, H. (2014). “Experimental investigation of the laminar burning velocities of methanol, ethanol, n-propanol, and n-butanol at high pressure”, *Fuel* 117 (Part A): 340–350. https://doi.org/10.1016/j.fuel.2013.09.025

Bilgili, L., & Olçer, A. I. (2024). “IMO 2023 strategy-Where are we and what’s next?”, *Marine Policy 160:(Feb)* 105953. https://doi.org/10.1016/j.marpol.2023.105953

Budisa, N., & Schulze-Makuch, D. (2014). “Supercritical Carbon Dioxide and Its Potential as a Life-Sustaining Solvent in a Planetary Environment”, *Life* 4: 331-340. doi:10.3390/life4030331

Burke, U., Metcalfe, W. K., Burke, S. M., Heufer, K. A., Dagaut, P., & Currana, H. J. (2016). “A detailed chemical kinetic modeling, ignition delay time and jet-stirred reactor study of methanol oxidation”, *Combustion and Flame* 165 (Mar): 125–136. http://dx.doi.org/10.1016/j.combustflame.2015.11.004

Djermouni, M. & Ouadha, A. (2023). “Thermodynamic analysis of methanol, ammonia, and hydrogen as alternative fuels in HCCI engines”, *International Journal of Thermofluids* 19 (Aug): 100372. https://doi.org/10.1016/j.ijft.2023.100372

Elmi, Z., Li, B., Fathollahi-Fard, A. M., Tian, G., Borowska-Stefanska, M., Wisniewski, S., & Dulebenets, M. A. (2023). “Ship schedule recovery with voluntary speed reduction zones and emission control areas”, *Transportation Research* Part D 125 (Dec): 103957. https://doi.org/10.1016/j.trd.2023.103957

Fu, H., Wang, Y., Liu, B., Wang, Z., Zhang, X., & Liu, G. (2024). “Experimental and theoretical study of cyclopropanated fuel exo, exo-Tetracyclo[3.3.1.$0^{2,4}$.$0^{6,8}$]nonane pyrolysis in a jet-stirred reactor” , Fuel 361 (Apr): 130702. https://doi.org/10.1016/j.fuel.2023.130702

Johansen, K. (2015). “Multi-catalytic soot filtration in automotive and marine applications”. *Catalysis Today 258(Part 1):(Dec)* 2–10. http://dx.doi.org/10.1016/j.cattod.2015.06.001

Jung, Y., Pyo, Y., Jang, J., Woo, Y., Ko, A., Kim, G., Shin, Y., & Cho, C. (2022). “Nitrous oxide in diesel aftertreatment systems including DOC, DPF and urea-SCR”, *Fuel 310* (Part C): (Feb) 122453.https://doi.org/10.1016/j.fuel.2021.122453

Lee, S.-S. (2024). “Analysis of the effects of EEDI and EEXI implementation on CO_2 emissions reduction in ships”. *Ocean Engineering 295:(Mar)* 116877. https://doi.org/10.1016/j.oceaneng.2024.116877

Pichler, C., & Nilsson E. J. K. (2018). “Reduced Kinetic Mechanism for Methanol Combustion in Spark-Ignition Engines”, *Energy Fuels* 32 (12):12805−12813.DOI: 10.1021/acs.energyfuels.8b02136

Shao, S., Tan, Z., Wang, T., & Liu, Z. (2023). “Configuration design of the emission control areas for coastal ships:A Stackelberg game model”, *Transportation Research* Part E 172: (Apr) 103072. https://doi.org/10.1016/j.tre.2023.103072

Topic, T., Murphy, A. J., Pazouki, K., & Norman, R. (2023). “NOx Emissions Control Area (NECA) scenario for ports in the North Adriatic Sea”, *Journal of Environmental Management* 344 (Oct): 118712. https://doi.org/10.1016/j.trd.2023.103957

Trivanovic, U., Corbin, J. C., Baldelli, A., Peng, W., Yang, J., Kirchen, P., Miller, J. W., Lobo, P., Gagné, S., & Rogak, S. N. (2019). “Size and morphology of soot produced by a dual-fuel marine engine”. Journal of Aerosol Science 138:(Dec) 105448. https://doi.org/10.1016/j.jaerosci.2019.105448

Ushakov, S., Stenersen, D., & Einang, P. M. (2019). “Methane slip from gas fuelled ships: A comprehensive summary based on measurement data”. *Journal of Marine Science and Technology 24:(Jan)* 1308–1325. https://doi.org/10.1007/s00773-018-00622-z

Van, T. C., Ramirez, J., Rainey, T., Ristovski, Z., & Brown, R. J. (2019). “Global impacts of recent IMO regulations on marine fuel oil refining processes and ship emissions”. *Transportation Research (Part D): Transport and Environment 70:(May)* 123-134. https://doi.org/10.1016/j.trd.2019.04.001

Van, T. C., Ramirez, J., Rainey, T., Ristovski, Z., & Brown, R. J. (2019). Transportation Research Part D 70 (May): 123-134. https://doi.org/10.1016/j.trd.2019.04.001

Vancoillie, J., Christensen, M., Nilsson, E. J. K., Verhelst, S., & Konnov, A. A. (2012). “Temperature Dependence of the Laminar Burning Velocity of Methanol Flames”, *Energy Fuels* 26: 1557−1564. dx.doi.org/10.1021/ef2016683

Wang, C., Liu, H., Zhang, M., Zhong, X., Wang, H., Jin, C., & Yao, M. (2023). “Experimental and kinetic modeling studies on oxidation of methanol and di-tert-butyl peroxide in a jet-stirred reactor”, *Combustion and Flame* 258 (Part 2): 113093. https://doi.org/10.1016/j.combustflame.2023.113093

Wang, Z., Zhao, H., Yan, C., Lin, Y., Lele, A. D., Xu, W., Rotavera, B., Jasper, A. W., Klippenstein, S. J., & Ju, Y. (2022). “Methanol oxidation up to 100 atm in a supercritical pressure jet-stirred reactor”, *Proceedings of the Combustion Institute* 39 (1): 445-453. https://doi.org/10.1016/j.proci.2022.07.068

Zhang, Y., Xia, C., Liu, D., Zhu, Y., & Feng, Y. (2023). “Experimental investigation of the high-pressure SCR reactor impact on a marine two-stroke diesel engine”, *Fuel* 335 (Mar): 127064. https://doi.org/10.1016/j.fuel.2022.127064

Zhang, Z., Huang, Z., Wang, X., Xiang, J., Wang, X., & Miao, H. (2008). “Measurements of laminar burning velocities and Markstein lengths for methanol–air–nitrogen mixtures at elevated pressures and temperatures”, *Combustion and Flame* 155 (3): 358–368. https://doi.org/10.1016/j.combustflame.2008.07.005

Zhao, B., Liang, X., Wang, K., Li, T., Lv, X., & Zhang, S. (2022). “Impact of sulfur functional groups on physicochemical properties and oxidation reactivity of diesel soot particles”. *Fuel 327:(Nov)* 125041. https://doi.org/10.1016/j.fuel.2022.125041

Zhou, F., Yu, J., Wu, C., Fu, J., Liu, J., & Duan, X. (2024). “The application prospect and challenge of the alternative methanol fuel in the internal combustion engine”, *Science of the Total Environment* 913 (Feb): 169708. https://doi.org/10.1016/j.scitotenv.2023.169708

https://www.wartsila.com/marine/decarbonisation/adopting-methanol-as-marine-fuel

Reducing GHG emissions - ETS Extension to maritime - EMSA - European Maritime Safety Agency (europa.eu)

Reducing GHG emissions - MRV Regulation Changes - EMSA - European Maritime Safety Agency (europa.eu)

Appendix I: Reduced order chemical kinetics mechanism of methanol combustion – Nilsson

Table 95 shows the elements, species and elementary reactions of the reduced-order mechanism *ACR55* of Pichler & Nilsson (2018).

Table 95: Reduced-order Mechanism *ACR55*

Reduced-order Mechanism *ACR55*				
Elements	O N HE AR H C			
Species	CH_2OH H_2O O CH_3O HO_2 CO_2 OH N_2 O_2 HCO H_2O_2 CH_4 CH_2O CH_3 CH_3OH H_2			
Number	**Reactions**	**Pre-exponential factor, A (mole-cm-s-K)**	**Exponent of temperature n[-]**	**Activation Energy E_a (cal/mole)**
1.	$CH_2OH+O_2=>CH_2O+HO_2$	1.6211E+14	0.00000	5017.000
2.	$CH_2O+HO_2=>CH_2OH+O_2$	3.8506E+15	-0.12690	25426.450
3.	$H_2+OH=>H+H_2O$	6.2119E+13	0.00000	6990.000
4.	$H+H_2O=>H_2+OH$	4.0260E+15	-0.36380	22641.320
5.	$H_2+O=>H+OH$	5.0800E+04	2.67000	6292.000
6.	$H+OH=>H_2+O$	3.7800E+04	2.60750	4963.430
7.	$CH_2OH+HO_2=>CH_2O+H_2O_2$	1.4205E+12	0.00000	0.000
8.	$H+OH+M=>H_2O+M$	3.5000E+22	-2.00000	0.000
	H_2/0.73/ H_2O/3.65/ CH_4/2/			
9.	$O_2+H=>O+OH$	1.0400E+14	0.00000	15286.000
10.	$O+OH=>O_2+H$	2.7690E+11	0.40110	-1483.240
11	$CH_2OH+OH=>H_2O+CH_2O$	4.5695E+13	0.00000	0.000
12.	$CH_3O+O_2=>CH_2O+HO_2$	2.3974E-19	9.50000	-5501.000
13.	$H_2O_2(+M)=>2OH(+M)$	2.0000E+12	0.90000	48748.990
	H_2O/7.65/ CO_2/1.6/ N_2/1.5/ O_2/1.2/ H_2O_2/7.7/ H_2/3.7/ CO/2.8/ LOW / 2.4900E+24 -2.30000 48748.990/ TROE / 4.3000E-01 1.0000E-30 1.0000E+30 /			
14.	$2OH(+M)=>H_2O_2(+M)$	1.6060E+05	2.35580	-3518.090
	H_2O/7.65/ CO_2/1.6/ N_2/1.5/ O_2/1.2/ H_2O_2/7.7/ H_2/3.7/ CO/2.8/ LOW / 2.0000E+17 -0.84000 -3518.090/ TROE / 4.3000E-01 1.0000E-30 1.0000E+30 /			
15.	$H_2O_2+H=>H_2+HO_2$	2.1500E+10	1.00000	6000.000
16.	$H_2+HO_2=>H_2O_2+H$	6.0890E+07	1.63050	21998.800
17.	$CH_2O(+M)=>CO+H_2(+M)$	6.3368E+13	0.02050	82259.230
	H_2/2/ H_2O/6/ CO/1.5/ CO_2/2/ CH_4/2/ LOW / 5.2047E+33 -4.90000 87007.230/ TROE / 9.3200E-01 1.9700E+02 1.5400E+03 1.0300E+04 /			
18.	$CH_2O+O=>HCO+OH$	5.2409E+09	1.15000	2260.000
19.	$CH_2O+H=>HCO+H_2$	3.1043E+07	1.90000	2740.000
20.	$CH_2O+OH=>HCO+H_2O$	7.7247E+07	1.63000	-1055.000
21.	$HCO+H_2O=>CH_2O+OH$	1.2443E+06	1.82360	29191.440
22.	$CH_2O+HO_2=>HCO+H_2O_2$	2.0724E+04	2.70000	11520.000
23.	$HO_2+H=>H_2+O_2$	1.1400E+10	1.08270	553.780

24.	$H_2+O_2=>HO_2+H$	5.4430E+08	1.59470	54719.410
25.	$OH+HO2=>H_2O+O_2$	7.0000E+12	0.00000	-1092.960
	DUP			
26.	$2HO_2=>H_2O_2+O_2$	1.0000E+14	0.00000	11040.880
	DUP			
27.	$2HO_2=>H_2O_2+O_2$	1.9000E+11	0.00000	-1408.920
	DUP			
28.	$HO_2+H=>2OH$	7.0790E+13	0.00000	295.000
29.	$2OH=>HO_2+H$	6.6960E+09	0.85060	36362.820
30.	$HCO+M=>H+CO+M$	5.7000E+11	0.66000	14870.000
	H_2/2/ H_2O/6/ CO/1.5/ CO_2/2/ CH_4/2/			
31.	$H+CO+M=>HCO+M$	4.1030E+08	1.58210	-2384.350
	H_2/2/ H2O/6/ CO/1.5/ CO_2/2/ CH_4/2/			
32.	$CO+OH=>CO_2+H$	7.0150E+04	2.05300	-355.700
33.	$CO_2+H=>CO+OH$	3.8290E+11	0.77510	25308.850
34.	$HCO+O_2=>CO+HO_2$	6.6758E+12	0.00000	410.000
35.	$CH_2O+CH_3O=>HCO+CH_3OH$	2.7367E+11	0.00000	2294.000
36.	$H+O_2(+M)=>HO_2(+M)$	4.6500E+12	0.44000	0.000
	H_2/1.3/ CO/1.9/ CO_2/3.8/ H_2O/10/ CH_4/2/ LOW / 1.7370E+19 -1.23000 0.000/ TROE / 6.7000E-01 1.0000E-30 1.0000E+30 1.0000E+30 /			
37.	$HO_2(+M)=>H+O_2(+M)$	3.2490E+14	-0.04660	50168.080
	H_2/1.3/ CO/1.9/ CO_2/3.8/ H_2O/10/ CH_4/2/ LOW / 1.2140E+21 -1.72000 50168.080/ TROE / 6.7000E-01 1.0000E-30 1.0000E+30 1.0000E+30 /			
38.	$OH+HO_2=>H_2O+O_2$	4.5000E+14	0.00000	10929.600
	DUP			
39.	$H_2O+O_2=>OH+HO_2$	1.9750E+15	0.14820	80746.550
40.	$CH_2O+H(+M)=>CH_2OH(+M)$	7.3512E+11	0.45400	3600.000
	H_2/2/ H_2O/6/ CO/1.5/ CO_2/2/ CH_4/2/ LOW / 7.0205E+31 -4.82000 6530.000/ TROE / 7.1870E-01 1.0300E+02 1.2910E+03 4.1600E+03 /			
41.	CH2OH(+M)=>CH2O+H(+M)	3.6522E+12	0.09420	33358.630
	H_2/2/ H_2O/6/ CO/1.5/ CO_2/2/ CH_4/2/ LOW / 5.0403E+32 -5.18000 36288.630/ TROE / 7.1870E-01 1.0300E+02 1.2910E+03 4.1600E+03 /			
42.	$CH_3O(+M)=>CH_2O+H(+M)$	2.4668E+13	0.00000	26170.000
	H_2/2/ H_2O/6/ CO/1.5/ CO_2/2/ CH_4/2/ LOW / 4.9534E+24 -3.00000 24307.000/ TROE / 9.0000E-01 2.5000E+03 1.3000E+03 1.0000E+99 /			
43.	$H_3+OH(+M)=>CH_2OH+H(+M)$	1.0002E+09	0.99600	31.000
	LOW / 1.0085E+07 5.01000 1887.000/ TROE / 8.6220E-01 9.3210E+03 3.6180E+02 3.1250E+03 /			
44.	$CH_3OH(+M)=>CH_3+OH(+M)$	2.2172E+18	-0.61500	92540.590
	LOW / 9.4041E+42 -7.00000 97992.190/ TROE / -4.7480E-01 3.5580E+04 1.1160E+03 9.0230E+03 /			
45.	$CH_3OH+H=>CH_3O+H_2$	1.4100E+05	2.56000	10300.000
46.	$CH_3O+H_2=>CH_3OH+H$	2.6789E+04	2.63200	8116.770
47.	$CH_3OH+H=>CH_2OH+H_2$	4.7881E+05	2.55000	5440.000
48.	$CH_3OH+O=>CH_3O+OH$	3.3881E+04	2.50000	3080.000
49.	$CH_3OH+O=>CH_2OH+OH$	5.1127E+05	2.50000	3080.000
50.	$CH_3OH+OH=>CH_2OH+H_2O$	1.6181E+04	2.65000	-806.700
51.	$CH_3OH+HO_2=>CH_3O+H_2O_2$	2.1136E+12	0.00000	20070.700

52.	$CH_3OH+HO_2=>CH_2OH+H_2O_2$	3.6901E+13	0.00000	18782.200
53.	$CH_3OH+CH_3=>CH_3O+CH_4$	1.0453E+04	2.42500	8579.500
54.	$CH_3OH+HCO=>CH_2OH+CH_2O$	8.9697E+03	2.90000	13110.000
55.	$CH_2OH+CH_2O=>CH_3OH+HCO$	1.4302E+02	3.27650	3762.260

Appendix II: Chemkin interface

Below are presented indicative examples using the Chemkin code for each type of simulation.

Ignition delay time simulations

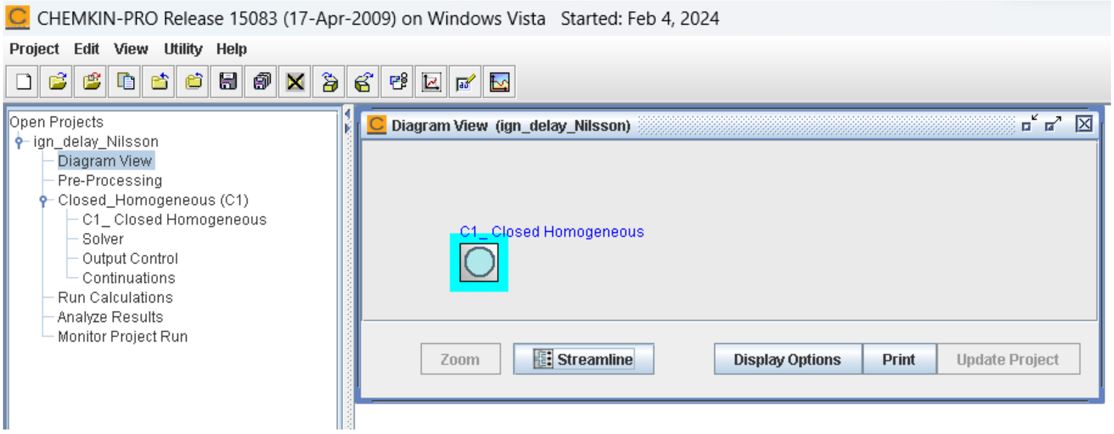

Figure 90. Chemkin-Ignition delay time - Diagram View

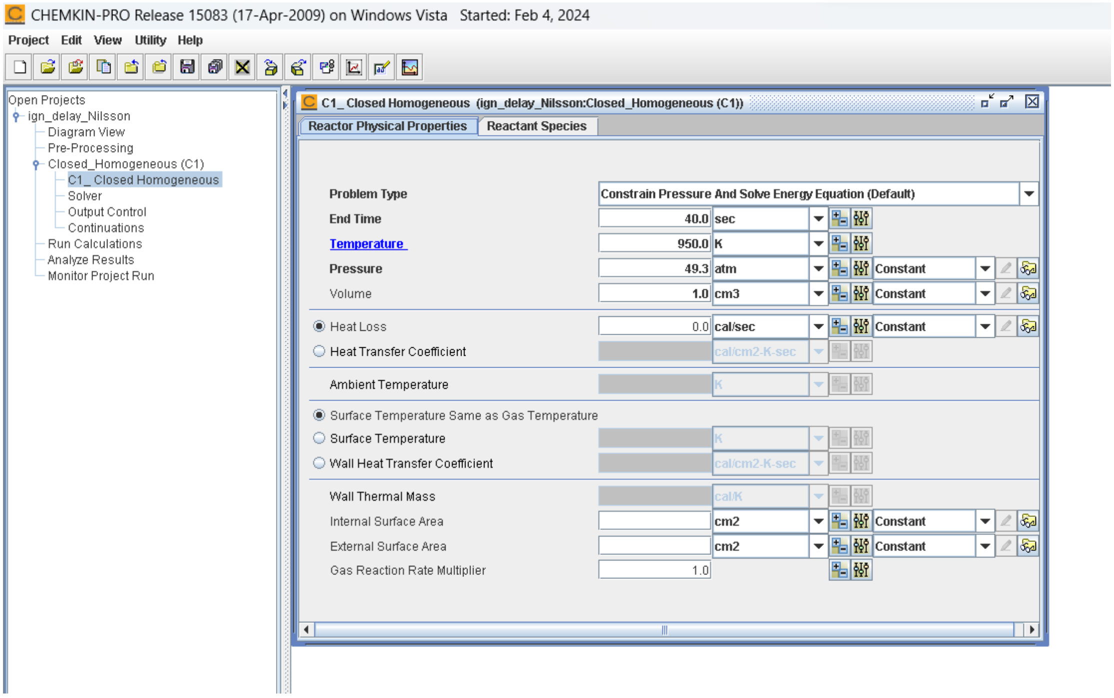

Problem Type	Constrain Pressure And Solve Energy Equation (Default)		
End Time	40.0	sec	
Temperature	950.0	K	
Pressure	49.3	atm	Constant
Volume	1.0	cm3	Constant
● Heat Loss	0.0	cal/sec	Constant
○ Heat Transfer Coefficient		cal/cm2-K-sec	
Ambient Temperature		K	
● Surface Temperature Same as Gas Temperature			
○ Surface Temperature		K	
○ Wall Heat Transfer Coefficient		cal/cm2-K-sec	
Wall Thermal Mass		cal/K	
Internal Surface Area		cm2	Constant
External Surface Area		cm2	Constant
Gas Reaction Rate Multiplier	1.0		

Figure 91. Chemkin-Ignition delay time - Reactor Physical Properties

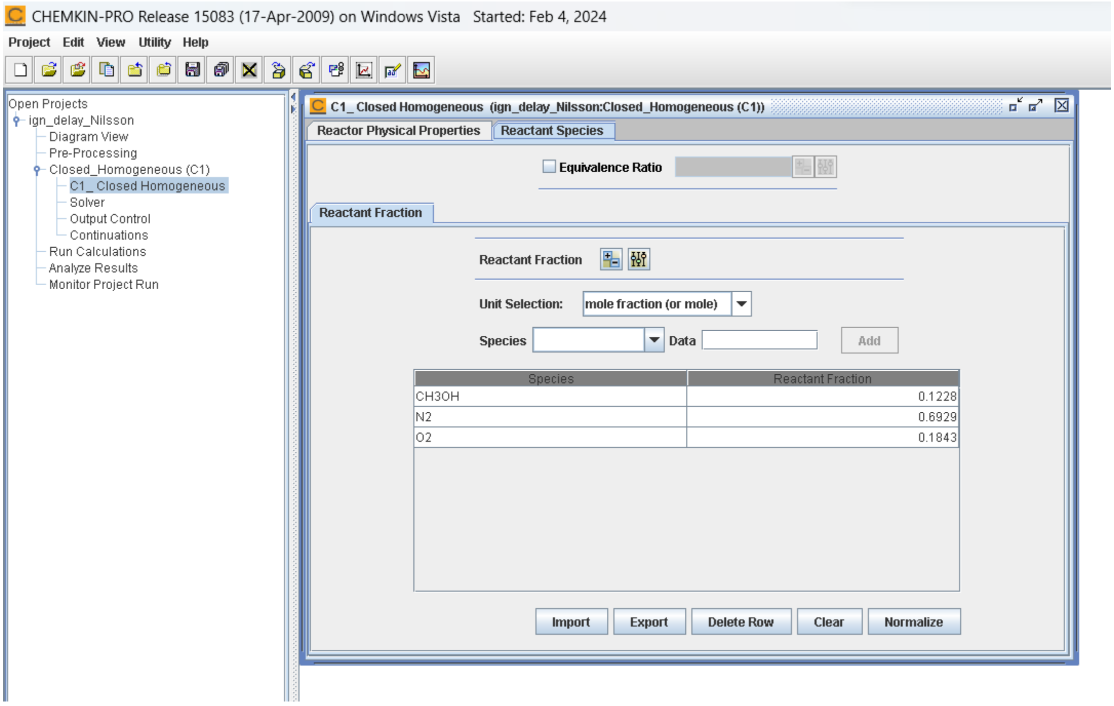
CHEMKIN-PRO Release 15083 (17-Apr-2009) on Windows Vista   Started: Feb 4, 2024

C1_Closed Homogeneous (ign_delay_Nilsson:Closed_Homogeneous (C1))

☐ Equivalence Ratio

Unit Selection: mole fraction (or mole)

Species	Reactant Fraction
CH3OH	0.1228
N2	0.6929
O2	0.1843

Figure 92. Chemkin-Ignition delay time – Reactant Species

Simulations at PSR conditions

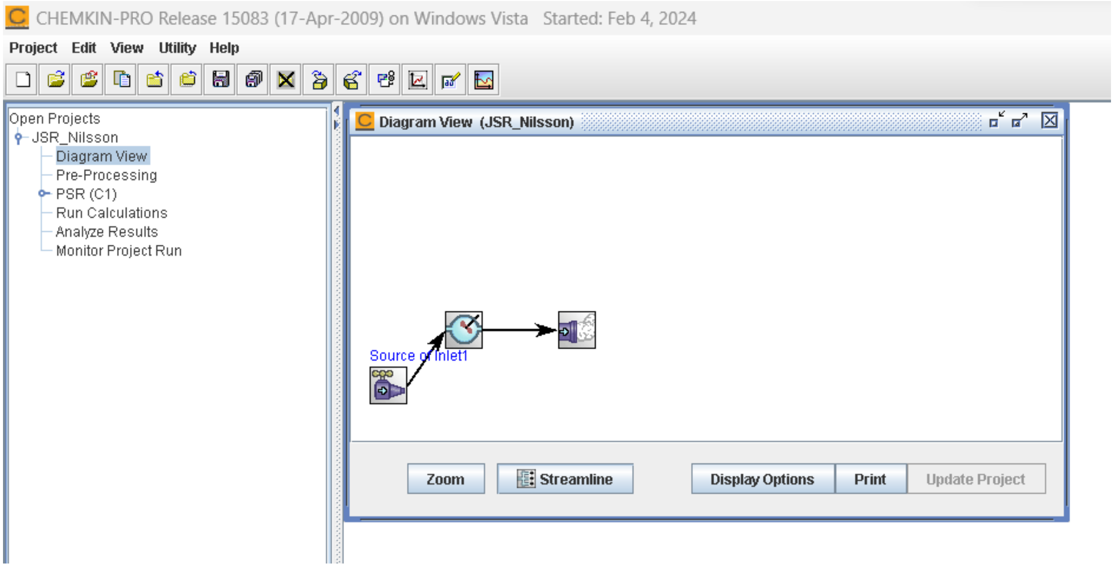
CHEMKIN-PRO Release 15083 (17-Apr-2009) on Windows Vista   Started: Feb 4, 2024

Diagram View (JSR_Nilsson)

Figure 93. Chemkin - Concetration profiles - Diagram View

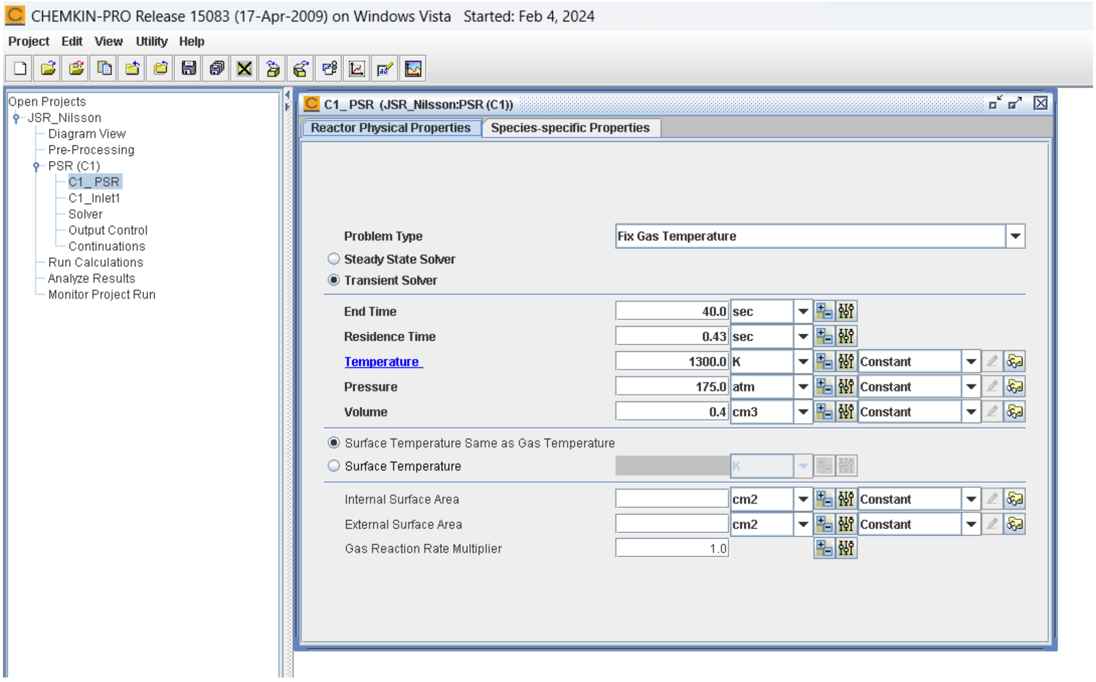

Problem Type: Fix Gas Temperature

○ Steady State Solver

● Transient Solver

End Time	40.0	sec	
Residence Time	0.43	sec	
Temperature	1300.0	K	Constant
Pressure	175.0	atm	Constant
Volume	0.4	cm3	Constant

● Surface Temperature Same as Gas Temperature

○ Surface Temperature K

Internal Surface Area		cm2	Constant
External Surface Area		cm2	Constant
Gas Reaction Rate Multiplier	1.0		

Figure 94. Chemkin - Concertation profiles - Reactor Physical Properties

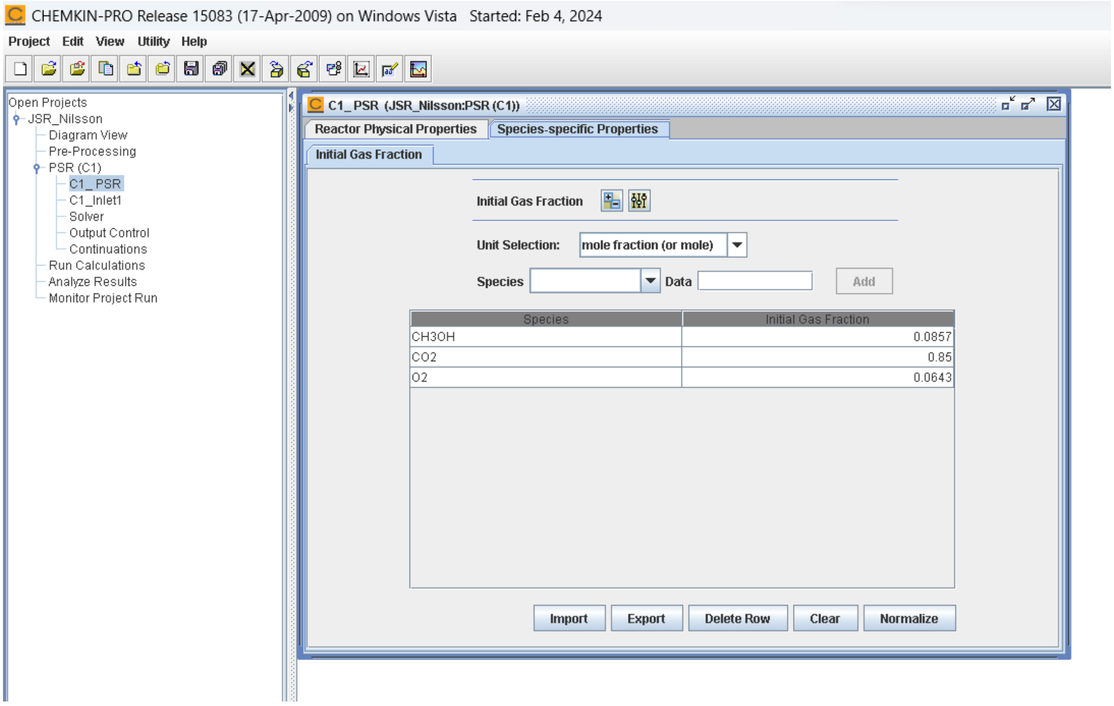

Initial Gas Fraction

Unit Selection: mole fraction (or mole)

Species Data

Species	Initial Gas Fraction
CH3OH	0.0857
CO2	0.85
O2	0.0643

Figure 95. Chemkin - Concertation profiles – Species - specific Properties

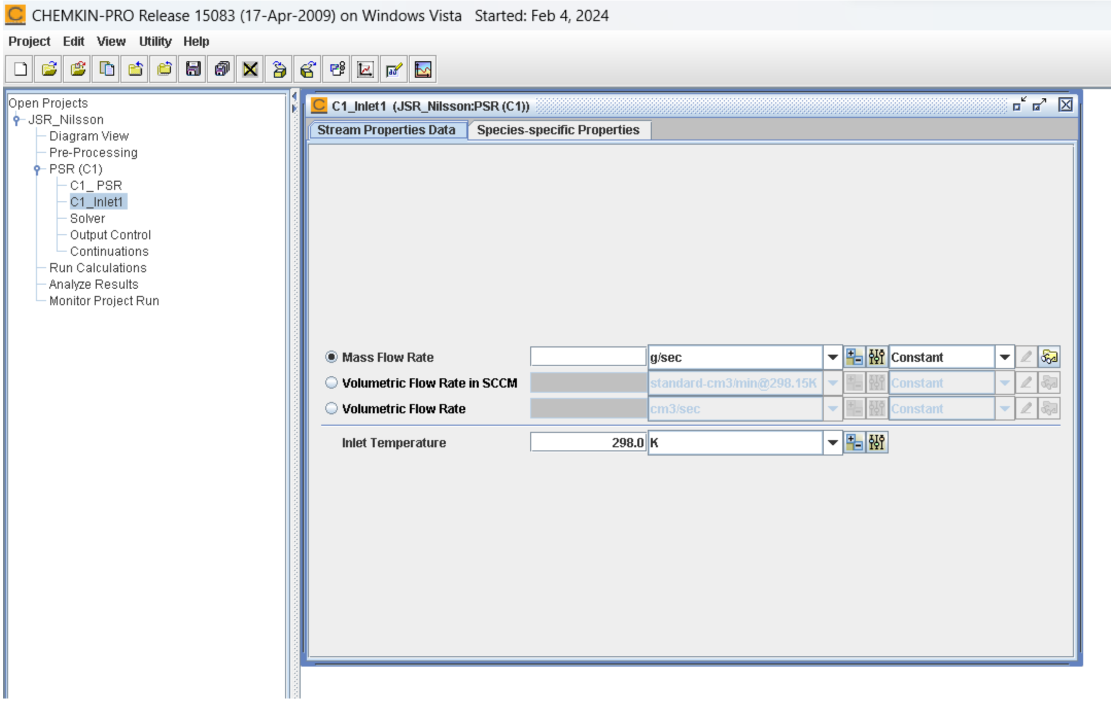

● Mass Flow Rate g/sec Constant

○ Volumetric Flow Rate in SCCM standard-cm3/min@298.15K Constant

○ Volumetric Flow Rate cm3/sec Constant

Inlet Temperature 298.0 K

Figure 96. Chemkin - Concertation profiles –Stream Properties Data

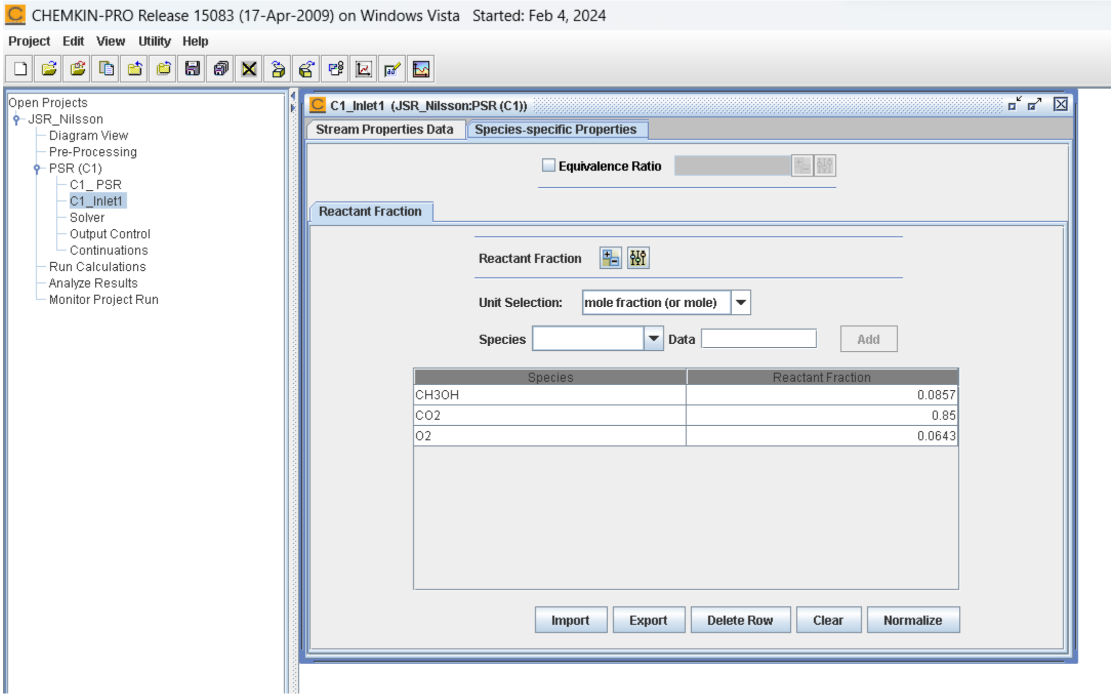

☐ Equivalence Ratio

Reactant Fraction

Unit Selection: mole fraction (or mole)

Species	Reactant Fraction
CH3OH	0.0857
CO2	0.85
O2	0.0643

Figure 97. Chemkin - Concertation profiles – Species - specific Properties

Laminar flame speed

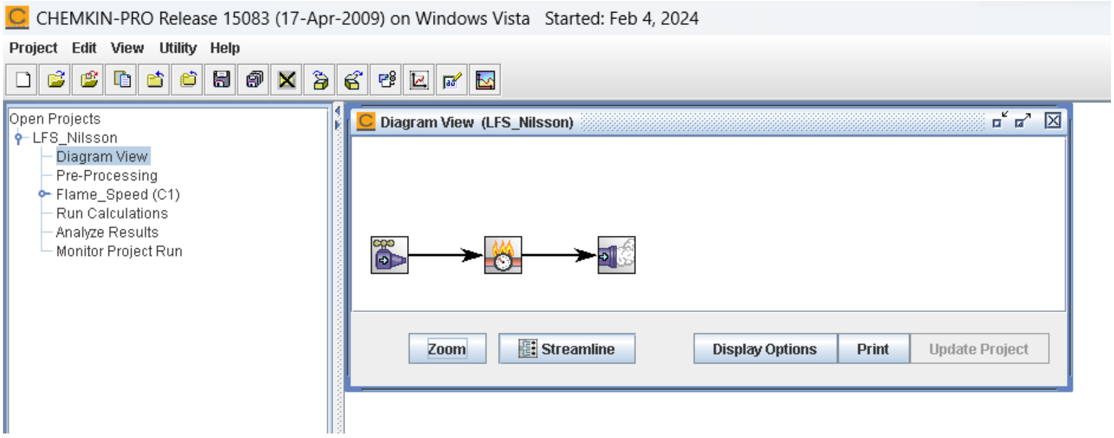

Figure 98. Chemkin - Laminar premix flame speed - Diagram View

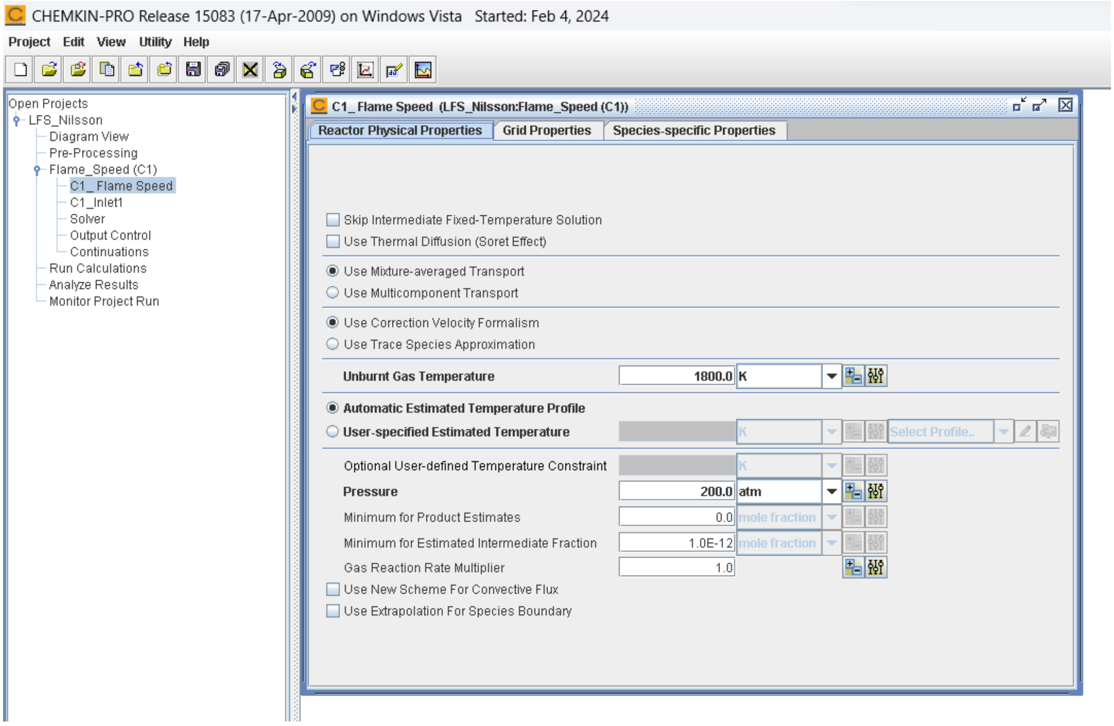

☐ Skip Intermediate Fixed-Temperature Solution
☐ Use Thermal Diffusion (Soret Effect)

● Use Mixture-averaged Transport
○ Use Multicomponent Transport

● Use Correction Velocity Formalism
○ Use Trace Species Approximation

Unburnt Gas Temperature 1800.0 K

● **Automatic Estimated Temperature Profile**
○ **User-specified Estimated Temperature** K Select Profile..

Optional User-defined Temperature Constraint K
Pressure 200.0 atm
Minimum for Product Estimates 0.0 mole fraction
Minimum for Estimated Intermediate Fraction 1.0E-12 mole fraction
Gas Reaction Rate Multiplier 1.0

☐ Use New Scheme For Convective Flux
☐ Use Extrapolation For Species Boundary

Figure 99. Chemkin - Laminar premix flame speed - Reactor Physical Properties

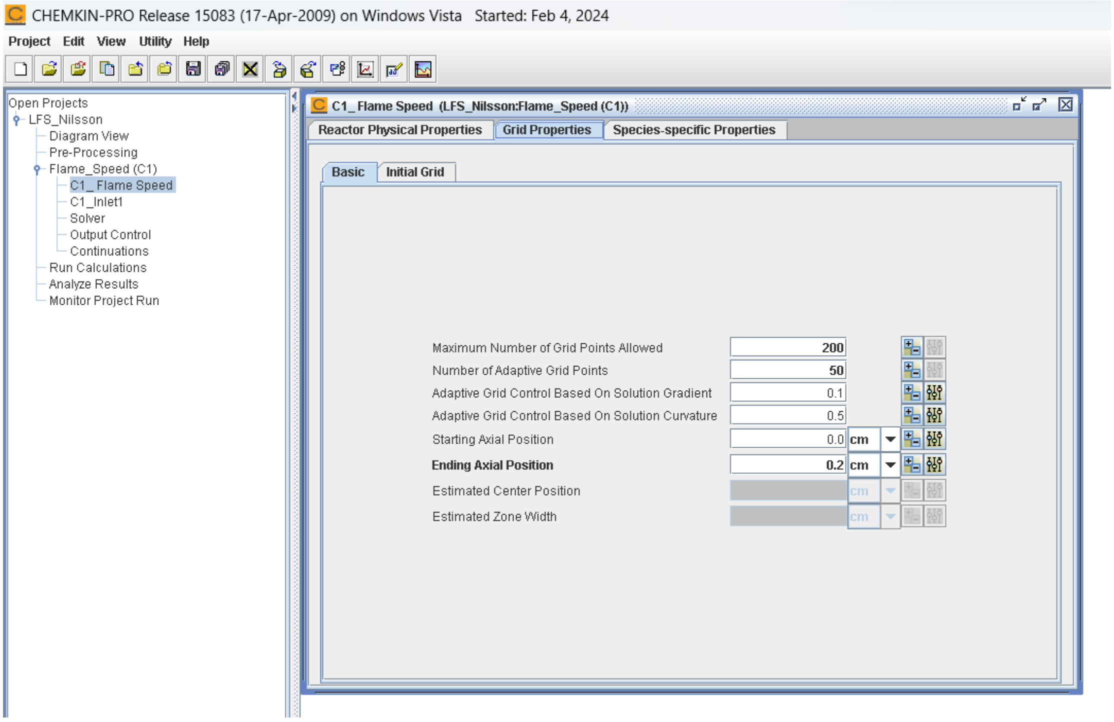

Maximum Number of Grid Points Allowed 200

Number of Adaptive Grid Points 50

Adaptive Grid Control Based On Solution Gradient 0.1

Adaptive Grid Control Based On Solution Curvature 0.5

Starting Axial Position 0.0 cm

Ending Axial Position 0.2 cm

Estimated Center Position cm

Estimated Zone Width cm

Figure 100. Chemkin - Laminar premix flame speed - Grid Properties

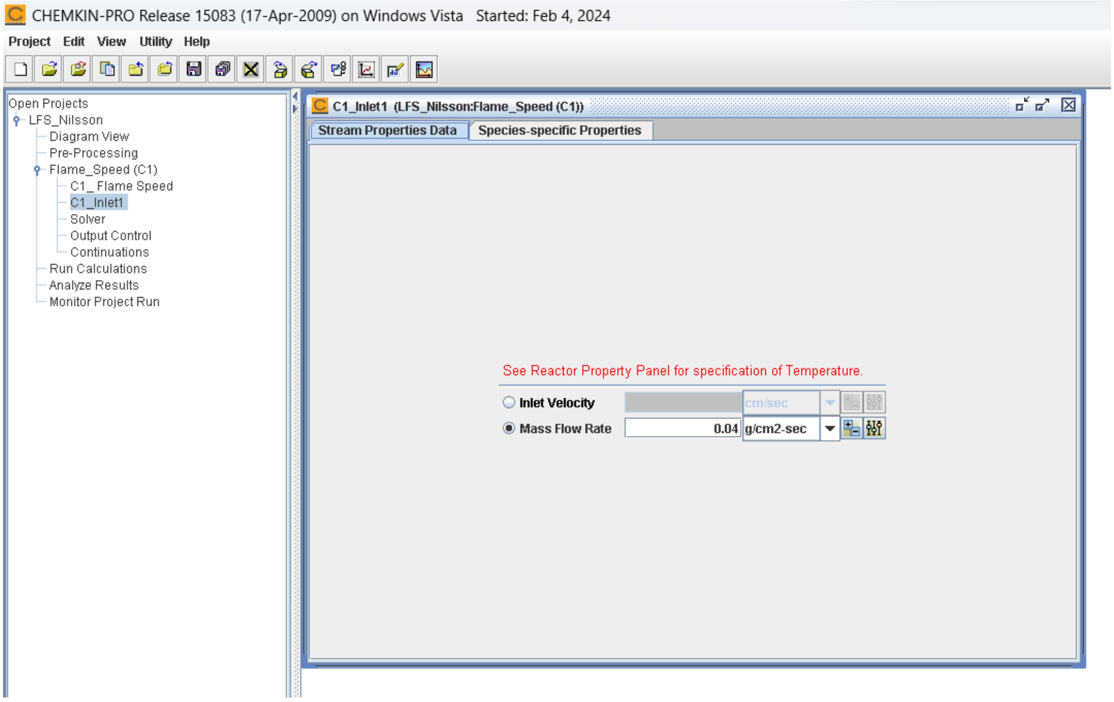

See Reactor Property Panel for specification of Temperature.

○ **Inlet Velocity** cm/sec

● **Mass Flow Rate** 0.04 g/cm2-sec

Figure 101. Chemkin - Laminar premix flame speed - Stream Properties Data

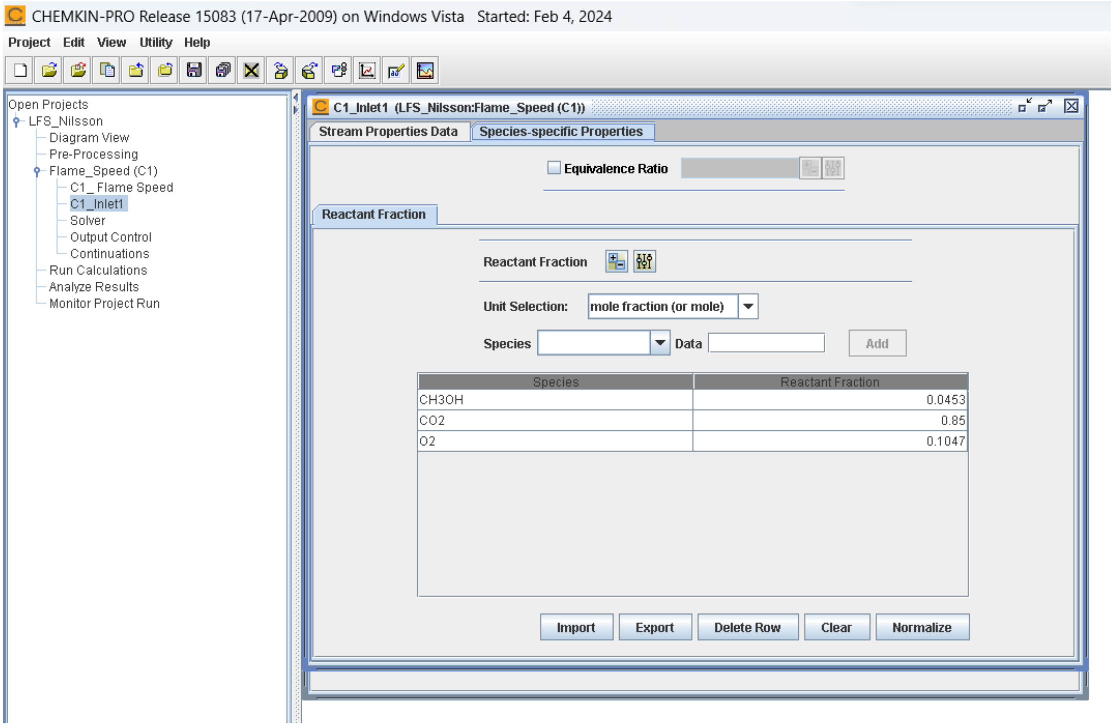

☐ Equivalence Ratio

Unit Selection: mole fraction (or mole)

Species	Reactant Fraction
CH3OH	0.0453
CO2	0.85
O2	0.1047

Figure 102. Chemkin - Laminar premix flame speed - Species - specific Properties